Channel Modelling and Fractionally-Spaced MMSE Equalisers for Broadband Channels

Ghassem Narimani

A thesis presented for the degree of

Doctor of Philosophy

in

Electrical and Electronic Engineering

at

The University of Canterbury

Christchurch, New Zealand

February 2018

Abstract

Channel Modelling and Fractionally-Spaced MMSE Equalisers for Broadband Channels

In response to the increasing demand for high data rate communications, broadband (BB) wireless systems utilising several gigahertz (GHz) of bandwidth will be used in future generations of wireless networks. The characteristics of BB wireless channels differ from those of narrowband (NB) channels. Three of the key differences are as follows:

1. The response of communication system components (e.g., connectors and antennas in each direction) and propagation mechanisms (e.g., diffraction, scattering, reflection from and transmission through obstacles) over a wide frequency band are frequency selective. As a result, per-path pulse distortion in BB channels is more than NB channels. In NB channel modelling the frequency dependency of physical channel effects are usually ignored and the frequency dependency of antennas and connectors are minimised using matching circuits and appropriate antenna design. The residual frequency dependency does not cause considerable approximation error because variations of the electric parameters of materials over a narrow frequency band are not significant.

2. The delay spread of BB channels in terms of symbol interval are much longer than those of NB channels. This is due to the fact that the duration of a BB pulse is shorter than that of a NB pulse.

3. A BB channel consists of many clusters of propagation paths. The clustering effect tends not to be observable in indoor NB channel measurements because the pulse length[1] of electromagnetic pulses used in NB systems are usually large compared to the geometrical size of the scatterers and the differences between the lengths of paths travelled by individual pulses. Therefore, a large number of

[1]For a transient electromagnetic pulse with limited duration of T_p seconds, the pulse length $\lambda_p = c\,T_p$, where c is the speed of light in free space. The pulse length of a pulse is inversely related to its bandwidth.

received pulses overlap at the receiver to make a single fading multipath component. But, when the pulse bandwidth is large, its duration (and consequently, its pulse length) is short and the number of overlapping pulses at the receiver are fewer.

Per-path pulse distortion occurs in channels with large fractional bandwidths. Longer delay spread and the clustering phenomena are more observable in channels with large absolute bandwidths. In channel modelling there are no particular values for absolute or fractional bandwidths in order to be used for classifying channels with respect to the significance of per-pulse distortion effects, channels' delay spreads or their clustering effects. This is so because the significance of these effects not only depend on the channel's fractional and absolute bandwidth but also on the communication environment. Therefore, in this thesis, we use the term BB to refer to those channels that in their mathematical models none of the above mentioned effects is ignored.

The design of an appropriate receiver and its theoretical and simulated performance analysis depends on the adopted model for the channel. In this thesis, certain issues regarding channel modelling and receiver designing for BB systems are considered.

Considering the above mentioned differences of NB and BB channels, we derive a mathematical formula for a lowpass received signal from a BB channel which includes pulse distorting effects of the physical channel due to frequency selectivity and wideband Doppler effect. For a given pulse shaping filter, we characterise the smallest signal space that includes the set of all received signals from a BB channel. In particular, it is shown that an appropriate model for a BB channel is a fractionally-spaced tapped delay-line (TDL) model in which the tap delays are shorter than the symbol interval. Then, using a realizable front-end receiver filter and the properties of orthonormal bases, a set of variables is extracted that constitute a sufficient statistic for any optimum receiver. The geometry of Hilbert spaces and the theory of shift-invariant subspaces of finite-energy signals are used to prove the sufficiency of the extracted statistic. Our approach does not suffer from the ideality of the Shannon sampling theorem and the corresponding sampling models for communication channels. We show that using realisable filters the performance of the ideal lowpass filter can be achieved.

As a case study of the per-path pulse-distorting effects of a physical channel, we analyse the effects of lossy dielectric walls on BB pulses by using the basic principles of electromagnetics and frequency domain methods. The frequency-dependent parameters of commonly used building materials are used to analyse the effects of multiple reflections and transmissions, material distortion, and interpulse interference (IPI) on BB pulse waveforms. The possibility of polarisation-dependent distortion (PDD) is

discussed. Various thicknesses of walls and angles of incidence are considered. The distortion due to each effect is quantified in terms of maximum correlation coefficients (MCCs). The overall effect of the wall is modelled as a TDL filter based on the MCC. Using our model derivation approach, the sources of the multicluster and the soft-onset phenomena of BB channel models are explained. This part of the thesis proposes a theoretical approach, by using laws of classical electromagnetics, to derive models for indoor channels where reflection from and transmission through walls or partitions are major propagation mechanisms. The theoretical approach can be used to complement and validate the experimental channel modelling approaches.

It is well known that in a linear transmission system with unknown channel information, where a basic pulse shape with non-zero excess bandwidth is used for transferring information symbols, a sufficient statistic for any optimum detection method can only be obtained by sampling the received signal at rates higher than or equal to the Nyquist rate for the received signal[2]. In this case the channel observed by a receiver is a fractionally-spaced (FS) TDL channel. Specially, in BB channels where there exists significant pulse distortion due to the frequency dependency of the BB channel effects, the necessity of adopting a FS channel model and employing a FS equaliser becomes more prominent.

Another feature of BB channels is their longer delay spread compared to NB channels when measured in terms of their corresponding symbol intervals. The longer delay spread of BB channels increases the sensitivity of adaptive receivers to perturbations when used for these channels.

The final part of the thesis is devoted to spectral analysis of FS minimum mean-square error (MMSE) equalisers. While many aspects of the FS MMSE equalisers have been studied since their first appearance in the literature in 1970s, some aspects of them are not completely understood. For example, behaviour of a FS MMSE equaliser is usually speculated based on the eigenvalues of the correlation matrix of the input FS samples of the received signal. A characterisation of the equaliser in terms of its transfer function (TF) that includes the effects of the front end prefilter and sampler is not available in the literature. In Chapter 4, we derive the TF of a FS MMSE equaliser under the general system model described in Chapter 2. Then, the TF is used to analyse the behaviour of the adaptive FS MMSE equaliser.

An adaptive FS MMSE equaliser, implemented using the least-mean-square (LMS) algorithm, suffers from instability. Stabilisation of adaptive FS MMSE equalisers has a long history. A major problem in dealing with FS sampling receivers is the non-stationarity of the received sampled process, even if the channel itself is time invariant. In communication systems that use a linear modulation scheme for transmission, the FS

[2]The Nyquist sampling rate for a signal with maximum absolute frequency $f_{\max}$ is equal to $2f_{\max}$.

samples of the received signal from a wide-sense stationary (WSS) channel constitute a wide-sense cyclostationary (WSCS) time series. Hence, standard Fourier transform techniques cannot be used directly to study the spectral characteristics of the received FS samples or to derive the TF of the corresponding MMSE receiver. In this thesis, an expression for the TF of the FS MMSE equaliser is derived. Due to the WSCS nature of the input sampled signal, the FS equaliser's TF is periodically time varying. Using the TF, the sources of instability of the FS LMS algorithm are characterized. The obtained results improve the existing knowledge in the literature regarding the sources of instability of FS MMSE equalisers. Based on the analysis performed, sufficient conditions are provided to increase the stability and guarantee convergence of the FS LMS algorithm.

For channels with longer delay spread, such as BB channels, the corresponding TDL equaliser needs to be sufficiently long in order to perform satisfactorily. The LMS algorithm is more sensitive to perturbation when the equaliser delay line is longer. The effects of equaliser length and sampling phase on stability of the LMS algorithm are explained. The waveform level simulations of communication systems validates the theoretical results.

Acknowledgements

I would like to take this opportunity to express my gratitude to many people who have helped and supported me during the course of my study in the University of Canterbury.

First of all, I appreciate my supervisors Prof. Philippa Martin and Prof. Des Taylor for their excellent guidance. They read tirelessly several versions of my writings for publication of papers and preparation of this thesis. The feedbacks I received from them improved my way of thinking and explaining my ideas.

Secondly, I would like to thank the academic and technical staff in the Department of Electrical Engineering and Computer Science for providing suitable environment for doing research and living in. I would like to extend my dearest gratitude to my fellow students in the department and in the university that we enjoyed together many events, activities, and discussions. My special thanks to Ken Smart for organising football games and managing the department team.

Last but foremost, my special gratitude with a flavour of love goes to my wife, who does not expect appreciation but always have mine in any moment of my life. Her unconditional love and infinite support gave me the power to reach my goals.

Dedication

To Parinaz and Babak

Contents

List of Figures

List of Tables

Abbreviations, Acronyms and Symbols

Abbreviations and Acronyms

AWGN	Additive White Gaussian Noise
BB	Broadband
C/D	continuous-time-to-discrete-time
CLT	Central Limit Theorem
CT	Continuous-Time
DSP	Digital Signal Processing
DT	Discrete-Time
ESD	Energy Spectral Density
EVM	Error Vector Magnitude
FCC	Federal Communications Commission
FS	Fractionally-Spaced
FS	fractionally-spaced
GHz	Gigahertz
GSM	Global System for Mobile Communications, originally Groupe Spècial Mobile
IPI	Interpulse Interference
IR	Impulse Response

LMS	Least Mean-Square
MAP	Maximum a Posteriori Probability
MCC	Maximum Correlation Coefficient
ML	Maximum Likelihood
MLSD	Maximum-Likelihood Sequence Detection
MMSE	Minimum Mean-Square Error
NB	Narrowband
NLOS	Non-Line-of-Sight
OFDM	Orthogonal Frequency-Division Multiplexing
ONB	Orthonormal Basis
PDD	Polarisation-Dependent Distortion
PDP	Power-Delay Profile
PHY	Physical Layer
PSD	Power Spectral Density
RF	Radio Frequency
SIS	Shift-Invariant Subspace
SNR	Signal-to-Noise Ratio
SRRC	Square-Root Raised Cosine
SS	Symbol-Spaced
TDL	Tapped Delay-Line
TF	Transfer Function
TF	Transfer Function
UWB	Ultrawideband

WSCS	Wide-Sense Cyclostationary
WSS	Wide-Sense Stationary
WSSUS	Wide-Sense Stationary Uncorrelated Scattering

Symbols

ϵ	permittivity
ϵ_c	complex permittivity
ϵ_r	relative permittivity or dielectric constant
$\mathcal{L}_2$	The space of (Lebesgue-measurable) finite energy signals
$\mathcal{L}_\infty$	The space of (Lebesgue-measurable) essentially bounded signals
μ_r	relative permeability or magnetic constant
μ	permeability
$\overline{z}$	The complex conjugate of a complex number z
Re$[z]$	The real part of a complex number z
σ	conductivity

Chapter 1

Background

Synopsis This chapter includes the motivations, description of the problems, a review of the research results of the thesis and the approaches used to obtain these results.

1.1 Motivation and Outline

In a wireless communication system, when the transmitted signal's absolute or fractional bandwidth is sufficiently large, some channel response characteristics change significantly compared to the case where the signal's absolute and fractional bandwidth are small [85, 26]. This implies the necessity for a revision of the widely used wide-sense stationary uncorrelated scattering (WSSUS) model [9, 102, 87] to include the frequency-dependent effects of the channel. In fact, the WSSUS model is based on the *narrowband (NB) assumption* and cannot be used as an appropriate model for channels with large absolute/fractional bandwidths. Experimental measurements of ultrawideband (UWB) channel responses have shown that some characteristics of UWB channels are significantly different from NB channels [84, 83, 85, 26]. The following quote from the introducer of the WSSUS model, Philip A. Bello [9], emphasises this point [10]:

> "The WSSUS channel model has provided a useful tool for modelling random time variant linear channels in the four decades since its introduction. However, with the advent of UWB (Ultra Wideband) communications, it is necessary to replace this model which is valid for Narrowband (NB) channels."

The research of this thesis is motivated by the necessity of revising the traditional NB channel modelling approach and optimum receiver designs. The main thrust of Chapter 2 is to provide a sufficiently general mathematical model for wireless channels that includes the frequency dependency of the channel effects. However, our considerations are limited to mathematical analysis using physical principles rather than model derivation using experimental methods.

The analysis in Chapter 2 shows that an appropriate discrete-time (DT) channel model should be fractionally-spaced (FS) in order to be able to capture all characteristics of a real continuous-time (CT) channel. Accordingly, an optimum receiver is also FS. Therefore, in chapter 4, we study the FS minimum mean-square error (MMSE) receiver and some issues in its practical implementations.

Implementation of FS receivers requires particular care as sampling the received baseband signal at a rate higher than the symbol rate can cause singularity at the equaliser. We consider the singularity problem for FS MMSE equaliser. While the study was inspired by the current trend in utilising wide frequency bands for wireless communications, the results are valid for all wireless communication systems irrespective of their absolute or fractional bandwidths.

In this thesis (Chapter 2) the channel and antenna effects are modelled mathematically by linear operators including linear filters with arbitrary impulse responses in each spatial direction and Doppler dilation operators. Then, it is shown that the appropriate channel model with *a priori* unpredictable channel response should be FS rather than a symbol spaced one. The necessity of a FS channel model comes from the fact that, in practice, all pulse shapes used for transmitting information symbols have non-zero excess bandwidth. Therefore, sampling the received signal at transmission symbol rate causes aliasing [94].

When the channel impulse response over a certain frequency band is not known (for example, due to aliasing), or equivalently, its pulse response for a given input pulse is not known, it is impossible to perform synchronisation, channel estimation, equalisation and detection satisfactorily using a symbol-spaced (SS) sampling receiver[1].

[1] In information theoretic studies of communication systems, it is usually assumed that the channel impulse response is known at least statistically [102, 12]. When the receiver samples the received signal at symbol rate, this assumption is not justifiable. [77]

Considering this fact, in the lack of channel state information there is no reason to assume a SS channel model and analyse or simulate the system performance based on this assumption.

Adopting a FS channel model, it is well known that the uncorrelated scattering assumption breaks down. The FS samples of the received signal can be correlated, as two or several samples may correspond to a response signal received from a single scatterer. When the fractional bandwidth of the transmitted pulse is large, the wide-sense stationary assumption can also be questioned. In large fractional bandwidth signals, the pulse length[2] is comparable to the carrier wavelength. As a result, movements at the scale of the carrier signal's wavelength of the communicating devices can change the location of the multipath components on the delay line; a phenomenon that is not considered in WSSUS channel models.

Main results of this thesis are presented in Chapters 2, 3 and 4 and are reviewed in Sections 1.3, 1.4 and 1.5. Now, a brief review of the thesis is given to connect the separated results presented in chapters 2-4.

Chapter 2 proposes using a FS baseband channel model for channels with large absolute or fractional bandwidths. To do this, the equivalent complex baseband model of the CT received signal from such a channel is derived. The complex baseband model incorporates the Doppler time dilation effects on individual received pulses modelled as dilation operators, Doppler frequency shift of the carrier wave, the filtering effects due to antennas and the interacting objects in the propagation channel which are modelled as filtering operations. The individual pulse distortion due to Doppler time dilation as well as the filtering by the antennas and interacting objects are usually ignored in traditional NB models. In order to capture the information available in the lowpass received signal according to the proposed FS channel model, the front-end receiver continuous-time-to-discrete-time (C/D) converter is defined. The C/D converter consists of a lowpass filter, referred to as a prefilter, and a sampler. The characteristics of the prefilter is determined in such a way that it is realisable and the samples provide a sufficient statistic for any kind of optimum receiver.

In order to substantiate the motivations for using FS channel models, Chapter 3

[2]In this thesis, for a transient pulse of duration T_p, we define its pulse length as $\lambda_p \triangleq T_p\, c$, where c is the speed of light.

provides a detailed analysis of the pulse distortion phenomena due to lossy dielectric walls. Experimental studies of effects of lossy dielectric walls on UWB pulses have shown that the pulses reflected off or transmitted through these walls experience significant distortions [19, 26]. However, a detailed analysis of these distortions and their sources based on the principles of electromagnetic wave propagation was missing in the literature. Chapter 3 can be considered as a case study of the pulse distortion phenomena observed in experimental studies using signals with large absolute or fractional bandwidths. This study provides useful insights for understanding the sources of the clustering effect and a sort of soft onset phenomenon [85] observed in UWB channel measurements.

Chapter 4 focuses on the receiver side. Design of an optimum receiver depends on the adopted model for the channel. Adopting a FS channel model as described in Chapter 2, we study the optimum FS equaliser based on the MMSE criteria. The study of FS MMSE equalisers have a long history. Since 1970s many aspects and capabilities of FS MMSE equalisers have been studied by many researchers [17, 147, 42, 40, 102]. However, there are several open question regarding these equalisers. The main open problem is the characterisation of the FS MMSE equaliser's transfer function (TF) that explicitly includes the effects of the C/D converter, transmit and receive filters, channel IR and the sampling phase errors. The other problem is the sources of instability of the FS MMSE equaliser when it is implemented using the popular least mean-square (LMS) algorithm. In Chapter 4 these problems are addressed by derivation of the TFs of FS MMSE equalisers and proposing a stabilisation method for the FS LMS algorithm. Then we describe the effects of the TDL equaliser's length, sampling phase offsets and indeterminacy of the equaliser TF over some frequencies on the stability of the LMS algorithm using the derived TF of the FS MMSE equaliser. This approach is different from others in the literature where these problems are discussed based on the eigenstructure of the correlation matrix of the input samples (regressors) [117].

1.2 Nomenclature

"The beginning of wisdom is the definition of terms." – Socrates

We will frequently use the terms NB, UWB and broadband (BB) throughout the thesis. We start with a description of these terms as they may have other meanings in other contexts. There are no unified definitions for the terms BB and NB in the field of wireless communications, but UWB has a standard definition [31]. Currently, the term UWB is generally used to referred to a wireless communication technology that uses UWB signals for transmission. A signal $s(t)$ is called UWB [31] if it satisfies at least one of the following conditions:

1. The effective absolute bandwidth of $s(t)$ is larger than 500 MHz.
2. The effective fractional bandwidth of $s(t)$, i.e., the bandwidth divided by the carrier (or centre) frequency, is larger than 0.20.

For a transmission system, the bandwidth is defined by using the power spectral density (PSD) of the signal emitted by an antenna. There are physical reasons for this classification of channels that will become clear in the following sections.

The term BB has been used in many contexts including commercial communication services like fibre BB or wireless BB. Our usage of NB and BB is in the context of channel modelling approaches. We use *BB channel model* to refer to a wireless transmission system model that considers the frequency-selectivity of the transmit and receive antenna effects, the propagation channel effects such as reflection, diffraction, refraction, and transmission through lossy media, and the Doppler effect. In traditional channel models, usually the frequency selectivity of these effects is ignored, that is they are based on the *NB assumptions* [62, 151]. When this is the case, we refer to the model as a *NB channel model*.

We use the terms NB and BB to refer to two different *channel modelling approaches* as described in the above paragraph. We will also use the same terms to refer to communication channels or systems depending on whether the NB assumptions are valid or invalid for them. For example, NB assumptions are not valid for a UWB system with large fractional and/or absolute bandwidth [85]. Therefore, UWB channels are included within the category of BB channels. Underwater acoustic (UWA) channels are other examples of BB channels, as the NB assumptions are not valid for them [129].

The reason for this classification of BB channels is that, as described before,

the traditional wide-sense stationary uncorrelated scattering (WSSUS) channel model might not be valid for them [10]. WSSUS channel model have been used successfully for many decades, but for BB channels a revision of WSSUS model is required [10, 85]. WSSUS channel models are essentially based on NB assumption by construction [9, 102][3]. We use the phrase NB channel and NB model to refer to all channels and their mathematical models when the NB assumption is valid or assumed to be valid for them.

Multipath channel models are widely used for wireless channels. An important characteristic of a multipath channel model based on the NB assumption is that its multipath subchannels (i.e., multipath components of the channel) are assumed to be frequency flat. This implies that in these channel models pulse waveforms received from different paths are assumed to be exactly the same as the transmitted pulse waveform[4]. For a channel with a large absolute or fractional bandwidth, the NB channel assumption might not be valid [85]. As such, in these channels, per-path pulse distortion must be taken into account. Per-path pulse distortion phenomenon can be due to extremely large bandwidth and/or relatively large fractional bandwidth compared to the traditional systems. Therefore, the channel models for UWB systems are classified as BB channels.

1.3 Wireless Channel Modelling for BB Systems

The validity of simulation-based performance analysis of wireless BB systems depends crucially on having accurate and useful models of the BB channel. In principle, any model for a physical communication channel serves two major purposes. It provides:

1. a model for the received signal and hence a receiver can be designed based on certain optimality criteria; and

2. a tool for testing various communication strategies by adopting appropriate modulation and demodulation techniques.

[3]Details are provided in **??**.

[4]Pulse waveform changes when it is distorted. Distortion includes phase distortion and magnitude distortion. Frequency-flat attenuation (by a real or complex constant) or delay do not cause distortion or pulse waveform change.

A wireless channel is usually characterized as a time-variant linear filter having an equivalent lowpass impulse response (IR) $h(t, \tau)$ and an additive zero-mean Gaussian noise process, $z(t)$ [102]. For a transmitted signal $s(t)$, the received signal can be represented by

$$\begin{aligned} r(t) =& \int_{\mathbb{R}} h(t, \tau) s(t - \tau) \, \mathrm{d}\tau + z(t) \\ =& u(t) + z(t), \end{aligned} \tag{1.1}$$

where $z(t)$ is the additive noise. The IR may include effects due to the transmission and reception equipments, antennas, propagation channel, mobility and filtering at the transmitter and receiver. Also, if the transmitter and receiver are not properly frequency synchronized, the residual frequency after down-conversion appears as a rotating phasor in the lowpass IR [77].

The responses of antennas and the propagation channel effects are frequency dependent. The frequency-dependent propagation channel effects include reflection from and transmission through planar objects, scattering by rough surfaces, diffraction by edges and the Doppler [110, 152, 99, 87]. The significance of the impact of these effects in a practical application depends on the bandwidth of the signal, the channel dynamics, and the geometrical and electrical characteristics of the antennas and the interacting objects in the environment. When the system bandwidth is small, the overall effect of antennas and the propagation channel on a pulse received from a single path of a multipath channel can be modelled as a multiplicative constant called path coefficient. Then, the resulting multipath channel model is referred to as a NB channel model as the NB assumption is assumed to be valid.

The bandwidths used by most traditional communication systems are sufficiently narrow that any frequency dependency of most of the physical effects can be safely ignored [10]. In modelling NB channels, three effects are usually considered [102]:

1. delay dispersion due to multipath effect,

2. small-scale fading due to multipath effect, and

3. large-scale fading (or, shadowing) effect due to blocking.

None of these effects include the per-pulse distortion phenomenon.

Mathematical modelling for BB wireless channels, where the transmit pulse bandwidth can be several GHz, is a relatively new field. The existing information about the propagation mechanism of BB signals in various environments are mainly obtained by experiments [26, 86, 109]. Some of these experimental results have been used in [88] to formulate models for UWB channels in order to provide a platform for evaluation of communication systems designed based on the IEEE 802.15.4a standards[5]. The mathematical models for these channels are more complicated than traditional channels as the number of parameters used to describe them statistically is large.

Most modern digital receivers down-convert the continuous-time (CT) received radio-frequency (RF) signal to a lowpass signal $r(t)$ before discretisation. Then, the first task of an all-digital receiver is the extraction of a denumerable set of variables from the received CT signal $r(t)$ that include all information about the channel $h(t,\tau)$ and the transmitted signal $s(t)$ available in the signal $u(t)$. Since the channel and the data are in general random, the extracted variables are random. This set of random variables, denoted by $\mathbf{T}[r(t)]$, is referred to as a sufficient statistic. For establishing reliable coherent communication, knowing the channel, the carrier phase and symbol timing are crucial [102, 77]. Therefore, an optimum digital receiver should be able to acquire these information from the discrete-time (DT) signal $\mathbf{T}[r(t)]$.

In Chapter 2, we consider mathematical channel modelling for BB systems where we follow two goals. There, the first goal is to provide a mathematical formula for the *lowpass* received signal that takes into account the frequency dependency of channel components. Derivation of a mathematical form of the received lowpass signal is a fundamental step in studying any communication system at the physical layer (PHY) [102].

The second goal of Chapter 2 is to design front-end receiver C/D converters that provide a sufficient statistic for an optimum digital receiver. A C/D converter consists of a lowpass filter, referred to as a prefilter, and a fixed-rate sampler. It is well-known that for a linear channel with AWGN, and any linear modulation scheme, a sufficient statistic is obtained by the symbol time-spaced samples of the output of the matched

[5]IEEE 802.15.4a is superseded by IEEE 802.15.4-2011.

filter [34, 102]. For a real pulse shape $p(t)$ a linearly modulated lowpass transmit signal is represented by

$$s(t) = \sum_{n=0}^{N} \mathrm{d}_n p(t - nT), \tag{1.2}$$

where $\{\mathrm{d}_n : n = 1, \cdots, N\}$ is a set of information carrying symbols. The IR of the matched filter is defined by $f_{MF}(t) = \int_{\mathbb{R}} \overline{h(-t, \tau)} p(-t - \tau)\, \mathrm{d}\tau$, where overbar denotes the complex conjugation. Then a sufficient statistic is

$$\mathbf{T}[r(t)] = \{r * f_{MF}(kT - \tau_0) : k = 0, \cdots, N\}, \tag{1.3}$$

where τ_0 is the channel delay and $*$ denotes convolution. The informations required for performing matched filtering are: 1) channel delay, τ_0; 2) symbol interval, T; 3) channel IR; 4) carrier frequency, f_c; and 5) carrier phase. Usually, these parameters are not available at the receiver front end initially and must be acquired from the DT signal using digital signal processing (DSP) methods. Under this condition, the statistic characterised by (1.3) is not observable at the receiver. The matched filter maximizes the signal-to-noise ratio of the samples when the symbols are transmitted individually (without intersymbol interference) and τ_0 is known. This, together with the property of providing a sufficient statistic are the theoretical advantages of matched filtering. In the lack of the matched filter, the characteristics of a front-end C/D converter need to be determined in such a way that the DT signal at its output provides a sufficient statistic for any optimum detection method including matched filtering [102].

The performance study of any digital communication system operating over a given CT channel requires a discrete model for the channel that approximates the discretisation procedure that occurs in practical digital receivers. The goal is to derive a DT model for the channel with the following properties:

1. It captures all characteristics of the CT channel, in the sense that the CT channel can be characterized by the DT model.

2. It is realizable, in the sense that the DT model's variables are practically observable at the receiver.

In information-theoretic studies of communication systems, using the matched

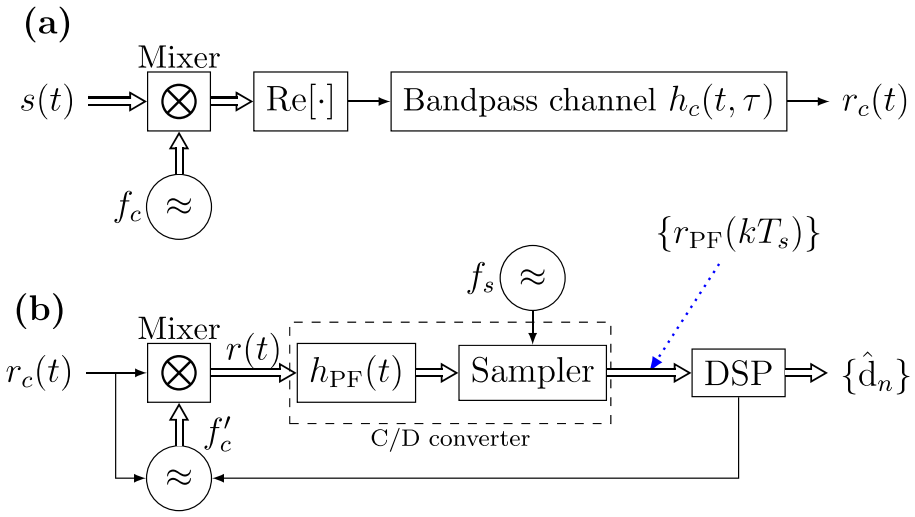

Figure 1.1: Digital communication system. Real-valued signal flows are shown by single-line arrows and the complex-valued signal flows are shown with double-line arrows. (a) Creation of the real bandpass received signal $r_c(t)$. (b) Processing blocks in the front-end of a typical digital receiver [77, 15, 143].

filter is the most common discretisation approach [102, 12, 8]. In this approach, the SS samples of the matched filter output provide a sufficient statistic for any optimum detection method [34]. In the absence of the matched filter or perfect channel state information, the SS samples do not provide a sufficient statistic. Therefore, the channel capacity and performances calculated using SS sampling models and matched filtering cannot be approached in practice. A more realistic performance measures can be obtained using a FS channel model. A receiver corresponding to such a channel model is also FS, meaning that, it processes the samples at a fractional rate [147, 105].

In practical receivers, instead of the matched filter, other filters are used for pre-filtering and the sampling rate of the filter output is usually higher than the symbol rate [15, 40, 102, 132]. Accordingly, the main building blocks of a typical all-digital receiver is as shown in Fig. 1.1 (b).

Detailed block diagrams can be found in [15] and [77].

In Fig. 1.1 (b), the input is a real bandpass signal $r_{\mathrm{c}}(t)$. A coarse estimate f_c' of the carrier frequency f_c, is used to down-convert the received signal to a complex lowpass signal $r(t)$. Due to the frequency offset $f_c' - f_c$ and the phase offset θ_0, a rotating phasor $\exp\left(\mathrm{j}\,2\pi([f_c' - f_c]t + \theta_0)\right)$ appears in the down-converted signal. The lowpass signal

$r(t)$ is passed through a lowpass filter, referred to as prefilter, with impulse response $h_{\mathrm{PF}}(t)$. The output of the prefilter is sampled with a rate f_s. The sampling rate f_s is provided by a free-running oscillator [77]. In general, the transmission symbol rate $\frac{1}{T}$ is incommensurate with the sampling rate f_s [77]. The DT signal from the output of the sampler is forwarded to the digital signal processing (DSP) units where the quantized values are processed to produce the final decision variables $\{\hat{\mathrm{d}}_n\}$, at the transmission symbol rate $\frac{1}{T}$ [77].

Over time intervals longer than the coherence time of the channel, the phase, $\theta_0(t)$, and the IR, $h(t,\tau)$, are functions of time t [102]. For a short duration, which usually spans several symbol intervals [102], they can be assumed to be constant with respect to t. That is, $h(t,\tau) = h(\tau)$ and $\theta_0(t) = \theta_0$. In the design of the prefilter and the sampler, the long term behaviour of the these functions must be taken into account.

Since the received lowpass signal's bandwidth is always larger than the transmitted symbol rate, the appropriate DT model for such a channel is a FS tapped delay-line (TDL) filter model. In Chapter 2, a FS TDL filter model is derived and based on that the optimum receiver structure is characterised. In Chapter 4, the FS MMSE equaliser is considered which is the most popular linear equaliser [102]. There, the transfer function of the FS MMSE equaliser is derived that includes the effects of the front-end receiver C/D converter.

1.4 A Case Study of BB Pulse Distortion in Indoor Channels

In most of the current commercial wireless communication systems the fractional and absolute bandwidth of the channel are small compared to the UWB and BB mm-wave channels. In UWB systems, the information carrying electromagnetic pulses have absolute bandwidth of more than 500 MHz and/or fractional bandwidth of more than 0.2 [31]. In BB mm-wave communication systems based on the IEEE 802.11ad standard [1], the transmitted pulse bandwidth can exceed 2 GHz. As a result of these differences in absolute and/or fractional bandwidths, the channel responses to BB mm-wave and UWB pulses are different from those for NB channels [23, 85]. The differences in channel response to information carrying pulses can stem from these factors:

1. The pulse length of the BB electromagnetic pulses in the air are much smaller than the NB pulses. Therefore, more individual BB pulses are resolvable at the receiver. This happens when the absolute bandwidth of the pulse is large.

2. Electrical properties of the material of the interacting objects are frequency dependent. Therefore, individual received BB pulses can experience more distortion than NB pulses due to interactions with objects. This happens when the fractional bandwidth of the pulse is large.

3. The frequency dependence of the transmit and receive antenna characteristics. All antenna responses are frequency dependent. When the transmitted pulse is NB, by designing appropriate antennas the distortion can be minimised so that it can be ignored [137]. When the fractional bandwidth of the pulse is large, antenna distortion increases to a level than cannot be ignored [159, 119].

In Chapter 3, we focus on the interactions of UWB pulses with walls. We will show that some phenomena observed in UWB propagation such as the clustered distribution of arrival times of pulses [88] and the power-delay profile (PDP) of each cluster [88, 83, 49] are related to the effects of walls [90].

Walls are abundant in indoor and urban communication environments. Electromagnetic waves can reflect off or transmit through a wall with sufficiently large dimensions. When the dimensions of the wall is comparable or smaller that the wavelength of an incident harmonic wave, diffraction occurs which is a different phenomenon and is not considered in this thesis. This is due to the complexity of mathematical analysis of the diffraction effects involved with the propagation of transient pulses [104, 103] and the fact that reflection from and transmission through walls are the dominant propagation mechanisms in indoor environments [112].

Three of the key differences between the interactions of NB and BB pulses with lossy dielectric walls are:

1. The time-harmonic approximations of time-limited pulses, as used in modelling NB systems and receiver design [102], do not adequately characterize BB channels [26, 86, 23]. Each pulse experiences amplitude and phase distortion.

2. Lossy dielectric walls illuminated by a BB pulse, reflect/transmit several separate or partially-overlapped BB pulses.

3. Due to polarization-dependent surface reflection and transmission [5], the transmission and reflection responses of lossy dielectric walls for parallel and perpendicular polarizations are different and may cause polarization-dependent distortion (PDD).

Waveform distortion is a degrading factor in BB systems [137, 104, 103, 85]. The theoretical study of pulse distortion due to some special diffracting geometrical objects was considered in [104] and [103]. Time domain methods for wall reflections and transmission were considered in [7] and [138]. There, the material parameters are assumed to be constant across the UWB frequency range and the available solutions are based on simplifying assumptions that are not valid for most building materials. Therefore, these methods do not provide practical information about pulse distortion. Many experimental results for electromagnetic (EM) parameters of commonly used building materials over a wide frequency range show the frequency dependency of the material parameters. We refer readers to [32] and [112] for a review of some measurement results. The available information on frequency-dependent material parameters facilitates theoretical and simulated study of physical effects in the frequency domain. The analysis of the effects of walls on UWB pulses in Chapter 3 is based on permittivity and conductivity *functions* of commonly used building materials given in [28].

In our analysis of pulse distortion phenomena occurring in indoor BB channels, we focus on the pulse waveform distortion and delay dispersion of UWB signals due to reflection from and transmission through a lossy dielectric wall and its correspondence with standardized channel models for UWB systems [88]. We use frequency-domain methods. We consider the aspects of pulse responses that influence UWB and BB mm-wave channel modellings. The significance of the distortions due to lossy dielectric walls of different building materials are compared. The pulses created by multiple internal reflections of wall surfaces are considered. The maximum correlation coefficient (MCC) [13, 60, 64] is used as a measure of the distortion of individual pulses compared to the incident pulse. MCC is a measure of the maximum energy that can be captured from each received pulse when the transmitted pulse shape is used as the reference pulse

shape at the receiver.

Our contributions in Chapter 3 can be summarised as:

1. Including realistic frequency dependence of the parameters of materials in indoor environments over an ultra-wide frequency range.

2. Developing the MCC as a measure of the degree of distortion caused by surface reflections/transmissions and internal material distortion for multiple reflections and transmissions.

3. Inclusion of per-path pulse distortions, multiple internal reflections caused by lossy dielectric walls and derivation of PDPs for reflections from and transmissions through walls.

4. Theoretical explanation of the clustering and a soft onset phenomenon due to walls.

The results are based on the information provided by ITU's recommendation [96] about the frequency-dependent permittivity and conductivity of some commonly used building materials. In the graphs and simulation results presented in this chapter, we have focused on frequency ranges that are pertinent to UWB communication systems complying with the standard IEEE 802.15.4-2011 [2][6]. A similar approach can be used to analyse the pulse distortion phenomena and derive TDL models for responses of single or multilayer wall structures over the frequency ranges pertinent to mm-wave communication systems [109], in particular, those compliant with the standard IEEE 802.11ad.

1.5 Adaptive MMSE Equaliser for BB Channels

A linearly modulated transmit signal can be represented as [102]

$$s(t) = \sum_n \mathrm{d}_n p(t - nT), \tag{1.4}$$

[6]This standard has been superseded by the standard IEEE 802.15.4-2015 [3].

where $\{d_n\}$ is the sequence of complex data symbols, $p(t)$ is the pulse shaping filter's impulse response (IR), and T is the symbol interval. The two-sided bandwidth of $p(t)$ is usually less than $2/T$ and more than $1/T$. Therefore, according to the sampling theorem of Shannon [102], $T/2$-spaced samples of the received signal, $r(t)$, from a linear channel form a characterizing set. That is, $r(t)$ can be reconstructed from these samples and the samples can be used in a digital receiver to perform synchronization and equalization with no performance loss. Theoretically, any sampling rate satisfying the conditions of the sampling theorem [43] can be used, but due to its simple implementation, $2/T$ is the most common sampling rate [147, 42, 105].

A popular linear equaliser that is designed to perform channel equalization using $T/2$-spaced samples of the received signal is the FS MMSE equaliser [102]. When the sampling rate is $2/T$, the FS MMSE equaliser is implemented using a TDL filter whose tap spacing is $T/2$ [105, 102]. A major advantage of the FS MMSE equaliser over its SS counterpart is its capability to compensate for sampling phase errors (which result in band edge distortions) and any other linear distortion caused by the communication channel [147, 42, 102].

Using the celebrated FS LMS algorithm [147, 40, 102, 8], the FS MMSE equaliser can be implemented adaptively. Adaptivity, simplicity and low complexity are major advantages of the LMS algorithm for equalizing *a priori* unknown and slowly time-varying channels [47, 117].

It is well known that the optimum infinite-length $T/2$-spaced MMSE equaliser is not unique, but the corresponding suboptimal finite-length MMSE equaliser is unique [41, 40, 105]. Therefore, when the LMS algorithm is convergent, it will converge (in mean) to this unique solution. A major drawback of FS LMS algorithm is its non-convergence and instability [41]. This is due to the increasing magnitudes of some of the equaliser tap weights and the additive noise [41]. A TDL equaliser with large tap gains is sensitive to input perturbations. Since in the LMS algorithm noisy estimates of the gradient of the MSE surface are used to update the tap weights [102], the FS LMS algorithm is unstable. According to this argument, in order to stabilize the FS LMS algorithm, the tap gains of the equaliser should be restricted to small values. Usually this is done by modifying the cost function of the MMSE estimation, that is,

by defining the modified cost function by [147, 41, 117]

$$J_\mu(\mathbf{q}) = J_{\mathrm{MSE}}(\mathbf{q}) + \mu\|\mathbf{q}\|^2, \tag{1.5}$$

where $\mathbf{q}$ is the equaliser tap-weight vector, $J_{\mathrm{MSE}}(\mathbf{q})$ is the MMSE estimation cost function, $\|\cdot\|$ denotes Euclidean norm and μ is the tap-leakage parameter [147, 41, 117]. The modified cost function penalizes the squared norm of the vector $\mathbf{q}$, and therefore, the tap gains cannot grow large when this modified cost function is used. The modified LMS algorithm based on the cost function $J_\mu(\mathbf{q})$ is referred to as the tap-leakage algorithm [41] or the leaky LMS algorithm [47, 117].

By using the tap-leakage method the vanishing eigenvalues of the input samples correlation matrix can be removed, but this does not guarantee the convergence of the adaptive algorithm. Convergence of the modified LMS (leaky LMS) algorithm still depends on the eigenvalue spread of the correlation matrix.

There is a major difference between the SS sampling receiver and FS sampling receiver. Since the FS sampled received signal is not a wide-sense stationary process, the channel correlation matrix is not Toeplitz. Therefore, the impulse response (IR) and TF of the corresponding MMSE equaliser are time-variant. The Fourier transform, which is commonly used for derivation of the TF of the SS MMSE equaliser [40, 102, 117], cannot be used directly to study the eigenvalues of the correlation matrix of a FS sampled signal or to derive the TF of the FS MMSE equaliser. In this chapter, an explicit formula for the TF of the FS MMSE equaliser is derived. Using the TF, all aspects of the FS MMSE equaliser can be studied.

The stability analysis of the adaptive FS equaliser, implemented using the LMS algorithm, is usually based on simplifying assumptions or approximations. For instance the analysis in [147] relies on a two-stage approximation of the channel correlation matrix. The first is the approximation of a non-Toeplitz channel matrix by a Toeplitz matrix and the second is the approximation of a non-cyclic Toeplitz matrix by a cyclic Toeplitz matrix. In the course of these approximations, the sources of instability are avoided.

Using the TF of the FS MMSE equaliser, we show that the increasing tap weight magnitudes by recursion of the LMS algorithm can be a natural consequence of two

phenomena: 1) constructive addition of frequency domain sinusoidals corresponding to time domain TDL filter over some frequency intervals over which the equaliser does not have control, 2) sampling time offsets which create spectral dips over the rolloff regions of the transmitted pulse. Then, the appropriate approach to control the tap weight magnitudes is introduced.

Our approach to spectral analysis of the FS MMSE equaliser is different from the existing methods. The existing analyses of the FS MMSE equaliser are based on the statistical properties (covariance matrix) of the input sampled signal to the equaliser. Therefore, the behaviour of the equaliser is indirectly speculated using the statistical properties of the input data. In this chapter, the properties of the FS MMSE equaliser are studied based on the derived TF of the optimum FS MMSE equaliser.

The contributions of Chapter 4 are:

1. Derivation of the TF of a FS MMSE equaliser (the Wiener solution for an FS MMSE equaliser) that includes the effects of the channel components: transmit filter, propagation channel, receiver C/D converter and the sampling phase.
2. Analysis of the effects of the sampling phase on FS MMSE equaliser's TF.
3. Analysis of the effects of the C/D converter on the performance of FS MMSE equaliser and LMS algorithm.
4. Investigation of the convergence and stability of the LMS algorithm using properties of the optimum solution.
5. Explanation of the effect of equaliser length on the stability of the LMS algorithm.
6. Introduction of ensemble-averaged equaliser norm as an appropriate tool for stability analysis of the LMS algorithm.

1.6 Summary of Original Contributions and Publications

The original contributions of this thesis are summarised as follows.

1. Derivation of the *baseband model* for wireless BB communication channels that include the frequency dependent effects of the channel. In this model, per pulse

distortions due to antennas and propagation effects are modelled as filters for individual paths and the Doppler effect is modelled as a combination of the carrier frequency shift and the envelope dilation. Using this model, the front end C/D converter of a digital receiver described in such a way that its output DT signal provides a sufficient statistic for any optimum digital receiver. Chapter 2 includes these results.

2. Physical description of the clustering effect of indoor BB channels by performing *pulse distortion analysis* and derivation of PDP models for walls and partitions. The approach is novel, extendible and the obtained results are compatible with experimental models available in the literature. These results are presented in Chapter 4 and has been published in the following paper

   > G. Narimani, P. A. Martin, and D. P. Taylor. "Analysis of Ultrawideband Pulse Due to Lossy Dielectric Walls and Indoor Channel Models". In: *IEEE Trans. Antennas. Propag.* 64.10 (2016), pp. 4423–4433.

3. Derivation of an explicit formula for the TF of FS MMSE equaliser for the first time. It includes the effects of the pulse shaping filter, the channel and the receiver front-end C/D converter. It also includes, explicitly, effects of the prefilter and sampling rate used in the C/D converter. The derived formula is new and provides more insights on behaviour of the adaptive FS MMSE equalisers. The formula is used to study convergence and stability of the FS LMS algorithm. Based on the insights provided by the formula, the sources of instability of FS LMS algorithm are described and a stabilisation method is proposed. The proposed method has superior performance compared to the popular tap-leakage regularisation method. These results are presented in Chapter 4 and will appear in the IEEE Transactions on Communications:

   > G. Narimani, P. A. Martin, and D. P. Taylor. "Spectral Analysis of Fractionally-Spaced MMSE Equalisers and Stability of the LMS Algorithm". In: *IEEE Trans. Commun.* (2017). (Accepted)

Chapter 2

Discrete-Time Models for BB Channels

Synopsis A mathematical formula for a lowpass received signal from a generic linear time-variant wireless channel with additive white Gaussian noise is derived. It includes arbitrary linear filtering effects due to the transmission and reception equipments (connectors, antennas) and the frequency-dependent propagation channel effects (multipath, distortions by lossy dielectric obstacles and Doppler shifts). Therefore, it is a generalisation of the traditional narrowband (NB) received signal model appropriate for broadband (BB) channels. The theory of shift-invariant subspaces (SISs) of finite-energy signals is used to find a discrete-time (DT) model for the channel that captures all characteristics of the continuous-time (CT) model. This approach does not suffer from the ideality of the Shannon sampling theorem, i.e., it is realisable and more compatible with practical channel and receiver front-end processing.

2.1 Introduction

A wireless channel is usually characterized as a time-variant linear filter having an equivalent lowpass impulse response (IR) $h(t, \tau)$ and an additive zero-mean Gaussian noise process, $z(t)$ [102]. Therefore, the channel response to an equivalent lowpass signal $s(t)$ can be represented by

$$r(t) = \int_{\mathbb{R}} h(t, \tau) s(t - \tau) \, \mathrm{d}\tau + z(t). \tag{2.1}$$

The noise free received signal

$$u(t) = \int_{\mathbb{R}} h(t,\tau)s(t-\tau)\,\mathrm{d}\tau, \tag{2.2}$$

is the most general form of a signal at the output of a time-variant linear filter. For a particular wireless channel the IR may include effects due to antennas, propagation channel, mobility and filtering at the transmitter and receiver. Also, if the transmitter and receiver are not properly frequency synchronized, the residual frequency after down-conversion appears as a rotating phasor in the lowpass IR.

The responses of antennas and the propagation channel effects are frequency dependent. The propagation channel effects include reflection from and transmission through planar objects, scattering by rough surfaces, diffraction by edges and the Doppler. In practical applications, the significance of frequency dependency due to channel effects and the antenna response depends on the bandwidth of the signal, the channel dynamics, and the geometrical and electrical characteristics of the antennas and the interacting objects in the environment.

The bandwidths used by most traditional communication systems are sufficiently narrow that any frequency dependency of most of the physical effects can be safely ignored [137, 26]. In channel modelling based on the NB assumption, three effects are usually considered: 1) delay dispersion, 2) small-scale fading, and 3) large-scale fading (or, shadowing) [99, 102]. Small-scale fading is due to multipath propagation of the signal in the communication environment and to mobility. Delay dispersion can be due to multipath propagation and/or pulse distortion (deffuse or non-resolvable multipath). In NB channel models, per-pulse distortion is ignored. Therefore, multipath propagation is considered to be the only source of delay dispersion. A received multipath component can correspond to the line-of-sight path or can be the resultant of interactions of the transmit pulse with one or several objects in the environment. Each received pulse is accompanied by a multiplicative phasor due to the carrier sinusoidal wave. The multiplicative phasors can have different phases as they have undergone different physical interactions with objects and due to differences on their travelling distances on the order of wavelength of the carrier wave. As a result, a received multipath component's amplitude is determined by the addition of several phasors which can

be constructive or deconstructive. The multipath component's amplitude will change with displacements of the transmitter, receiver and/or the objects on the order the carrier wavelength. The carrier wavelength is usually small compared to the pulse length in NB communication systems, and hence, the multipath component's amplitude variation due to small displacements is referred to as small-scale fading. The large-scale fading or shadowing effect is caused by large objects that cause long-term signal attenuation by shadowing.

Most existing channel models are based on the NB assumption, and therefore, are valid for channels with relatively narrow bandwidth. Mathematical modelling for broadband wireless channels, where the transmit pulse bandwidth is several GHz, is a relatively new field. The existing information about the propagation mechanism of broadband signals in various environments have mainly been obtained by experiments [26, 86, 109]. Some of these experimental results have been used in [88] to formulate a model for UWB channels in order to provide a platform for evaluation of communication systems designed based on the IEEE 802.15.4a standard[1]. Understanding the propagation mechanisms of BB pulses in a communication environment is an important step toward finding appropriate channel models for BB channels. A chapter of this thesis is devoted to an analytical study of one of many propagation mechanisms. Specifically, in Chapter 3, using basic principles of electromagnetics, we study the interactions of an UWB pulse with single and multilayer walls. There, it is shown that the clustering effect, the soft onset phenomenon and small-scale fading observed in experimental UWB channel models can be related to interactions of UWB pulses with multilayer structures like walls, windows and partitions abundantly available in indoor communication environments.

In principle, any model for a physical communication channel serves two major purposes: 1) it provides a tool for testing various communication strategies by adopting appropriate modulation and demodulation techniques; 2) it provides a model for the received signal and hence a receiver can be designed based on certain optimality criteria. In Chapter 4, we will consider receiver design for a broadband channel based on the minimum mean-square error (MMSE) criteria. Therefore, certain stability problems that are important issues in designing adaptive receivers for single carrier

[1]IEEE 802.15.4a was superseded by IEEE 802.15.4-2011.

broadband systems are discussed. Since modern receivers are digital-intensive, the front-end receiver C/D converter needs to be incorporated into the received DT signal model.

The first task of an all-digital receiver is the extraction of a denumerable set of variables from the received CT signal $r(t)$ that include all information about the channel $h(t,\tau)$ and the transmitted signal $s(t)$ available in the signal $u(t)$. Since the channel and the data are in general random, the extracted variables are random. This set of random variables, denoted by $\mathbf{T}[r(t)]$, is referred to as a sufficient statistic. For establishing reliable coherent communication, knowing the channel, the carrier phase and symbol timing are crucial [102, 77]. Therefore, an optimum digital receiver should be able to acquire this information from the discrete-time (DT) signal $\mathbf{T}[r(t)]$.

This chapter has two goals. The first goal is to derive a mathematical formula for the lowpass received broadband signal that takes into account the frequency dependency of channel components. This is a fundamental step in studying the physical layer (PHY) of any communication system.

The second goal of this chapter is to design front-end receiver C/D converters that provide a sufficient statistic for any optimum digital receiver. It is well-known that for a linear channel with AWGN, and any linear modulation scheme, a sufficient statistic is obtained by the symbol time-spaced samples of the output of the matched filter [34, 102]. For a real pulse shape $p(t)$ and a linearly modulated lowpass transmit signal

$$s(t) = \sum_{n=0}^{N} \mathrm{d}_n p(t - nT), \tag{2.3}$$

the IR of the matched filter is defined by $h_{MF}(t) = \int_{\mathbb{R}} \overline{h(-t,\tau)} p(-t-\tau)\,\mathrm{d}\tau$, where the overbar indicates complex conjugation. Then a sufficient statistic is

$$\mathbf{T}[r(t)] = \{r * h_{MF}(kT - \tau_0) : k = 0, \cdots, N\}, \tag{2.4}$$

where τ_0 is the channel delay. The variables required for performing matched filtering are: 1) channel delay, τ_0; 2) symbol interval, T; 3) channel IR; 4) carrier frequency, f_c; and 5) carrier phase. Usually, this information is not initially available at the receiver front end and must be acquired from the DT signal using DSP methods. Under

this condition, the statistic characterised by (2.4) is not observable at the receiver. The matched filter maximizes the signal-to-noise ratio of the samples when the symbols are transmitted individually (without intersymbol interference) and τ_0 is known. This, together with the property of providing a sufficient statistic are the theoretical advantages of matched filtering.

When the channel is rapidly varying, in the sense that channel IR changes within a duration shorter than the effective delay spread of the channel, only a genie can realize a matched filter! Because in this case the channel changes before its response is wholly observed at the receiver and hence the receiver's information about the channel is always aged. We will not consider such a rapidly varying (fast fading) channel conditions. If a statistical description of the channel variation is available, then the performance of a communication system including the modulation scheme and the receiver structure can be studied statistically [100, 125, 14].

The performance study of any digital communication system operating over a given CT channel requires a discrete model for the channel that approximates the discretisation procedure that occurs in practical digital receivers. Therefore, our goal is to derive a discrete model with the following properties:

1. The DT model captures all characteristics of the CT channel, in the sense that the CT channel can be characterized by the DT model.

2. It is realizable, in the sense that the DT model's variables are practically observable.

In information-theoretic studies of communication systems, using the matched filter is the most common discretisation approach [102, 12, 8]. However, in practice matched filtering is rarely possible as the information required for its implementation may not be available *a priori*. Channel estimation procedures and synchronisation subsystems are used to estimate the channel IR and the symbol and carrier parameters. To do so digitally, first a DT sufficient statistic is extracted from the received CT signal. This is done by using an invariant front-end lowpass filter (prefilter) and a fixed sampling rate. Then, DSP is used to obtain channel information and synchronisation parameters from the DT sufficient statistic. But with unknown channel IR and/or

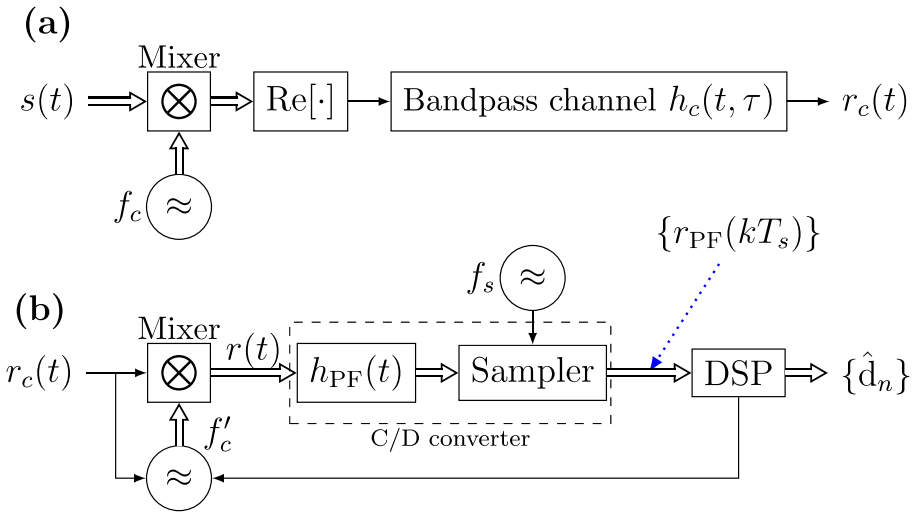

Figure 2.1: Digital communication system. Real-valued signal flows are shown by single-line arrows and the complex-valued signal flows are shown with double-line arrows. (a) Creation of the real bandpass received signal $r_c(t)$. (b) Processing blocks in the front-end of a typical digital receiver [77, 15, 143].

synchronisation parameters, SS samples do not provide sufficient statistics. The last point will be discussed in detail in the next section.

In practical receivers, instead of the matched filter, other filters are used for pre-filtering and the sampling rate of the filter output is usually higher than the symbol rate [15, 40, 102, 132]. Accordingly, the main building blocks of a typical all-digital receiver are as shown in Fig. 2.1 (b). Detailed block diagrams can be found in [15] and [77].

In Fig. 2.1 (b), the input is a real bandpass signal $r_{\rm c}(t)$. A coarse estimate f_c' of the carrier frequency f_c, is used to down-convert the received signal to a complex lowpass signal $r(t)$. Due to the frequency offset $f_c' - f_c$ and phase offset θ_0, a rotating phasor $\exp\left(\mathrm{j}\,2\pi([f_c' - f_c]t + \theta_0)\right)$ appears in the down-converted signal. The lowpass signal $r(t)$ is passed through a lowpass filter, referred to as prefilter, with impulse response $h_{\rm PF}(t)$. The output of the lowpass filter is sampled at a rate f_s. The sampling rate f_s is provided by a free-running oscillator. In general, the transmission symbol rate $\frac{1}{T}$ is incommensurate with the sampling rate f_s [77]. The DT signal from the output of the sampler is forwarded to the DSP units where the quantized values are processed to produce the final decision variables $\{\hat{\rm d}_n\}$, in the transmission symbol rate $\frac{1}{T}$ [77].

The DSP block in Fig. 2.1 encompasses many sub-blocks performing required tasks for carrier and symbol-timing synchronisations, channel estimation and equalisation. Among these tasks, we will consider equalisation in fractionally-spaced sampling receivers in Chapter 4 where we focus on one of the most important linear equalisation techniques referred to as fractionally-spaced minimum mean-square error (FS MMSE) equalisers and their adaptive implementation using the LMS algorithm.

Over a time interval longer that the coherence time of the channel [102], the phase $\theta_0(t)$ and the IR, $h(t, \tau)$, are functions of the time t. For a short duration, which usually spans several symbol intervals [102], they can be assumed to be constant with respect to t. That is, $h(t, \tau) = h(\tau)$ and $\theta_0(t) = \theta_0$. In the design of the prefilter and the sampler, the long term behaviour of these functions must be taken into account. For synchronisation, channel estimation and equalisation, understanding the time variations of the channel is crucial [77].

The earlier research works on UWB channel modelling were mainly focused on carrier-free transmission which is usually called impulse radio [161, 162, 23]. In this case, the local oscillators creating sinusoidal waves with frequencies f_s and f_c' and the mixers in Fig. 2.1 are not required. After the first report and order on UWB technology issued by Federal Communications Commission (FCC) in United States [31], the research partially shifted from IR to carrier-based transmission. The FCC report and order specified the spectral masks for maximum emission power from the UWB transmit antennas. This FCC regulation was followed by similar regulations in Europe and other places [26].

An advantage of IR radio is communication without using local oscillators and mixers at transmitters and receivers. With the current regulations concerning UWB technology deployment, the carrier-based transmission is preferred for the following reasons:

- Better spectrum utilization by dividing the useful UWB frequency band into several sub-bands.
- Satisfying the strict emission power limitations by employing suitable spectrally flat pulse shapes, such as the square-root raised cosine (SRRC) pulse, and a variety of interesting linear modulation schemes [102].

- Reducing the power usage at the receiver by performing DSP at baseband. Due to significant path-dependent pulse distortions, the superposition of the received UWB pulses from different paths have no resemblance to the transmitted one. Therefore, performing analogue matched filtering is very difficult, if not impossible. Therefore, characterization of the received signal and matched filtering need to be done in the digital domain. Down-conversion of a passband signal to baseband reduces the sampling rate required for DSP [102].[2]

For carrier-based wireless communication channels important determining factors are the dedicated frequency band (i.e., the bandwidth and the carrier frequency), the physical effects of the channel (including antennas) on the transmitted radio frequency (RF) signals in that frequency band and, the dynamics of the environment [99]. Specifically in broadband communications these factors should not be studied independently as most effects of the propagation environment and antennas depend on the frequency content of the transmitted signal waveforms [37, 159, 104, 103].

2.2 Lowpass Received Signal Model

Characterization of the transmission channel is important for determination of optimum and sub-optimum transceiver designs and their comparative performance studies [9]. The baseband representation of the received RF signal is required for the design of baseband receiver front-end, to perform baseband DSP at the receiver, and study its performance [102]. An appropriate equivalent baseband model for a channel includes the effects of the propagation channel and the antennas.

In spite of the importance of an equivalent baseband channel model for broadband communications, the derivation of a baseband model for these channels has only been considered in [10] with some simplifying assumptions such as ignoring the directivity of the antennas filtering effects and the frequency dependency of reflections, diffractions and scattering from objects. These are the distinctive characteristics of broadband channels and they should be incorporated into the model. This fact has

[2]There is a method called transmitted reference technique to overcome the problem of unknown pulse distortions of the channel [52], however, it reduces the channel capacity, C, to $\frac{C}{2L}$, where L is the delay spread of the channel.

been emphasized in several research papers including [104, 103, 101, 37, 166, 89, 85].

In this section, we derive the baseband equivalent channel model for carrier-based broadband systems under general assumptions on the transmit and receive antennas and physical propagation mechanisms. More specifically, in this work the antennas are modelled as arbitrary directional filters, the reflections, scatterings and diffractions are modelled as filters, and the Doppler effect is modelled as dilation (time scaling) operators. Also, the differences of the derived model with the NB channel models are discussed.

We consider a system that employs a linear modulation scheme to transmit the data over a linear wireless multipath channel. In such systems, the effects of channel on the linearly modulated and sequentially transmitted signal is completely characterized by the effects of the channel on the normalized pulse-shaping filter's IR.

2.2.1 Lowpass transmit signal

Consider a real bandpass signal $s(t)$ with complex envelope $s_{\mathrm{b}}(t)$, such that

$$s(t) = \Re\{s_{\mathrm{b}}(t)\mathrm{e}^{\mathrm{j}\,2\pi f_c t}\}, \tag{2.5}$$

where $\Re$ denotes the real part of a complex number and f_c is the carrier or centre frequency. In carrier-based communication systems the real bandpass signal $s(t)$ is fed to the transmit antenna. The antennas and the propagation channel affect $s(t)$ with a variety of mechanisms before it arrives at the receiver. We will discuss these effects shortly. Our aim is to translate these effects into baseband and, consequently, formulate the complex envelope of the received signal.

We assume that the modulation scheme used for communication is linear and full response. Then

$$s_{\mathrm{b}}(t) = \sum_n \mathrm{d}_n\, p(t - nT_s), \tag{2.6}$$

where $\{\mathrm{d}_n\}$ is a complex data symbol sequence, T_s is symbol period, and $p(t)$ is a real signal called the amplitude shaping pulse. We assume that the channel is linear. Therefore, for complete characterization of the communication channel we need only to consider the effects of the channel on the amplitude shaping pulse, $p(t)$.

We consider a system that consists of a transmit network, a transmit antenna, a propagation channel, a receive antenna, and a receive network. For example, the circuit model of a transmit network and the transmit antenna can be visualised as shown in Fig. 2.2. By restricting our attention to the amplitude shaping filter, the task of the transmit network is to generate a voltage signal $p(t)$ and mix it with the carrier signal $\cos(2\pi f_c t)$ generated by a local oscillator and feed the transmit antenna with the real signal $v_T(t) = p(t)\cos(2\pi f_c t)$. The circuit model of a receive network is similar to that of a transmit network, but in a receive network the direction of the current is reversed.

We now consider the key effects of the channel on the transmitted signal $v_T(t)$.

2.2.2 Physical channel effects

Studies of UWB communication channels reveal that the degrees of freedom in the received signal and its statistical properties such as small scale and large scale fadings are impacted by the frequency content[3] of the transmitted signal pulses [23, 68, 88]. This necessitates careful consideration of the physical effects of broadband channels, including antennas, on the transmitted pulses and finding an appropriate model for the channel that incorporates these effects.

The transmit and receive antenna effects

The antennas are essential parts of any wireless communication system and their properties have to be taken into account in system design and performance evaluation. Traditionally, in NB wireless communication systems, antennas are characterized by their gain, directivity, polarization and voltage reflection coefficient [6, p. 94]. These characteristics are usually used in link budget analysis. These characteristics are frequency-dependent. The gain, directivity and polarization depend on the directions of transmission and reception. For NB communication systems the frequency dependence of antenna effects are usually regarded only for the centre (or carrier) frequency of the signals. This can be justified only for NB signals where the radiated electric fields resemble a time-harmonic field [6]. Since the antenna characteristics change significantly with respect to frequency content of ultra-wide bandwidth signals, for BB communica-

[3]The frequency content of a signal $s(t)$ is $\{f : S(f) \neq 0\}$.

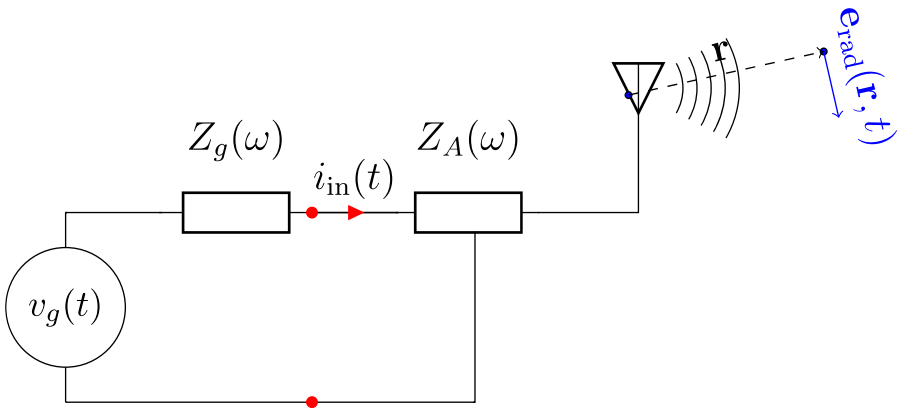

Figure 2.2: Circuit model for a transmit network.

tions, antenna characteristics have to be considered over an ultra-wide frequency range [141, 120, 167, 159].

In order to incorporate the frequency-dependency of the antenna effects we use the concept of *vector effective length* [6, 123, 126, p. 87]. Frequency-dependent polarization properties of an antenna in the far field region can be described by its vector effective length. With reference to Figure 2.2, assume that the input current wave at the antenna terminals is $i_{\text{in}}(t)$ with Fourier transform $I_{\text{in}}(f)$. The (approximate) electric field in the far field region of the antenna induced by $i_{\text{in}}(t)$ is denoted by $\mathbf{e}_{\text{rad}}(\mathbf{r},t)$, where $\mathbf{r}$ is the position vector of the point in space with respect to a coordinate system with its origin located at the center of the antenna. The vector effective length $\mathbf{h}^t(\hat{\mathbf{r}},t)$ is defined, in the Fourier domain, by

$$\mathbf{E}_{\text{rad}}(\mathbf{r},\omega) = -\mathrm{j}\omega\eta\frac{\mathrm{e}^{\mathrm{j}\omega\frac{r}{c}}}{4\pi rc}I_{\text{in}}(w)\mathbf{H}^t(\hat{\mathbf{r}},\omega), \tag{2.7}$$

where

$$\mathbf{E}_{\text{rad}}(\mathbf{r},\omega) = \int_{\mathbb{R}}\mathbf{e}_{\text{rad}}(\mathbf{r},t)\mathrm{e}^{-\mathrm{j}\omega t}\,\mathrm{d}t, \quad \mathbf{H}^t(\hat{\mathbf{r}},\omega) = \int_{\mathbb{R}}\mathbf{h}^t(\hat{\mathbf{r}},t)\mathrm{e}^{-\mathrm{j}\omega t}\,\mathrm{d}t, \tag{2.8}$$

η is the intrinsic impedance of free space, and $\hat{\mathbf{r}} = \frac{1}{r}\mathbf{r}$ is the unit vector in the direction of $\mathbf{r}$. The integrals of vector functions in (2.8) are calculated component-wise.

With this definition, the vector effective length, $\mathbf{h}^t(\hat{\mathbf{r}}, t)$, of the transmit antenna is a complex vector-valued function of the spatial direction ($\hat{\mathbf{r}}$), and time (t). But it is independent of the distance r from the antenna centre.

The definition of the vector effective length given by (2.7) does not include the impedance of the signal generator $Z_g(\omega)$. In order to relate the voltage waveform generated by the signal generator to the far field radiation (and hence to the vector effective length), assume that the transmit antenna has load impedance $Z_A(\omega)$ when it is excited by a harmonic signal with frequency ω. Then $I_{\text{in}}(\omega) = V_g(w)/(Z_g(\omega) + Z_A(\omega))$. Therefore, by (2.7)

$$\mathbf{E}_{\text{rad}}(\mathbf{r}, \omega) = -\mathrm{j}\omega\eta \frac{\mathrm{e}^{\mathrm{j}\omega\frac{r}{c}}}{4\pi r c} \frac{V_g(w)}{Z_g(\omega) + Z_A(\omega)} \mathbf{H}^t(\hat{\mathbf{r}}, \omega). \tag{2.9}$$

By reciprocity theorem, it can be shown [126, 123, 127] that the open circuit voltage $V_L(w)$ at the terminals of a receiving antenna is given in terms of the vector effective length, $\mathbf{H}^r(\hat{\mathbf{r}}, \omega)$, of the receiving antenna and the incident electric field $\mathbf{E}_{\text{inc}}(\hat{\mathrm{r}}, \omega)$ by

$$V_L(\hat{\mathrm{r}}, \omega) = \mathbf{E}_{\text{inc}}(\hat{\mathbf{r}}, \omega) \cdot \mathbf{H}^r(\hat{\mathbf{r}}, \omega). \tag{2.10}$$

In (2.10), $\hat{\mathbf{r}}$ denotes a unit vector with respect to a coordinate system with its origin located at the centre of the receive antenna.

The consequence of the representations (2.9) and (2.10) is that both transmitting and receiving antennas *in each direction* act as time-invariant linear filters. Therefore, they can be modelled as integral operators with convolutional kernels [53], where the kernels are angle dependent. The Fourier transform of these kernels, i.e., the TFs of the filters are given by (2.9) and (2.10). The vector function notation used in the above discussion means that the transmitting antenna not only decomposes the input signal into two components in two orthogonal polarisation directions but also filters each component. The receiving antenna combines the received electric field components after filtering each of them.

The signals received from non-line-of-sight (NLOS) paths experience several changes before arriving at the receive antenna. For example, depolarisations, phase changes, Doppler shifts and losses due to reflection, diffraction and scattering. Therefore, for NLOS paths these effects should be taken into account.

For static channels all of these effects can be modelled as time-invariant linear filters. As such, we may correspond to each occurrence of these effects a linear operator with a convolutional kernel [53]. For dynamic channels, the mobility of the channel components results in Doppler frequency shifts. The Doppler effect is time variant and cannot be represented as a convolution operator. When the relative speeds of the transmitter, receiver and the interacting object are pairwise constant, the Doppler effect can be modelled as a time dilation operator [157].

The frequency dependency of the atmospheric effects in microwave and mm-wave frequencies is usually insignificant for communication applications [96], but it is higher around the 60 GHz band. For mm-wave communication over a long distance the frequency dependency around 60 GHz bandwidth can cause pulse distortion. For short range communications this causes insignificant distortion. Note that the standard IEEE 802.11ad [1] using 60 GHz bandwidth has been planned for communications over ranges below 10 metres.

2.2.3 Lowpass received signal

The multipath channel model that we consider is different from traditional multipath models. In a traditional multipath model, each received pulse from a single path is considered undistorted. That is, each received pulse can be represented by $a_\kappa p_{\mathrm{c}}(t-\tau_\kappa)$, where $p_{\mathrm{c}}(t) = \Re\{p(t)\mathrm{e}^{\mathrm{j}2\pi f_c t}\} = p(t)\cos(2\pi f_c t)$ is the real passband pulse corresponding to a real baseband pulse $p(t)$, a_κ is a complex number referred to as the path gain and τ_κ is the path delay.

In the model presented below, along with path gain and path delay, two linear distortions are also included. Namely, the distortion caused by frequency dependent channel effects associated with each path and the Doppler effect. Considering all effects

on the pulse together, the pulse response of a single path, indicated by the index κ, can be represented as $a_\kappa(t)\left[h_\kappa(t) * p_{\mathrm{c}}\big(\nu_\kappa t - \tau_\kappa\big)\right]$, where τ_κ is the delay with respect to the transmit time $t_0 = 0$, ν_κ is the Doppler dilation due to movements of the path's interacting objects with constant velocities, $h_\kappa(t)$ is the impulse response of the path including direction dependent filtering effects of the transmit and receive antennas, and $a_\kappa(t)$ is the time-variant attenuation due to mobility. The angle of departure and the angle of arrival for each path is absorbed in the index κ. The Doppler dilation due to constant velocity v_κ in the direction of propagation of the signal is given by $\nu_\kappa = 1 \pm \frac{v_\kappa}{c}$ [45]. The impulse response of the κth path is due to the frequency-dependent reflection and transmission and diffraction coefficients. For BB communication channels, such as UWB and mm-wave channels, consideration of the frequency-dependency of the channel effects is necessary [85, 23, 67, 135].

The total pulse response of the channel is given by the aggregation of all pulses received from several single paths. Therefore, the pulse response of the channel is represented by

$$x_{\mathrm{c}}(t) = \sum_{\kappa \in I} a_\kappa(t)\left[h_\kappa(t) * p_{\mathrm{c}}\big(\nu_\kappa t - \tau_\kappa\big)\right], \tag{2.11}$$

where the index set I corresponds to the set of all active paths at time instant t.

For NB signals it is usually assumed that $h_\kappa(t) = \delta(t)$ and the Doppler effect is modelled as a pure frequency shift of the carrier wave. That is, the effect of Doppler time scaling on the envelope of the carrier modulated pulse, $p_{\mathrm{c}}(t)$, is ignored. Note that the envelope of this pulse is $p(t)$. The time duration of the pulse $p_{\mathrm{c}}(t)$ is usually very short and the dynamic change in the environment over this duration is insignificant. Therefore, the attenuation coefficient $a_\kappa(t)$ corresponding to each received pulse can be assumed constant; $a_\kappa(t) = a_\kappa$.

In (2.11) all parameters, a_κ, ν_κ and τ_κ, are deterministic. $p_{\mathrm{c}}(t)$ is the real passband transmitted pulse and $x_{\mathrm{c}}(t)$ is the corresponding real passband received signal. We refer to (2.11) as *the deterministic channel pulse response* to the pulse $p_{\mathrm{c}}(t)$. Next, we want to derive the equivalent baseband channel model. Let $p(t)$ denote the baseband pulse. Then

$$p_{\mathrm{c}}(t) = \Re\left\{p(t)\mathrm{e}^{\mathrm{j}\,2\pi f_c t}\right\}, \tag{2.12}$$

where f_c is the carrier frequency. By (2.11)

$$\begin{aligned} x_{\rm c}(t) &= \sum_{\kappa\in I} a_\kappa \left[h_\kappa(t) * \Re\left\{p(\nu_\kappa t-\tau_\kappa){\rm e}^{{\rm j}2\pi f_c(\nu_\kappa t-\tau_\kappa)}\right\}\right] \\ &= \Re\Big\{ \sum_{\kappa\in I} a_\kappa \ \left[h_\kappa(t) * \left(p(\nu_\kappa t-\tau_\kappa){\rm e}^{{\rm j}2\pi f_c(\nu_\kappa t-\tau_\kappa)}\right)\right] \Big\} \\ &= \Re\Big\{ \sum_{\kappa\in I} a_\kappa {\rm e}^{-{\rm j}2\pi f_c\tau_\kappa} \ \left[h_\kappa(t) * \left({\rm e}^{{\rm j}2\pi\nu_\kappa f_c t}p(\nu_\kappa t-\tau_\kappa)\right)\right] \Big\} \\ &= \Re\Big\{ {\rm e}^{{\rm j}2\pi f_c t}\Big(\sum_{\kappa\in I} a_\kappa {\rm e}^{-{\rm j}2\pi f_c\tau_\kappa}\times \\ &\qquad \left[\left({\rm e}^{-{\rm j}2\pi f_c t}h_\kappa(t)\right) * \left({\rm e}^{{\rm j}2\pi(\nu_\kappa-1)f_c t}p(\nu_\kappa t-\tau_\kappa)\right)\right] \Big) \Big\}. \end{aligned} \tag{2.13}$$

Therefore, with reference to (2.12), the complex baseband input-output relationship is

$$x(t) = \sum_{\kappa\in I} a_\kappa {\rm e}^{-{\rm j}2\pi f_c\tau_\kappa}\left({\rm e}^{-{\rm j}2\pi f_c t}h_\kappa(t)\right) * \left({\rm e}^{{\rm j}2\pi(\nu_\kappa-1)f_c t}p(\nu_\kappa t-\tau_\kappa)\right). \tag{2.14}$$

The received signal model in (2.14) is *the deterministic equivalent lowpass* model. In the case that the carrier frequency is not known at the receiver, the receiver mixer uses a coarse approximate f_c' of f_c for down-conversion. Then the received signal model becomes

$$x(t) = {\rm e}^{{\rm j}2\pi f_\epsilon t}\sum_{\kappa\in I} a_\kappa {\rm e}^{-{\rm j}2\pi f_c\tau_\kappa}\left({\rm e}^{-{\rm j}2\pi f_c t}h_\kappa(t)\right) * \tag{2.15}$$

$$\left({\rm e}^{{\rm j}2\pi(\nu_\kappa-1)f_c t}p(\nu_\kappa t-\tau_\kappa)\right), \tag{2.16}$$

where $f_\epsilon = f_c - f_c'$.

Derivation of the lowpass received signal model as presented above is not based on the NB assumption, and therefore, is valid for time-variant broadband wireless channels. In the following, we will obtain the baseband model based on the NB assumption. We will see that the commonly used wide-sense stationary uncorrelated scattering (WSSUS) model can be obtained from (2.14) after applying several approximations that might not be valid for BB channels.

A1 In (2.14), for a given κ, when the velocity $v_\kappa \neq 0$, the Doppler scaling $\nu_\kappa \neq 1$. Therefore, the Doppler has two effects: 1) carrier frequency shifting due to the

factor $e^{j2\pi(\nu_\kappa-1)f_c t}$, and 2) pulse dilation[4]. In channel models based on the NB assumption, the pulse dilation due to Doppler is ignored (i.e., $\nu = 1$) and the Doppler effect is only considered as a shift of the carrier frequency.

A2 In NB channel modelling per-path pulse distortions are ignored, i.e., in NB channel modelling it is assumed that $h_\kappa(t) = \delta(t)$ for all $\kappa \in I$.

A3 In derivation a TDL filter model for channels based on the NB assumption, the total relative delay spread of the channel with respect to the first received pulse is divided into several delay bins in which the widths of delay bins are usually equal to the reciprocal of the channel bandwidth, W. That is, assuming a channel with relative delay spread T_d,

$$[0, T_d] = [0, 1/W] \cup [1/W, 2/W] \cup \cdots \cup [(L_{\mathrm{NB}} - 1)/W, L_{\mathrm{NB}}/W], \tag{2.17}$$

where $L_{\mathrm{NB}} = \lfloor T_d W + 1 \rfloor$ is the number of taps of the TDL filter. Then the following approximation is used:

$$p(t - \tau_\kappa) \approx p(t - m_i) \tag{2.18}$$

for all τ_κ satisfying $\frac{i}{W} \leq \tau_\kappa < \frac{i+1}{W}$. In (2.18), $m_i = \frac{2i+1}{2W}$ is the middle point of the interval $B_i = [\frac{i-1}{W}, \frac{i}{W}]$. The approximation in (2.18) is only justifiable when $|\tau_\kappa| \ll 1/W$.

By applying the approximations mentioned above the following TDL model for channel can be obtained from (2.15)

$$x_{\mathrm{NB}}(t) = \sum_{i=0}^{L_{\mathrm{NB}}-1} \gamma_i(t) p(t - m_i), \tag{2.19}$$

where

$$\gamma_i(t) = e^{j2\pi f_\epsilon t} \sum_{\tau_\kappa \in B_i} a_\kappa e^{-j2\pi f_c \tau_\kappa} e^{j2\pi(\nu_\kappa - 1) f_c t}, \tag{2.20}$$

[4] $p(\nu_\kappa t - \tau_\kappa)$ is a dilated version of $p(t - \tau_\kappa)$.

for $i = 0, \cdots, L_{\mathrm{NB}} - 1$, are the time-varying channel coefficients. Using the equality $\nu_\kappa = 1 + \frac{v_\kappa \cos(\theta_\kappa)}{c}$ where θ_κ is the angle of arrival of the κth pulse relative to the direction of motion of the κth scatterer with constant velocity v_κ, (2.20) can be expressed as

$$\gamma_i(t) = \mathrm{e}^{\mathrm{j}\,2\pi f_\epsilon t} \sum_{\tau_\kappa \in B_i} a_\kappa \mathrm{e}^{-\mathrm{j}\,2\pi f_c \tau_\kappa} \mathrm{e}^{\mathrm{j}\,2\pi v_\kappa \cos(\theta_\kappa) f_c t/c} \tag{2.21}$$

$$= \mathrm{e}^{\mathrm{j}\,2\pi f_\epsilon t} \sum_{\tau_\kappa \in B_i} a_\kappa \mathrm{e}^{-\mathrm{j}\,2\pi f_c \tau_\kappa} \mathrm{e}^{\mathrm{j}\,2\pi f_{D,\kappa} t} \tag{2.22}$$

where $f_{D,\kappa} = v_\kappa \cos(\theta_\kappa) f_c/c$ is the Doppler shift of the κth path. The impact of the factors $\mathrm{e}^{\mathrm{j}\,2\pi f_{D,\kappa} t}$ on the time variation $\gamma_i(t)$ is slight due to existence of the $c = 3 \times 10^8$ in the denominator of their exponents. When some of the scatterers are moving with large velocities these factors can result in NB Doppler frequency spread in the received signal. A small change in path lengths results in small changes in path delays, $\tau_\kappa,\ \kappa \in I$. Due to the existence of the factor f_c, constructive and deconstructive addition of the exponential functions present sudden changes in channel coefficients.

2.2.4 WSSUS assumption and BB channel models

In statistical channel modelling of NB channels two other assumptions are common. These are the wide-sense stationarity (WSS) and uncorrelated scattering (US) assumptions [9, 102]. We say that the channel model (2.19) satisfies the WSS assumption if $\mathrm{E}[\gamma_{i_1}(t_1)\overline{\gamma_{i_2}(t_2)}]$ for any pair (i_1, i_2) depends only on the difference $\Delta t = t_1 - t_2$ and not on the individual time instants t_1 and t_2. Mathematically, the WSS condition can be stated as

$$\mathrm{E}[\gamma_{i_1}(t_1)\overline{\gamma_{i_2}(t_2)}] = \mathcal{R}(\Delta t, i_1, i_2), \tag{2.23}$$

where $\mathcal{R}$ is the correlation function of the two-parameter process $\gamma_i(t)$.

We say that the channel model (2.19) satisfies the US assumption if at each time instant $t = t_0$ and any $i_1 \neq i_2$, the two random variables $\gamma_{i_1}(t_0)$ and $\gamma_{i_2}(t_0)$ are uncorrelated, that is, $\mathrm{E}[\gamma_{i_1}(t_0)\overline{\gamma_{i_2}(t_0)}] = 0$. Putting WSS and US assumptions together, the channel is said to satisfy the WSSUS assumption if $\mathrm{E_i}[\mathrm{E_t}[\gamma_{i_1}(t_1)\overline{\gamma_{i_2}(t_2)}]]$ is equal to zero when $i_1 \neq i_2$, and is a function of $\Delta t = t_1 - t_2$ and $i_1 (= i_2)$ otherwise. In other words,

it satisfies the WSSUS assumption if $\mathrm{E_i}[\mathrm{E_t}[\gamma_{i_1}(t_1)\overline{\gamma_{i_2}(t_2)}]]$ can be written as

$$\mathrm{E_i}[\mathrm{E_t}[\gamma_{i_1}(t_1)\overline{\gamma_{i_2}(t_2)}]] = \mathcal{R}(\Delta t, i_1, i_2)\delta(i_1 - i_2), \tag{2.24}$$

where δ is the Dirac delta function. Note that $\gamma_i(t)$ is a two parameter random process with parameters i and t. To emphasise that, we have used two mathematical expectation operators with indices i and t.

When the channel bandwidth, W, is small, the number of MPCs falling within each delay bin will be large[5]. Then using the central limit theorem (CLT) each $\gamma_i(t)$ can be modelled as a wide-sense stationary Gaussian process. For BB channels with large absolute bandwidth the possibility of a large number of MPCs falling within a single delay bin decreases. As a result, the Gaussian process model for coefficients of channel with large absolute bandwidth is not appropriate if the communication is not in a sufficiently dense multipath environment [20].

2.3 Shift Invariant Signal Subspaces and Realizable Discretisations

We focus on the part of the receiver which is indicated by a dashed rectangle in Fig. 2.1 (b). This part of a digital receiver converts the CT received signal to a DT signal. For this reason, a digital communication system can be analysed using a DT system model. A theoretical and simulated evaluation of a system is valid if the adopted DT model captures all important characteristics of the real CT channel and the C/D conversion performed in the receiver.

The capability of the DSP units in performing the fundamental tasks of the receiver including channel estimation, synchronization and equalization depends on the characteristics of the prefilter and sampler. Therefore, we are interested in DT characterizations of the input-output relation (2.1), which encompasses the part of the system from the output of the modulator at the transmitter to the output of the sampler at the receiver, with the following properties:

P1 They can be implemented by using realizable filters, $h_{\mathrm{PF}}(t)$, and constant rate (f_s) sampling, as in Fig. 2.1 (b). (Realizability)

[5]This still depends on how dense the scatterers are in the communication environment.

P2 The output DT signal, $\{r_k\} = \mathbf{T}[r(t)]$, provides a sufficient statistic for the relevant information contained in the received signal.

P3 The noise samples z_k are uncorrelated: $\mathbf{E}[z_{k_1} z_{k_2}^*] = N_0 \delta(k_1 - k_2)$. (White noise)

Absolutely bandlimited filters are not realizable. By realizability we mean a filter whose tails do not carry significant energy, in the sense of Landau and Pollak [65].

The required memory and the computational complexity of the digital processing increases with the increase of the number of samples per symbol. For broadband communication systems such as UWB [26] and mm-wave [109] where the transmission bandwidth is extremely large this increase in the sampling rate and the subsequent processing might be unaffordable. Property **P3** is useful in evaluation of the performance as well as implementation of an optimum receiver when the DT signal is used as an input to an equaliser and detector that performs according to a maximum-likelihood criteria such as maximum-likelihood sequence detection (MLSD) or minimum mean-square error (MMSE) criteria [102] (See also the discussion in [77, p. 700].). Optimality of these receivers depend on the correlation of the noise samples. If the noise is not white, a noise whitening filter is required before feeding the noisy samples to the optimum receiver. When the correlation matrix of the noise samples is singular or ill-conditioned, the noise cannot be whitened by linear filtering. This can cause serious instability problems for optimum receivers designed based on the white noise assumption. For the case of MMSE receivers, this problem is analysed and addressed in Chapter 5.

The properties **P2** and **P3** can be satisfied by choosing the ideal brick-wall filter with sufficiently large bandwidth as the prefilter and sampling its output exactly at the Nyquist rate. The sampling model based on the sampling expansion is the most commonly adopted model in the theoretical analysis of the communication systems [40, 102, 145]. But it is not practically interesting as it is not easy to approximate the ideal brick-wall filter by using practical filters.

The conditions on the prefilter in order for the samples to provide a sufficient statistic were considered in [76] and [77]. The authors have used a reversibility argument to prove the sufficiency of the statistics. The sufficiency of conditions mentioned there can be formally proved using a generalized version of the sampling theorem [11,

Theorem 1.2]. However, those conditions do not imply property **P3**.

In general, discretisation methods use a set of basis functions to expand a hypothetical received signal. The expansions are assumed (or, proved) to be valid for a subspace of signals that include the set of all expected received signals. Due to the basis property, the expansion coefficients uniquely characterize the received signal in the signal space generated by the basis functions and, consequently, they contain all information available in the CT signal. When the CT received signal is modelled as a stochastic process, the expansion coefficients are random variables characterising the CT stochastic process.

In discretisations based on the Shannon sampling theorem, the basis functions are the shifts of the sinc function [59, 9]. Other expansion methods include the Karhunen-Loève series expansion [102, 150], expansions in terms of the prolate spheroidal wave functions [25], orthonormal bases expansions obtained by the Gram-Schmidt procedure [132], and wavelet bases expansions [168]. The OFDM symbols can also be described as an orthonormal expansion where the basis functions are time and frequency shifted versions of a single function. These time and frequency shifted functions are referred to as Gabor (or Weyl-Heisebnerg) basis [43]. Non-orthogonal expansions are also studied in [118] and many other papers. Some of these theoretical discretisation approaches are non-realizable, computationally complex or require *a priori* knowledge of the channel. Therefore, most receivers employ an approximation of the sampling model where the sinc filter is approximated by another realizable lowpass filter. But no other lowpass filter enjoys the exceptional properties of the ideal sinc filter. Therefore, the extracted statistic does not necessarily satisfy the properties **P1**-**P3**.

A close relative of the sinc function is the family of Nyquist and square-root Nyquist pulses which are usually used for pulse shaping. Therefore, the receiver filter is sometimes matched to the transmitted signal pulse [102, 132]. It can be shown that the samples of the output of this filter taken at the symbol rate does not provide a sufficient statistics if the channel distorts the pulse or the channel delay is unknown (and the samples are not taken at appropriate times). In order to have a sufficient statistic, sampling at least at the Nyquist rate for the received signal is required [40, 102]. Increasing the sampling rate beyond the symbol rate causes other problems; the

noise samples do not satisfy the property **P3** and the complexity increases.

Our next goal is derivation of a DT model that can be closely approximated in practice. In particular, the prefilter, $h_{\mathrm{PF}}(t)$ and the sampling rate, f_s, are characterized in such a way that the samples satisfy the properties **P1**-**P3**. To this end a signal space description of the communication system is used where the transmitted and received signals belong to some SI subspaces of $\mathcal{L}_2$ (Section 2.3). The channel is then modelled as an operator between these spaces and the properties **P1**-**P3** are described in terms of the geometry of the signal spaces and operators. Under certain conditions, we characterize the family of prefilters ($h_{\mathrm{PF}}(t)$) and the corresponding sampling frequencies (f_s) that satisfy **P1**-**P3**.

2.3.1 SI subspaces

By a T-SI subspace of $\mathcal{L}_2$ we mean any closed linear subspace $\mathcal{S}$ of $\mathcal{L}_2$ which is closed under T-shifts, i.e., for each $g(t) \in \mathcal{S}$ we have $g(t - kT) \in \mathcal{S}$ for every $k \in \mathbb{Z}$. A T-SI subspace generated by $g(t)$ is the closed subspace of $\mathcal{L}_2$ generated by T-shifts of $g(t)$. It is denoted by $\mathcal{S}_T(g)$ and called a principal SI subspace. The theory of SI subspaces plays an important role in various areas of mathematical analysis and its applications, such as approximation theory [16], wavelet analysis [24, 156], sampling theory [4] and finite element methods [130]. SI subspaces arise in communication theory as well. Linearly modulated signals (2.3) belong to a SI subspace whose generator is the pulse shaping filter's impulse response and the coefficients are the data symbols. That is, $s(t) \in \mathcal{S}_T(p)$. Also, by denoting the IR of a communication channel with $h(t)$ and $p(t) * h(t)$ by $g(t)$, the noise-free received signal

$$u(t) = \sum_{n=0}^{N} \mathrm{d}_n g(t - nT), \tag{2.25}$$

belongs to the SI subspace $\mathcal{S}_T(g)$. Therefore, the cascade of the pulse shaping filter and the noise-free linear channel can be described as a linear operator that maps a data vector $[\mathrm{d}_0, \cdots, \mathrm{d}_n]$ into $\mathcal{S}_T(g)$.

In any modulation scheme, the symbols are chosen from a certain constellation and the domain of the aforementioned operator is restricted to a finite subset of $\mathbb{C}^n$.

Without this restriction on the data symbols and ignoring the additive noise, the problem of data detection is equivalent to this one:

Given $u(t) \in \mathcal{S}_T(g)$ find the coefficients d_i that satisfy (2.25).

In practice, usually the channel is not known and there is noise. Our information about the channel and the noise is limited. It is commonly assumed that the noise is a zero-mean white Gaussian process, the channel is linear and the received useful signal is band-limited to $|f| \leq B$, for some B. Because of the roll-off region of the transmitted pulse, the time variations of the channel and frequency offset between the transmitter and receiver oscillators, $2B$ is greater than the symbol rate $\frac{1}{T}$. In this case, $u(t) \in \mathcal{S}_{\frac{1}{2B}}(D_{2B}\mathrm{sinc})$ by Shannon's sampling theorem (but, $u(t) \notin \mathcal{S}_T(D_{\frac{1}{T}}\mathrm{sinc})$) and

$$u(t) = \sum_{k=-\infty}^{\infty} c_k \mathrm{sinc}\,(2Bt - k), \tag{2.26}$$

where the expansion coefficients are the regularly-spaced samples of the signal

$$c_k = u(\frac{k}{2B}), \quad k \in \mathbb{Z}. \tag{2.27}$$

The coefficients c_k satisfy properties **P2**-**P3**. The only problem is the non-realizability of the sinc function as impulse response of a practical filter (**P1**). This observation leads us to investigate the family of functions that can replace the sinc function and are realizable. That is, to investigate the family of functions $q(t)$ such that $u(t) \in \mathcal{S}_{\frac{1}{2B}}(q)$ and the coefficient c_k in the expansion

$$u(t) = \sum_{k=-\infty}^{\infty} c_k q(2Bt - k), \tag{2.28}$$

satisfy the properties **P1**-**P3**.

In the lack of a sampling theorem for general $q(t)$, we will use the received signal model (2.15) to find the appropriate SI subspace with a generator $q(t)$, satisfying the conditions **P1**-**P3**. We will show that if the SRRC function is used for pulse shaping, and the channel is linear, the received signal belongs to a family of SI spaces generated by orthonormal shifts of dilated versions of the SRRC function. In this section we

will provide the required theoretical background about SI subspaces generated by the SRRC function $p(t)$ defined in (2.30).

If the channel distorts the pulse (in any form), the receive signal space, in general, will be different from the transmit signal space as the generator of the space has been distorted. Therefore, a generalization of the signal space notion for general channels is required.

The use of the SRRC function in this work is not accidental. The reason is its exceptional properties which make it a suitable pulse shape for transmission and reception. From an implementation point of view it is desirable because it is realizable to an acceptable order of approximation. From a theoretical point of view it is desirable because i) it is band-limited and decays rapidly in time (asymptotically as $\frac{1}{|t|^3}$), ii) its time shifts by integer numbers are orthonormal and iii) its convolution with itself is a sampling function and has the zero ISI property (Nyquist pulse). The results can be generalised to any bandlimited Nyquist pulse with sampling property.

The SRRC function is defined by

$$P(f) = \begin{cases} \frac{1}{\sqrt{R}}, & |f| \leq \frac{R}{2} - \beta \\ \frac{1}{\sqrt{R}} \cos\left(\frac{\pi}{4\beta}\left(|f| - \frac{R}{2} + \beta\right)\right), & \frac{R}{2} - \beta < |f| \leq \frac{R}{2} + \beta \\ 0, & \text{otherwise,} \end{cases} \tag{2.29}$$

in the frequency domain, and by

$$p(t) = \frac{\sin\left(2\pi t(\frac{R}{2} - \beta)\right) + 8\beta t \cos\left(2\pi t(\frac{R}{2} + \beta)\right)}{\pi\sqrt{R}t\left(1 - (8\beta t)^2\right)}, \tag{2.30}$$

in the time domain. In (2.29) and (2.30), the parameters R and β are the Nyquist bandwidth and excess bandwidth of the pulse $p(t)$ respectively. Usually, the rolloff factor $\alpha \triangleq \frac{2\beta}{R}$ is used to define the SRRC pulse [102]. (2.30) can be derived from (2.29) by straightforward but tedious calculation of the inverse Fourier transform. The SRRC function is usually expressed using the rolloff factor defined by $\alpha = 2\beta/R$, see (3.1). The raised cosine function (RC) in the time domain is

$$\forall f \in \mathbb{R},\ q(t) = p(t) * p(t) = \text{sinc}\,(Rt)\frac{\cos(2\beta\pi t)}{1 - (4\beta t)^2}. \tag{2.31}$$

The Fourier transform of the RC function is given by $Q(f) = P(f)^2$ and satisfies the following identity

$$\sum_{k\in\mathbb{Z}} |Q(f - kR)| \equiv \frac{1}{R}. \tag{2.32}$$

(2.32) has two important consequences:

1. The RC function, $q(t)$ has the zero ISI property [102].

2. The set of shifted SRRC functions $\{T_{kT_\circ}p(t)|\, k \in \mathbb{Z}\}$ is an orthonormal set in $\mathcal{L}_2$[24]. (It is not a basis for $\mathcal{L}_2$, as it is not complete.)

Now we formally define the SI subspaces of $\mathcal{L}_2(\mathbf{R})$.

Definition 2.3.1. Let $T \in \mathbb{R}$ and $\phi(t) \in \mathcal{L}_2$. The $T-$SI subspace generated by $\phi(t)$ is the closed complex linear span of the set of all shifts of $\phi(t)$ by integer multiples of T in $\mathcal{L}_2$. That is

$$S_T(\phi(t)) := \overline{\text{span}}\,\{\phi(\cdot - kT)|\, k \in \mathbb{Z}\}\,, \tag{2.33}$$

where $\overline{\text{span}}$ denotes the closed linear span [21].

When the shifts of the generator are orthogonal, the SI spaces have a simple characterization. Assume that $\{\phi(t - kT)\}$ is an orthogonal set and $g(t) \in S_T(\phi(t))$. There exists a unique $\{c_k\} \in \ell^2(\mathbb{Z})$ such that $g(t) = \sum_{k\in\mathbb{Z}} c_k\phi(t - kT)$. Applying the Fourier transform we have

$$\begin{aligned} G(f) &= \mathcal{F}\left[\sum_{k\in\mathbb{Z}} c_k\phi(t - kT)\right] \\ &= \left(\sum_{k\in\mathbb{Z}} c_k \mathrm{e}^{-\mathrm{j}2k\pi kTf}\right)\Phi(f), \end{aligned} \tag{2.34}$$

where $\mathcal{M}(f) = \sum_{k\in\mathbb{Z}} c_k \mathrm{e}^{-\mathrm{j}2k\pi kTf}$ is a $\frac{1}{T}$–periodic function which belongs to $\mathcal{L}_2[-\frac{1}{2T}, \frac{1}{2T}]$. Therefore, $g(t) \in S_T(\phi(t))$ if and only if there exists $\mathcal{M}(f) \in \mathcal{L}_2[-\frac{1}{2T}, \frac{1}{2T}]$ such that $G(f) = \mathcal{M}(f)\Phi(f)$. It can be shown that $\mathcal{M}(f)$ is equal to the folded spectrum of $\phi(t)$, i.e., $\mathcal{M}(f) = \sum_{k\in\mathbb{Z}} |\Phi(f - \frac{k}{T})|^2$. By the definition of the SI-subspaces 2.3.1, with $T_\circ = \frac{1}{R}$ and $p(t)$ equal to the SRRC function, $\{T_{kT_\circ}p(t)|\, k \in \mathbb{Z}\}$ is an orthonormal basis for $S_{T_\circ}(p(t))$.

The following theorem provides the mathematical foundation for our pulse shaping and reception method. For its statement, we need the following notation: for an operator A and a set $V = \{v_n : \ n \in N\}$ of functions we define AV as

$$AV = \{Av_n : \ n \in N\}, \tag{2.35}$$

which is called the image of V under A.In this theorem, and the rest of this chapter, we will use the SRRC function defined as in (3.1).

Theorem 2.3.1. *Let $p(t)$ denote the SRRC function. Then*

1. *$D_r S_{T_\circ}(p(t)) = S_{\frac{T_\circ}{r}}(D_r p(t))$, and $\{T_{\frac{kT_\circ}{r}} D_r p(t) | k \in \mathbb{Z}\}$ is an orthonormal basis for the space $D_r S_{T_\circ}(p(t))$, for all $r \in \mathbb{R}$,.*

2. *Dilation invariance: $D_{r_1} S_{T_\circ}(p(t)) \subseteq D_{r_2} S_{T_\circ}(p(t))$ for $r_1, r_2 \in \mathbb{R}$ if and only if $r_1(1 + \frac{2\beta}{R}) \leq r_2$.*

3. *Translation invariance: $T_\tau D_{r_1} S_{T_\circ}(p(t)) \subseteq D_{r_2} S_{T_\circ}(p(t))$ for $\tau, r_1, r_2 \in \mathbb{R}$ if and only if $r_1(1 + \frac{2\beta}{R}) \leq r_2$.*

4. *Modulation invariance: $M_\theta D_{r_1} S_{T_\circ}(p(t)) \subseteq D_{r_2} S_{T_\circ}(p(t))$ if and only if*

$$|\theta| \leq (r_2 - r_1)\frac{1}{2T_\circ} - r_1\beta.$$

5. *Phase shift invariance: $P_\phi D_r S_{T_\circ}(p(t)) = D_r S_{T_\circ}(p(t))$, for all $r \in \mathbb{R}$.*

6. *Linear distortion invariance: $l(t) * D_{r_1} S_{T_\circ}(p(t)) \subseteq D_{r_2} S_{T_\circ}(p(t))$ if and only if the restriction of $L(f)$ to the interval $[-\beta - \frac{r_1}{2T_s}, \beta + \frac{r_1}{2T_s}]$ is an essentially bounded function (i.e. belongs to $\mathcal{L}_\infty[-\beta - \frac{r_1}{2T_s}, \beta + \frac{r_1}{2T_s}]$) and $r_1(1 + \frac{2\beta}{R}) \leq r_2$.*

Proof. 1. Let $g(t) \in D_r S_{T_\circ}(p(t))$. Then there exists $\{c_k\} \in \ell^2(\mathbb{Z})$ such that $g(t) = D_r\left(\sum_{k\in\mathbb{Z}} c_k p(t - kT_\circ)\right)$. Since D_r is a continuous (unitary) operator and the

series is convergent, we may interchange D_r with the summation to write

$$\begin{aligned} g(t) &= \sum_{k\in\mathbb{Z}} c_k D_r p(t - kT_\circ) \qquad (2.36)\\ &= \sum_{k\in\mathbb{Z}} c_k \sqrt{r} p(rt - kT_\circ) \\ &= \sum_{k\in\mathbb{Z}} c_k \sqrt{r} p\left(r(t - \frac{kT_\circ}{r})\right) \\ &= \sum_{k\in\mathbb{Z}} c_k \sqrt{r} T_{\frac{kT_\circ}{r}} p(rt) \\ &= \sum_{k\in\mathbb{Z}} c_k T_{\frac{kT_\circ}{r}} D_r p(t). \qquad (2.37) \end{aligned}$$

The RHS of equality (2.37) belongs to $S_{\frac{T_\circ}{r}}(D_r p(t))$. The reverse inclusion is also evident from this equality.

Since D_r is a unitary operator on $\mathcal{L}_2$, it maps any orthonormal set onto an orthonormal set. Therefore, the generating set $\{T_{\frac{kT_\circ}{r}} D_r p(t) | k \in \mathbb{Z}\}$ is an orthonormal basis for the space $D_r S_{T_\circ}(p(t))$.

2. Since $D_{r_1}^{-1} = D_{\frac{1}{r_1}}$, by applying $D_{r_1}^{-1}$ to both sides of $D_{r_1} S_{T_\circ}(p(t)) \subseteq D_{r_2} S_{T_\circ}(p(t))$, we see that the statement of theorem is equivalent to $S_{T_\circ}(p(t)) \subseteq D_r S_{T_\circ}(p(t))$ for $r \geq 1 + \frac{2\beta}{R}$. Let $g(t) \in S_{T_\circ}(p(t))$. Then $G(f) = M(f)P(f)$ for a $\frac{1}{T_\circ}$–periodic function in $L^2[-\frac{1}{T_\circ}, \frac{1}{T_\circ}]$. By part 1, $g(t) \in D_r S_{T_\circ}(p(t))$ if and only if there exists a $\frac{r}{T_\circ}$–periodic function in $L^2[-\frac{r}{2T_\circ}, \frac{r}{2T_\circ}]$ such that $G(f) = M'(f) D_{\frac{1}{r}} P(f)$. Since $r > 1$ (for $\beta > 0$, which excludes the sinc function), $D_{\frac{1}{r}} P(f) \neq 0$ for $f \in [-\frac{1}{2T_\circ}, \frac{1}{2T_\circ}]$. Therefore, we may define

$$M_1(f) = \begin{cases} \frac{M(f)P(f)}{D_{\frac{1}{r}} P(f)} & \text{if } f \in [-\beta - \frac{1}{2T_\circ}, \beta + \frac{1}{2T_\circ}] \\ 0 & \text{otherwise,} \end{cases} \qquad (2.38)$$

and

$$M'(f) = \sum_{k\in\mathbb{Z}} M_1\left(f - \frac{rk}{T_\circ}\right). \qquad (2.39)$$

Then $M'(f)$ is $\frac{r}{T_\circ}$–periodic. It belongs to $\mathcal{L}_2[-\frac{r}{T_\circ}, \frac{r}{T_\circ}]$ because $D_{\frac{1}{r}} P(f)$ is bounded

away from zero over the interval $[-\frac{1}{2T_\circ}, \frac{1}{2T_\circ}]$. Also we have

$$M'(f)D_{\frac{1}{r}}P(f) = M(f)(P(f)) = G(f).$$

That is $g(t) \in D_r S_{T_\circ}(p(t))$.

3. Similar to the proof of part 2, we may assume that $r_1 = 1$ and $r = r_2 > 1 + \frac{2\beta}{R}$. The proof follows the same procedure as in the proof of part 2 and defining $M_1(f)$ as in (2.38) with $M(f)$ replaced by $\mathrm{e}^{-\mathrm{j}2\pi\tau f}M(f)$.

4. The proof is the same as the proof of part 2, with $M(f)$ in (2.38) replaced by $M(f-\theta)$.

5. All SI spaces are invariant with respect to constant multipliers especially phase shifts which are complex numbers with absolute value 1.

6. Let $g(t) \in l(t) * D_{r_1}S_{T_\circ}(p(t))$. Then there exists $g_1(t) \in D_{r_1}S_{T_\circ}(p(t))$ such that $g(t) = l(t) * g_1(t)$ and $G_1(f) = M(f)D_{\frac{1}{r_1}}P(f)$ for some $\frac{r_1}{T_\circ}$–periodic function $M(f) \in L^2[-\frac{r_1}{2T_\circ}, \frac{r_1}{2T_\circ}]$. Define

$$M_1(f) = \begin{cases} \frac{L(f)M(f)D_{\frac{1}{r_1}}P(f)}{D_{\frac{1}{r_2}}P(f)} & \text{if } f \in [-\beta - \frac{r_1}{2T_\circ}, \beta + \frac{r_1}{2T_\circ}] \\ 0 & \text{otherwise,} \end{cases} \tag{2.40}$$

and

$$M'(f) = \sum_{k\in\mathbb{Z}} M_1\left(f - \frac{r_2 k}{T_\circ}\right). \tag{2.41}$$

On the interval $[-\beta - \frac{r_1}{2T_\circ}, \beta + \frac{r_1}{2T_\circ}]$, $D_{\frac{1}{r_2}}P(f)$ is bounded away from zero and $L(f)$ is bounded. Therefore, $M'(f) \in \mathcal{L}_2[-\frac{r_2}{2T_\circ}, \frac{r_2}{2T_\circ}]$ and is $\frac{r_2}{2T_\circ}$–periodic. On the other hand $M'(f)D_{\frac{1}{r_2}}P(f) = L(f)M(f)D_{\frac{1}{r_1}}P(f) = G(f)$, which means that $g(t) \in D_{\frac{1}{r_2}}S_{T_\circ}(p(t))$, by part 1.

□

Remark. In Theorem 2.3.1, part 6 is equivalent to parts 3 and 5. ($6 \iff 3, 5$)

2.3.2 The transmit and receive signal subspaces

Assume that the transmitted signal has the complex envelope

$$s_{\mathrm{b}}(t) = \sum_{n=0}^{\infty} \mathrm{d}_n p(t - nT) \tag{2.42}$$

where $\{\mathrm{d}_n\}$ represents the discrete information bearing sequence of symbols (real or complex), $p(t)$ is the SRRC function defined by (3.1) and $T = \frac{1}{R}$. By the definition of SI subspaces, we see that $s_{\mathrm{b}}(t) \in S_{T_\circ}(p(t))$. For this reason, we call $S_{T_\circ}(p(t))$ the transmit signal space.

Now assume that the real passband signal $s_{\mathrm{p}}(t) = \Re\{s_{\mathrm{b}}(t)\mathrm{e}^{\mathrm{j}\,2\pi f_c t}\}$ is fed to the transmit antenna connector and transmitted through the channel. Depending on the channel and the antennas, the received signal from the receiving antenna's connector, $r_{\mathrm{p}}(t)$, is different from the transmitted signal. Whatever the channel effects are, the received signal still has finite energy, that is, $r_{\mathrm{p}}(t) \in \mathcal{L}_2$. The complex envelope of $r_{\mathrm{p}}(t)$, namely $r_{\mathrm{b}}(t)$ also has finite energy: $r_{\mathrm{b}}(t) \in \mathcal{L}_2$. An important step in designing an efficient receiver is to characterise a structured subspace of $\mathcal{L}_2$ that includes the received signal characterized by (2.14). By a structured subspace we mean a subspace with a suitable basis that permits to expand the received CT signals in a stable way. Then the DT signal obtained by expansion coefficients can be used for processing and decision making using DSP methods in a digital receiver.

Characterization of the receive signal space depends on our description of the channel effects. Based on the received signal formula (2.14), we will characterize the smallest receive signal space for the system. Evidently, the receive signal space also depends on the pulse shape employed by the system. Characterization of the smallest receive signal space is useful in rejecting the irrelevant parts, such as irrelevant out-of-band noise components and interferences, from the received signal.

The following theorem characterises the received signal space as SI subspaces of $\mathcal{L}_2$ generated by dilated SRRC pulses.

Theorem 2.3.2. *Let $p(t)$ denote the SRRC function with roll-off factor β defined by (3.1). For a transmitted signal represented by (2.42), through a channel defined by the baseband input-output relationship (2.14), the received signal belongs to $S_{\frac{T_\circ}{r}}(D_r p(t))$,*

whenever $r \geq r_{\min} \triangleq \frac{2\beta}{R} + \max\left\{\nu_\kappa, 1 + \frac{2|\nu_\kappa - 1| f_c}{R} : \kappa \in I\right\}$. $r_{\min}$ *is the smallest real number such that* $S_{\frac{T_\circ}{r_{\min}}}(D_{r_{\min}} p(t))$ *contains the received signal (2.14).*

Proof. Defining the operators of phase shift, P_ϕ, modulation, M_θ, translation (or delay), T_τ, and dilation, D_r by

$$P_\phi p(t) = \mathrm{e}^{\mathrm{j}\phi} p(t), \tag{2.43}$$

$$M_\theta p(t) = \mathrm{e}^{\mathrm{j}2\pi\theta t} p(t), \tag{2.44}$$

$$T_\tau p(t) = p(t - \tau), \text{ and} \tag{2.45}$$

$$D_r p(t) = \sqrt{r} p(rt), \tag{2.46}$$

where $\phi, \theta, \tau \in \mathbb{R}$ and $r > 0$, the effects of the communication channel on the complex envelope of the transmitted pulse, $p(t)$ in (2.14), is a linear combination of composite operators of the form $P_\phi M_\theta T_\tau D_r$ and convolution with bandlimited finite energy functions, $h_\kappa(t)$. Therefore, Theorem 2.3.1 implies the result. □

Considering the special cases of interest, this theorem may be explained as follows. For a given channel we need some general information to design the optimum receiver. This information depends on the channel under study:

1. Assume that the channel is an ideal AWGN, i.e., the impulse response of the channel is equal to $\delta(t - \tau_0)$ [35], the transmission pulse shape is square-root Nyquist and there exists perfect time and frequency synchronisation between transmitter and receiver. Then, the optimum receiver consists of a filter matched to the transmitted pulse followed by a symbol-spaced sampler. If the pulse shape is not square-root Nyquist, this receiver would not be optimum. Also, without perfect synchronisation this receiver is not optimum. If the employed pulse is $\sqrt{R}\mathrm{sinc}\,(Rt)$ (corresponding to SRRC function with $\beta = 0$), perfect symbol timing synchronization is not required and still the receiver is optimum.

2. Assume that the channel is an ideal AWGN, the employed pulse is SRRC, and there exists perfect carrier frequency synchronisation but not perfect symbol timing and carrier phase synchronisation. Then, the optimum receiver depends on the roll-off factor, β, of the employed SRRC pulse, $p(t)$, for transmission. If

$\beta = 0$, the optimum receiver is as described in part 1. If $\beta \neq 0$, by Theorem 2.3.1, the optimum receiver consists of a filter with impulse response $D_{r_{\min}} p_1(t)$, where $r_{\min} = 1 + \frac{2\beta}{R}$ and $p_1(t)$ is a SRRC pulse with arbitrary roll-off factor, followed by sampling with rate $R + 2\beta$. Any other choice of the filter and the sampling rate will not result in an optimum filter. In the sense that if $r < r_{\min}$ is chosen, the samples do not provide a set of sufficient statistics, and if $r > r_{\min}$ is chosen, some parts of the irrelevant out-of-band noise and interference will not be suppressed. It is worth mentioning that with this choice of the receiver filter and the sampling rate, the receiver is not sensitive to symbol timing within one symbol interval and arbitrary carrier phase offsets.

3. If the channel is a linear time-invariant AWGN channel and the employed pulse shape is SRRC, $p(t)$, the optimum receiver consists of a filter with impulse response $D_{r_{\min}} p_1(t)$, where $r_{\min} = 1 + \frac{2\beta}{R}$ and $p_1(t)$ is a SRRC pulse with arbitrary rolloff factor, followed by sampling with the rate $R + 2\beta$. If $\beta = 0$, then the optimum receiver is as described in part 1. The optimum receiver structure is independent of the kind of the linear distortion and is insensitive to symbol timing errors and carrier phase offsets.

4. If the channel is time-varying, in the sense that the channel components including the transmit and the receive antennas and the scatterer are moving with constant speeds in the time interval of interest, the optimum receiver consists of a filter with impulse response $D_{r_{\min}} p(t)$ where

$$r_{\min} = \frac{2\beta}{R} + \max\left\{\nu_\kappa, 1 + \frac{2|\nu_\kappa - 1| f_c}{R} : \kappa \in I\right\},$$

and a sampler with the sampling rate rR. Each ν_κ corresponds to the Doppler dilation factor caused by overall relative speed of channel components participating in the κ-th path. The receiver is again independent of the symbol timing within a symbol interval.

Some comments about this theorem, that highlight its usefulness, are in order:

1. Theorem 2.3.2 implies that the received signal can be completely characterized by expansion coefficients with respect to the orthonormal basis $\{\sqrt{r} p_1(rt - kT_\circ) :$

$k \in \mathbb{Z}\}$, whenever $r \geq r_{\min}$ and $p_1(t)$ is a SRRC function with an arbitrary roll-off factor. When $r = r_{\min}$, the subspace generated by this orthonormal basis is the smallest with this property. Therefore, the projection of the noise process onto this subspace has the minimum power. Consequently, if $D_r p_1(t)$ is used as the front end filter at the receiver, the samples of the output will have the maximum signal-to-noise ratio (SNR) while providing a set of sufficient statistics.

2. The condition mentioned in Theorem 2.3.2 is sharp. In the sense that $\frac{2\beta}{R} + \max\{\nu_\kappa, 1 + \frac{2|\nu_\kappa - 1|f_c}{R} : \kappa \in I\}$ is the minimum possible value for r for perfect characterization of the received signal. This implies that $S_{\frac{T_\circ}{r_{\min}}}(D_{r_{\min}} p(t))$ is the smallest subspace of $\mathcal{L}_2$ that includes the received signal defined by (2.14).

3. By the proof, the result is independent of geometrical and material characteristics of the physical channel, the transmit and receive antennas efficiency and directivity, and path delays. That is, if the channel is static (time-invariant) and $r \geq 1 + \frac{2\beta}{R}$, the received signal belongs to $S_{\frac{T_\circ}{r}}(D_r p(t))$, irrespective of the antennas and other static characteristics of the channel.

4. In the case that frequency offset exists, such as due to synchronisation loss or frequency drifts in oscillators, with appropriate choice of r, the signal space $S_{\frac{T_\circ}{r}}(D_r p(t))$ contains the received signal which is modulated by the residual frequency. Particularly, if there is a frequency offset ξ between the transmitter and the receiver and

$$r \geq \frac{2\beta}{R} + \max\left\{\nu_\kappa, 1 + \frac{2|\nu_\kappa - 1|f_c + 2|\xi|}{R} : \kappa \in I\right\}, \tag{2.47}$$

then the receiver has the capability of compensating the frequency offset without requiring explicit frequency synchronization. This property is useful to define a tolerability threshold for the capability of the receiver to compensate for the frequency offsets. The only requirement is that the local oscillators at the transmitter and the receiver retain their frequency during the training and the data detection periods.

5. It is interesting to notice that the fractional bandwidth, $\frac{R}{f_c}$, the absolute bandwidth, R, and rolloff factor of the pulse shape, $\alpha \triangleq \frac{2\beta}{R}$, appear in (2.47). This

shows the importance of these channel parameters in designing an optimum receiver.

6. Oversampling the received signal at the output of the front end receiver filter, increases the complexity of the receiver as the complexity of equalisers increase with the number of samples per symbol [102]. A minimum number of required samples per symbol is crucial, especially in high data rate communication systems with long delay spread such as UWB, mm-wave and underwater acoustic (UWA) channels. Theorem 2.3.2 provides this minimum sampling rate which corresponds to the front end filter specified above, which is required for compensating various effects of the channel, antennas and synchronization errors.

2.4 The Optimum Receiver Structure

The optimum receiver for a given channel is generally defined as the one that minimizes the message error rate at the output of the detector [164, 102]. The cost function of this optimality criteria is the symbol error rate or the probability of error. This is an appropriate cost function because the channel and the noise are usually modelled as random processes. The transmitted symbols in any digital communication system are chosen from a finite set of complex or real numbers referred to as constellation points. When *a priori* knowledge about the information symbols is available, it can be used in manipulating the cost function. Following this approach gives rise to the maximum a posteriori probability (MAP) receiver [102]. When the information symbols are equiprobable, the MAP criteria reduces to the maximum likelihood (ML) criteria [102]. In the following, we assume that the information symbols are equiprobable.

Let us initially assume that the linear channel is time invariant, its lowpass equivalent impulse response is $h(t)$, and the additive noise is a white Gaussian process $z(t)$ with power spectral density $\sigma_z^2 = 2N_0$. In the case of one-shot transmission, when the transmitter sends a symbol d by using a pulse $p(t)$, the signal received by the receiver has a lowpass equivalent form given by

$$r(t) = \mathrm{d}p(t) * h(t) + z(t). \tag{2.48}$$

Without any constraint on the channel, $h(t)$, the received signal would be arbitrary and the optimum detection is not defined. In many cases $h(t)$ is unknown a priori. Using the time invariance of the channel, $p(t) * h(t)$ can be represented by a sufficient statistic $\mathbf{T}[p(t) * h(t)]$. The sufficient statistic is usually a sequence $\{c_n\}_{n\in\mathbb{Z}}$ obtained by using an orthonormal set of functions $\{g_n(t)\}_{n\in\mathbb{Z}}$ whose closed linear span includes $p(t) * h(t)$. More explicitly,

$$c_n = \langle p(t) * h(t), g_n(t)\rangle, \ \forall\, n. \tag{2.49}$$

The sufficient statistic $\mathbf{T}[p(t) * h(t)] = \{c_n\}_{n\in\mathbb{Z}}$ is a set of random variables. Since the additive noise is a white process, these random variables can be estimated arbitrarily closely by averaging many observations at the receiver, assuming that the channel is static during this averaging process.

Defining $r_n = \langle r(t), g_n(t)\rangle$ and $z_n = \langle z(t), g_n(t)\rangle$, we have

$$\mathbf{r} \triangleq \{r_n\} = \mathrm{d}\mathbf{c} + \mathbf{z}, \tag{2.50}$$

where $\mathbf{c} = \{c_n\}$, and $\mathbf{z} = \{z_n\}$ is a sequence of independent identically distributed (iid) normal random variables with zero mean and variance $2N_0$. (2.50) is the equivalent vector channel model of the waveform channel model (2.48). Since the components of $\mathbf{z}$ are normal iid random variables, the optimum receiver for the channel can be implemented by matched filtering in DT. Mathematically, the optimum detection rule according to ML is given by

$$\widehat{\mathrm{d}} = \arg\min_{\mathrm{d}\in\mathrm{D}} |\mathrm{d} - \frac{1}{\|\mathbf{c}\|^2}\langle \mathbf{r}, \mathbf{c}\rangle|, \tag{2.51}$$

where D is the set of all constellation points. Each component of the vector channel model (2.50) is an AWGN channel. Due to orthonormality of the basis, the noise components of these subchannels (i.e., the component channels) are independent and therefore, they can be described as diversity branches [56]. The matched filtering combines the diversity components by maximum-ratio combining method which is the optimum combining method for independent diversity branches. The equal gain combining is a

suboptimum combining method. Its detection rule is given by

$$\widehat{\mathrm{d}} = \arg\min_{\mathrm{d}\in\mathrm{D}} \|\mathbf{r} - \mathrm{d}\mathbf{c}\| \tag{2.52}$$

$$= \arg\min_{\mathrm{d}\in\mathrm{D}} \left\{ |\mathrm{d}|^2 - \frac{2\Re\left\{\mathrm{d}\,\langle \mathbf{r}, \mathbf{c}\rangle\right\}}{\|\mathbf{c}\|^2} \right\}. \tag{2.53}$$

The average SNRs at the output of the maximum-ratio and equal-gain combiners are respectively given by

$$\mathrm{SNR}_{MRC} = \frac{E[|\mathrm{d}|^2]\|\mathbf{c}\|^4}{E[|\langle \mathbf{z}, \mathbf{c}\rangle|^2]} = \frac{E[|\mathrm{d}|^2]\|\mathbf{c}\|^2}{2N_0}, \text{ and} \tag{2.54}$$

$$\mathrm{SNR}_{EGC} = \frac{E[|\mathrm{d}|^2]\|\mathbf{c}\|^2}{E[\|\mathbf{z}\|^2]} = \frac{E[|\mathrm{d}|^2]\|\mathbf{c}\|^2}{2LN_0}, \tag{2.55}$$

which shows that

$$\mathrm{SNR}_{MRC} = L \times \mathrm{SNR}_{EGC}, \tag{2.56}$$

where L is the number of orthonormal functions used for expansions or the number of independent diversity branches. The average SNR at the output when the MRC method is used is L-times larger than EGC method. This is true under the assumption of a perfectly known channel vector $\mathbf{c}$. Since the channel vector is used to weight the diversity branches, any error in its estimation will result in performance degradation of the optimum MRC method.

The possibility of realising a receiver that performs the channel estimation and data detection, according to the described method, depends on the realizability of the filters $\{g_n(t)\}$ used for derivation of the sufficient statistics. In theory, the Karhunen–Loève expansion method or the Gram-Schmidt procedure can be used. In CT it is not easy to implement these methods. They can be approximately implemented after discretisation at the cost of increased complexity. This reduces their practical value.

2.4.1 The RAKE demodulator

For an ideal AWGN channel the optimum receiver structure consists of a filter matched to the transmitted pulse followed by a sampler with the sampling rate equal to the symbol rate. The matched filter is required to capture the energy content of the useful signal and to suppress the additive noise as much as possible. For optimum

reception by this process, perfect time and frequency synchronizations are necessary [102]. Otherwise, it is not an optimum receiver. In the case of a non-ideal linear channel with AWGN, the optimum receiver consists of a matched filter, which is matched to the response of the channel to the employed pulse shape, followed by a symbol-spaced sampler. Therefore, in the case of non-ideal linear AWGN channels the receiver must have access to the channel pulse response and be synchronized with the transmitter in order to be able to provide the decision device with sufficient statistics and minimum noise power. Furthermore, for time-varying channels the receiver needs to be adaptive as the channel pulse response may change with time and synchronisation may be lost.

In practice, the pulse response of the channel is not known *a priori*. Therefore, for channel estimation, synchronisation and data detection purposes, the received CT baseband signal is passed through a low-pass filter with a large bandwidth to accommodate the bandwidth of the complex envelope of the transmitted signal and possible Doppler spreading introduced by the communication channel [102, 153]. Then, a set of sufficient statistics can be generated by sampling the filter output at a rate higher than or equal to the Nyquist rate. The sampling rate is usually an integer multiple of the symbol rate. This simplifies the later processing and the detection [102, 153, 30]. This set of sufficient statistics is used to estimate the channel pulse response and, time and frequency synchronisation. For data detection the number of samples is reduced to one sample per symbol by decimation [153]. The decimation might include an interpolation followed by symbol rate sampling. In this way, under some ideal conditions, one can get matched filtering performance. These ideal conditions are as follows:

1. The low-pass filter at the receiver is chosen in a way that passes all useful components of the received signal to the sampler, and at the same time suppresses the additive noise as much as possible.

2. Perfect time and frequency (sampling time, carrier frequency and carrier phase) synchronisation can be established between the transmitter and the receiver to maximise the SNR.

3. No useful information is lost during the decimation process to reduce the sampling rate to the symbol rate.

In practice, these ideal conditions might not be satisfied because the ideal lowpass filter (i.e., the brickwall filter) that satisfies the first condition is not realisable. Its IR is the sinc function which has infinite duration with very poor decay. As a result, its truncated version has very poor frequency localisation. Also, perfect synchronization is a formidable task, especially, in time-varying channels.

In this subsection we will show that it is possible to design a receiver which is simpler to implement. Based on the properties of the SI subspaces proved in subsections 2.3.1 and 2.3.2, we find the structure of an optimum receiver in which the low-pass filter preceding the sampler has SRRC frequency characteristics. Then we represent the channel as a tapped delay line filter. The tap delays are characterized by the characteristics of the physical channel.

In order to obtain a generic channel model and receiver structure we assume that the channel is unknown, but the complex envelope of the received signal has the general form of (2.14), in which, the number of paths, I, per path linear distortions, $h_\kappa(t)$, delays, τ_κ, and Doppler dilations, ν_κ, are arbitrary. Also, we assume a quasi-stationary channel, that is, $a_\kappa(t) = a_\kappa$ for the time interval of interest.

Theorem 2.3.2 provides information about the *receive signal space* or *the range space* of the channel. With appropriate choice of r, according to Theorem 2.3.2, all received signals belong to $S_{\frac{T_\circ}{r}}(D_r p(t))$, which has the orthonormal basis (ONB) $\{\sqrt{r}p(rt - kT_\circ) : k \in \mathbb{Z}\}$, by Theorem 2.3.1 (part 1). Consequently, the received signal corrupted by additive noise $z(t)$ may be represented as

$$r'_{\mathrm{b}}(t) = \sum_{k\in\mathbb{Z}} c_k \sqrt{r} p(rt - kT_\circ) + z(t), \tag{2.57}$$

where

$$c_k = \left\langle r_{\mathrm{b}}(t), \sqrt{r}p(rt - kT_\circ) \right\rangle, \tag{2.58}$$

are the expansion coefficients of the noise-free received signal $r_{\mathrm{b}}(t)$. The series in (2.57) is infinite.

The representation in (2.57) is independent of the per path distortions, delays and dilations as far as r is chosen according to Theorem 2.3.2. So, it should not be surprising that the receiver structure described below does not require perfect symbol

timing synchronisation and provides a set of sufficient statistics and when $r = r_{\min}$ the SNR is maximum.

The sufficient statistics from the received signal $r'_{\mathrm{b}}(t)$ can be extracted by projecting it onto the basis functions $\sqrt{r}p(rt - kT_\circ),\ k \in \mathbb{Z}$. This can be implemented by passing $r'_{\mathrm{b}}(t)$ through a filter with impulse response $\sqrt{r}p(rt)$ and sampling the output at rate $\frac{r}{T_\circ}$.

In NB channel model, the received signal is a linear combination of delayed and attenuated replicas of the transmitted signal. The NB channel model assumes the resolvability of the multipath channel into individual non-selectively fading paths. It was proposed and studied by Turin [146]. In Turin's model the relative delay values, $\Delta\tau_\kappa = \tau_{\kappa+1} - \tau_\kappa$, are not necessarily equal. It originates from the geometrical interpretation of the electromagnetic wave propagation in the environment.

With a different approach and a wider scope, Kailath [59] proposed another representation of the channel by using the Shannon Sampling Theorem [59]. Kailath's approach is valid for every linear filter with band-limited impulse response. This approach is usually used in the mathematical derivation of a discrete channel model [102, 153].

Both models have drawbacks and advantages. The assumption of uncorrelated scattering (US) is valid for Turin's model [9, 59] by modelling assumption and measurement supports, but it is not valid for Kailath's model [59, 136, 66]. On the other hand Turin's model assumes resolvability of individual *frequency non-selective* paths which is not a valid assumption in many communication channels such as UWB channels. In UWB communication, channel distortion of the pulses received from each path is a major problem that differentiates them from other channels [85, 10, 159, 104, 103]. As a result, the receiver designed based on Turin's model can not compensate for the pulse distortions caused by the channel if they exist. An important and widely used model based on the Turin's formulation is the Saleh-Valenzuela model for indoor wireless communication channels [115].

Different aspects of Turin's and Kailath's models can be summarised as follows:

Turin's Model:[146]

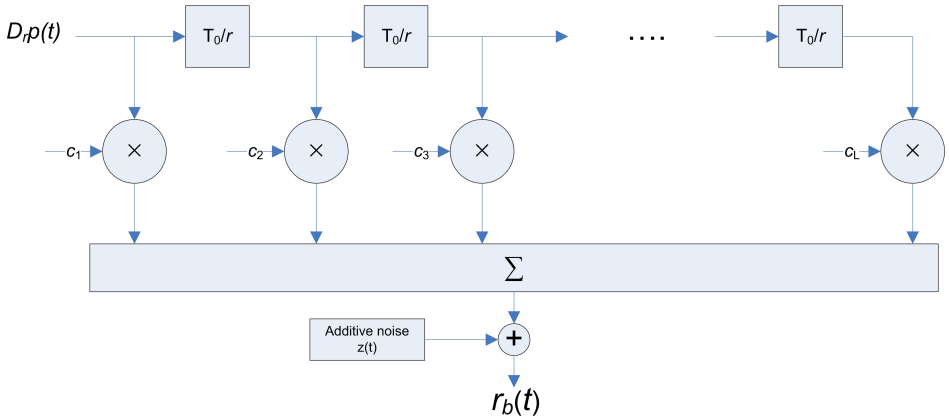

Figure 2.3: The truncated FS TDL model for the channel: The transmitted pulse, $p(t)$, is the SRRC function, but the TDL model's input is $D_r p(t)$, where r is characterized by Theorem 2.3.1. Since the channel is linear, this figure describes the response of the channel to any linearly modulated signal with pulse shape $p(t)$. The tap coefficients, c_k's, characterise the channel.

1. Pulse distortions are not taken into account, so this model is not valid for UWB channels. The receiver designed based on this model can not compensate for per path pulse distortions,

2. The relative path delays are not necessarily equal. The receiver has to estimate per path delays.

3. For channels with dense scatterers the uncorrelated scattering assumption is valid for this model.

Kailath's Model:[59]

1. Mathematical derivation of Kailath's model is based on special properties of the sinc function [59]. In practice, the signal $\mathrm{sinc}\,(t)$ can not be generated as it has infinite duration. Truncation of $\mathrm{sinc}\,(t)$ results in significant spectral side-lobes which is not a desirable property.

2. The US property, which is usually assumed for wireless channels, is not valid for Kailath's model. In other words, the channel tap weights can be correlated [59, 136, 66].

Both channel models can be described by a tapped delay line (TDL) filter model [146, 59]. The tap weights $\{c_k\}$, defined by (2.58), are different from the TDL model for NB channel models at least in two ways:

1. In the TDL model of NB channels the Doppler effect is modelled as constant frequency shifts across the whole bandwidth [56, 39], but in (2.11) the Doppler effect is modelled as dilation operators. There has been some effort to model the Doppler effect by dilations instead of modulations [27, 58, 111, 157, 69, 124, 163, 165, 168, 170, 169, 144]. Wavelets' success in many areas of science and engineering has been the major motive to look for modulation and/or reception techniques based on time-scale analysis instead of time-frequency analysis. While the theory of wavelets and their multiresolution capability is used in our results, our approach is completely different from all other works cited above. We are not using wavelets and their properties. We use the scaling function of wavelets (father wavelets) and the SI subspaces generated by them. We proved new invariance properties for the SI subspaces generated by the scaling function to characterise the *range signal space* for an arbitrary linear modulation and a given pulse shape. The pulse shape in our case is the famous SRRC pulse. The SRRC pulse can be replaced by other pulses with even better time decay.

2. Uncorrelated scattering (US) assumption of NB model is not valid for the new model. Since usually $r > 1$, it is possible for two adjacent coefficients to have contributions from one single received pulse. This implies that the (cross-)correlations of the coefficients needs to be studied.[6]

Based on the TDL model of Fig. 2.3, we now design a RAKE demodulator. We assume that the channel coefficients $\{c_k\}$ are known and there is no ISI. Modulation can be any linear modulation scheme with arbitrary constellation points. If the transmitted signal symbol is d_{n_0}, then the noise-free received signal $r_{\mathrm{b}}(t) \in S_{T_\circ}\left(\sqrt{r}p(rt)\right)$, and therefore, it has a unique representation in terms of the orthonormal basis $\{\sqrt{r}p(rt - kT_\circ) : k \in \mathbb{Z}\}$:

$$r_{\mathrm{b}}(t) = \sum_{k\in\mathbb{Z}} \mathrm{d}_{n_0} c_k \sqrt{r}p(rt - kT_\circ). \tag{2.59}$$

The receiver has no information about the transmitted symbol. Therefore, to extract the decision variables we correlate the noisy received signal with the basic signals

[6]Essentially, the US assumption is not valid in any band-limited channel model. It is valid if multipath components can be resolved and separated at the receiver. The difference is that in the model of Fig. 2.3 the correlation of tap weights are more than the symbol spaced one.

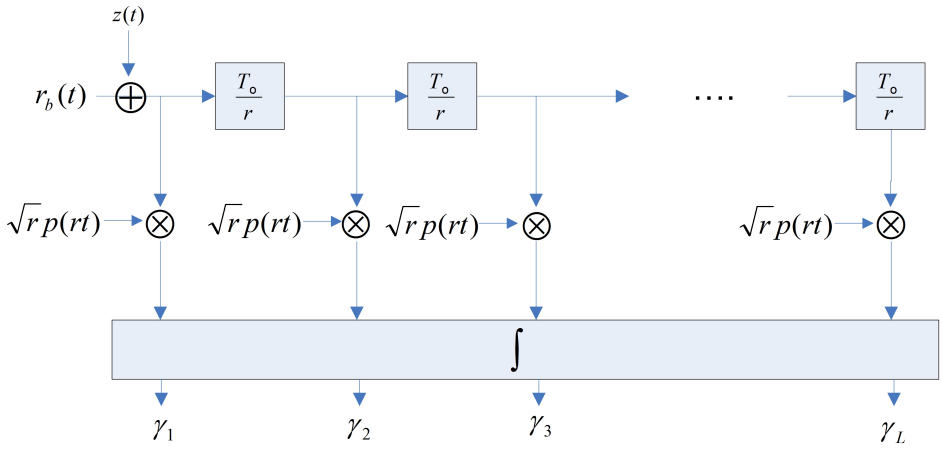

Figure 2.4: RAKE demodulator

$\sqrt{r}p(rt - kT_\circ)$ to obtain

$$\gamma_k = \langle r_\mathrm{b}(t) + z(t), \sqrt{r}p(rt - kT_\circ)\rangle \tag{2.60}$$

$$= \int r_\mathrm{b}(t)\sqrt{r}p(rt - kT_\circ)\,\mathrm{d}t + \int z(t)\sqrt{r}p(rt - kT_\circ)\,\mathrm{d}t \tag{2.61}$$

$$= r_k + z_k \ (k \in \mathbb{Z}). \tag{2.62}$$

Then the maximum likelihood receiver output is

$$\mathrm{d}_{n_0} = \underset{\mathrm{d}_n}{\operatorname{argmin}} \sum_{k\in\mathbb{Z}} |\mathrm{d}_n c_k - \gamma_k|^2 . \tag{2.63}$$

The RAKE demodulator structure with L fingers is shown in Fig. 2.4.

Remark. Since the basis is orthonormal (ONB), for additive white Gaussian noise (AWGN) $z(t)$ with zero mean and power spectral density $2N_0$, z_k $(k \in \mathbb{Z})$ are iid Gaussian random variables: $z_k \sim \mathcal{N}(0, 2N_0)$.

2.5 Conclusion

In this Chapter, we derived a mathematical expression for the lowpass received signal from a wireless channel which includes the frequency dependent effects of the channel. In this model, per pulse distortions due to antennas and propagation effects are modelled as filters for individual paths and the Doppler effect is modelled as a combination of the carrier frequency shift and the envelope dilation. Using this expression,

we determined the characteristics of a front-end receiver C/D converter including a realisable lowpass filter, and the lowest sampling rate with the property that its output provides a sufficient statistic for any optimum receiver. A DT TDL channel model with tap spacing equal to a fraction of the symbol interval is derived. The theory of SI subspaces are used to derive the DT channel model.

Chapter 3

Lossy Dielectric Wall Effects and UWB Channel Models

Synopsis Broadband (BB) wireless communication channels cause pulse distortion and result in many multipath components arriving at the receiver in clusters. As a case study of the pulse-distorting effects of a physical channel, we analyse the effects of lossy dielectric walls on BB pulses by using frequency domain methods. The frequency-dependent parameters of commonly used building materials are used to analyse the effects of multiple reflections and transmissions, material distortion, and interpulse interference on BB pulse waveforms. The possibility of polarization-dependent distortion is discussed. Various thicknesses of walls and angles of incidence are considered. The distortion due to each effect is quantified in terms of maximum correlation coefficients (MCCs). The overall effect of the wall is modelled as a tapped delay-line (TDL) filter based on the MCC. By using our model derivation approach, it is shown that the power-delay profiles (PDPs) of multilayer walls have multicluster structures and their first ray can be weaker than the second one; a phenomenon similar to the soft-onset phenomenon observed in measurements but is smaller scale. This chapter proposes a theoretical approach, by using the laws of classical electromagnetics, to derive TDL models for indoor channels. The theoretical approach can be used to complement and validate the experimental channel modelling approaches.

3.1 Introduction

In most NB communication systems, the message carrying pulses have an absolute bandwidth of less than 20 MHz and fractional bandwidth of less than 0.02. In UWB

systems, the pulses have absolute bandwidth of more than 500 MHz and/or fractional bandwidth of more than 0.2 [31]. In broadband mm-wave communication systems based on the standard IEEE 802.11ad [1], using the single carrier physical layer (SC-PHY), the transmitted pulse bandwidth can exceed 2 GHz. As a result of these differences in absolute and/or fractional bandwidths, the channel responses to NB, UWB and BB mm-wave pulses are different [23, 85].

The differences in channel response to information carrying pulses can stem from these factors: 1) the relative geometrical scale of the electromagnetic pulses in the air (i.e. pulse length) and the objects in the communication environment; and 2) the frequency-dependent electrical properties of the material of the interacting objects.

In this chapter, we focus on the interactions of UWB pulses with walls. We will show that some phenomena observed in UWB propagation such as the clustered distribution of arrival times of pulses [88] and the power-delay profile (PDP) of each cluster [88, 83, 49] are related to the effects of walls [90].

Walls are abundant in indoor and urban communication environments. The dimensions of walls in these environments are usually large compared to the pulse length. Electromagnetic waves can reflect off or transmit through a wall with sufficiently large dimensions. When the dimensions of the wall are comparable or smaller than the wavelength, diffraction occurs which is a different phenomena. In fact, reflection from and transmission through walls are the dominant propagation mechanisms in indoor environments [112].

Three of the key differences between the interactions of NB and BB pulses with lossy dielectric walls are:

1. The time-harmonic approximations of time-limited pulses, as used in modelling NB systems and receiver design [102], do not adequately characterize the UWB channel [26, 86, 23]. Each pulse experiences amplitude and phase distortion.

2. Lossy dielectric walls illuminated by a BB pulse, reflect/transmit several separate or partially-overlapped UWB pulses.

3. Due to polarization-dependent surface reflection and transmission [5], the transmission and reflection responses of lossy dielectric walls for parallel and perpendic-

ular polarizations are different and may cause polarization-dependent distortion (PDD).

Waveform distortion is a degrading factor in UWB systems [137, 104, 103, 85]. The theoretical study of pulse distortion due to some special diffracting geometrical objects was considered in [104] and [103]. Time domain methods for wall reflections and transmission were considered in [7] and [138]. There, the material parameters are assumed to be constant across the UWB frequency range and the available solutions are based on simplifying assumptions that are not valid for most building materials. Therefore, these methods do not provide practical information about pulse distortion. Many experimental results for electromagnetic (EM) parameters of commonly used building materials over a wide frequency range show the frequency dependency of the material parameters. We refer readers to [32] and [112] for a review of some measurement results. The available information on frequency-dependent material parameters facilitates theoretical and simulated study of physical effects in the frequency domain. The analysis of the effects of walls on UWB pulses in this chapter is based on permittivity and conductivity functions of commonly used building materials given in [28].

Here we focus on the pulse distortion and delay dispersion of UWB signals due to reflection from and transmission through a lossy dielectric wall and its correspondence with standardized channel models for UWB systems [88]. We use frequency-domain methods. We consider the aspects of pulse responses that influence UWB channel modelling. The significance of the distortions due to lossy dielectric walls of different building materials are compared. The pulses created by multiple internal reflections of wall surfaces are considered. The maximum correlation coefficient (MCC) [13, 60, 64] is used as a measure of the distortion of individual pulses compared to the incident pulse. MCC is a measure of the maximum energy that can be captured from each received pulse when the transmitted pulse shape is used for matched filtering.

Our contributions in this chapter can be summarised as: 1) including realistic frequency dependence of the parameters of materials in indoor environments over an ultra-wide frequency range; 2) developing the MCC as a measure of the degree of distortion caused by surface reflections/transmissions and internal material distortion for multiple reflections and transmissions; 3) inclusion of per-path pulse distortions,

multiple internal reflections caused by lossy dielectric walls and derivation of PDPs for reflections from and transmissions through walls, 4) theoretical explanation of the standardized experimental PDP of UWB channels.

The results are based on the information provided by ITU's recommendation [96] about the frequency-dependent permittivity and conductivity of some commonly used building materials. The information provided in [96] is valid over certain frequency ranges specified in Table 3.1. In the graphs and simulation results presented in this chapter, we have focused on frequency ranges that are pertinent to UWB communication systems complying with the standard IEEE 802.15.4-2011 [2][1]. A similar approach can be used to analyse the pulse distortion phenomena and derive TDL models for responses of single or multilayer wall structures over the frequency ranges pertinent to mm-wave communication systems [109], in particular, those compliant with the standard IEEE 802.11ad.

The method used in this chapter for analysing the effects of multilayer building structures on UWB pulses is new. Multilayer structure effects on harmonic waves in optical frequency range are usually studied in the physical optics literature. The book [18] is an excellent general reference and the classic book [50] is devoted to optical properties of thin solid films and their applications in coating.

3.2 UWB Pulses

UWB systems can be designed to be either baseband (carrierless) or bandpass (carrier-based) [86]. We consider a bandpass communication system so that the dependence of the distortion on a particular frequency band can be studied. The PDPs for wall reflections and transmissions obtained in Section 3.7 are valid for both baseband and bandpass transmissions.

We use pulses with square-root raised cosine spectral characteristics for amplitude shaping bandpass systems. These will be referred to as SRRC pulses. SRRC pulses cannot be used for baseband transmission as they have a significant DC component. For baseband transmission the fourth or higher order Gaussian derivatives can be used.

[1]This standard has been superseded by the standard IEEE 802.15.4-2015 [3].

Lower order pulses do not comply with UWB pulse emission regulations [54, 26]. For the second order Gaussian pulse this is shown in Fig. 3.1.

A SRRC pulse with Nyquist bandwidth $R_{\mathrm{s}} > 0$ and spectral roll-off factor α, $0 \leq \alpha \leq 1$, is defined by

$$p_{\mathrm{sr}}(t) = C_{\mathrm{s}} \frac{\sin\left((1-\alpha)\pi t R_{\mathrm{s}}\right) + 4\alpha t R_{\mathrm{s}} \cos\left((1+\alpha)\pi t R_{\mathrm{s}}\right)}{\pi t R_{\mathrm{s}} \left(1 - (4\alpha t R_{\mathrm{s}})^2\right)}, \tag{3.1}$$

for $t \neq 0, \pm 1/(4\alpha R_{\mathrm{s}})$, and elsewhere by continuity. When $C_{\mathrm{s}} = \sqrt{R_{\mathrm{s}}}$ the pulse $p_{\mathrm{sr}}(t)$ is normalized: $\int_{\mathbb{R}} |p_{\mathrm{sr}}(t)|^2 \, \mathrm{d}t = 1$, for any choice of α and R_{s}. The parameters R_{s} and α in (3.1) control the time and frequency concentration of the pulse. The time domain graph of this pulse and its energy spectral density (ESD) are plotted in Fig. 3.1. With appropriate choices of the parameters, the SRRC function easily satisfies the UWB spectral emission mask for indoor communications [31]. The second order Gaussian derivative pulse in the time domain and its energy spectral density are plotted for comparison.

According to UWB PHY of the standard IEEE 802.15.4-2011 [2], the pulse shape requirement for UWB communications is determined by the similarity of the pulse to a SRRC pulse with a rolloff factor of $\alpha = 0.5$. The similarity is measured by cross correlation. The normalised cross correlation between a given pulse $p(t)$ and $p_{\mathrm{sr}}(t)$ is defined by

$$\phi(\tau) = \frac{1}{\|p_{\mathrm{sr}}(t)\| \|p(t)\|} \operatorname{Re} \int_{-\infty}^{\infty} p_{\mathrm{sr}}(t) \overline{p(t+\tau)} \, \mathrm{d}t, \tag{3.2}$$

where Re denotes the real part. In order for a UWB PHY transmitter to be compliant with this standard, the transmitted pulse $p(t)$ must have a magnitude of the cross-correlation function $|\phi(\tau)|$ whose main lobe is greater than or equal to 0.8 for a duration of at least a fraction of a nanosecond depending on the channel numbers defined in [2, Table 108], and any sidelobe must be no greater than 0.3.

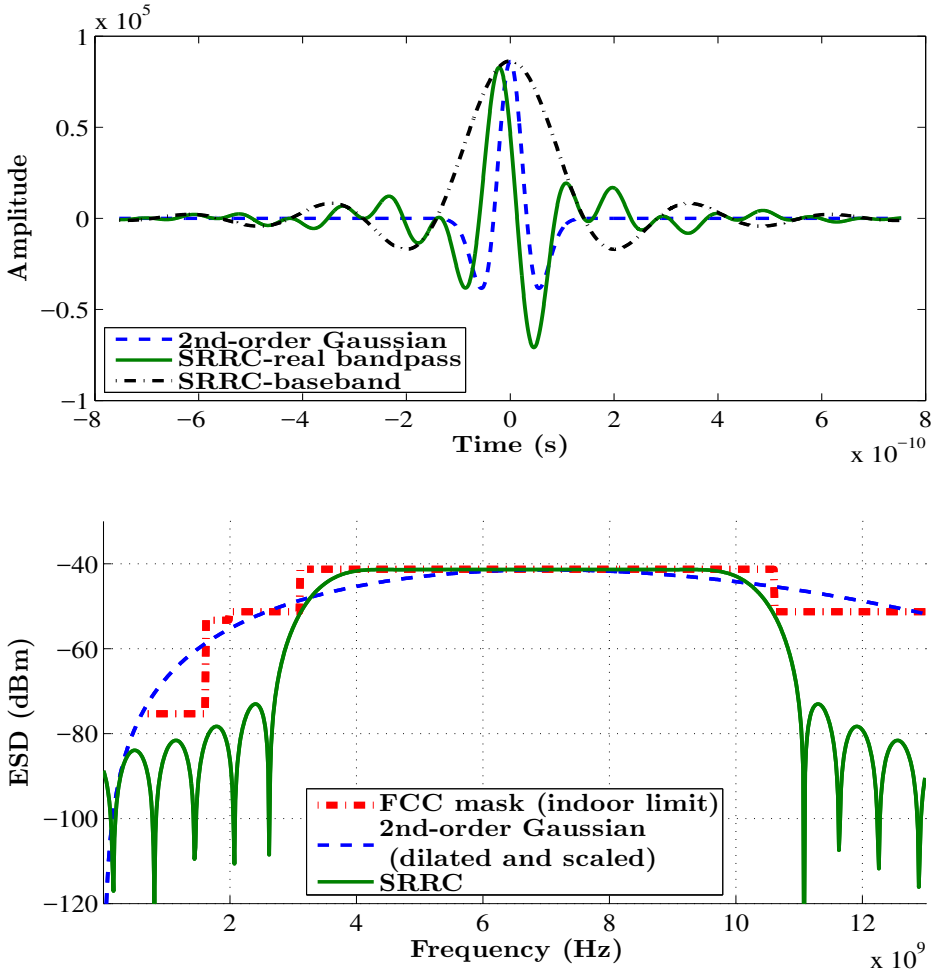

Figure 3.1: Comparison of the second order Gaussian derivative and the SRRC pulse with $\alpha = 0.22$ and $R_s = 6.6393 \times 10^9$ (Top: time domain pulses; bottom: energy spectral densities).

3.3 Millimetre Wave Pulses

In the standard IEEE 802.11ad, the transmit pulse shape has not been specified. It is up to the implementer to design a pulse shape that satisfies the relevant spectral mask requirements. This standard specification defines the receiver filter for error vector magnitude (EVM) measurement as a SRRC filter with a roll-off factor of 0.25. As we mentioned in Section 3.2 and as shown in Fig. 3.1 for the SRRC pulse, Nyquist pulses can be designed that use the available spectrum efficiently and can use the available degrees of freedom in joint time and frequency domains. Ideally, prolate spheroidal wave functions can be used to exploit all the time-frequency degrees of freedom [65]. But these functions are not suitable for serial transmission of data symbols as in PAM and QAM systems because, they do not satisfy Nyquist's ISI criterion and they are not generated by time shifts of a single generator in a way similar to SRRC pulses. For pulse

shaping for these systems, the SRRC family of functions provide a satisfactory balance between the complexity of implementation and joint time-frequency concentration. Also, they have the Nyquist's zero-crossing property.

3.4 Maximum Correlation Coefficient

Most communication systems and pulse radars use time-limited pulses [102, 137]. In these systems the optimum receiver consists of a filter matched to the pulse response of the channel [102]. Usually, the pulse response of the channel is not known a priori. In this case, modern digital receivers usually use a front end filter that is matched to the transmitted pulse. Then the output of this filter is sampled, periodically, at a rate that is usually higher than the Nyquist rate [102]. The Nyquist rate for the pulse (3.1) is $(1+\alpha)R_s$. The samples can be used for channel estimation, equalization and data detection [40, 102]. The combination of filtering and sampling is equivalent to correlating the received signal with delayed versions of the transmitted pulse and hence the correlation of the received pulse with the transmitted pulse is fundamental in channel modelling, receiver design and system performance evaluations. We therefore use the MCC (defined below) to quantify pulse waveform deformation and any measured loss due to pulse waveform deformation can be incorporated into the overall path-loss in the PDP.

The (deterministic) correlation function of two nonzero, finite-energy signals $x(t)$ and $y(t)$ is defined by

$$C(\tau) = \frac{1}{\|x\|\|y\|} \int_{\mathbb{R}} x(t-\tau)\overline{y(t)}\,\mathrm{d}t, \tag{3.3}$$

and the MCC by $m_c(x,y) = \max_{\tau\in\mathbb{R}} |C(\tau)|$. Obviously, for $y(t) = x(t)$ the MCC is equal to 1, and is achieved at $\tau = 0$. By the Cauchy-Schwartz inequality, $0 \leq m_c(x,y) \leq 1$. Note that since the function $I(\tau) \triangleq \int_{\mathbb{R}} x(t-\tau)\overline{y(t)}\,\mathrm{d}t$ is bounded and continuous, in (3.3) the maximum is attained at some extreme point τ_m which is not necessarily unique.

The MCC, also known as the Bhattacharyya coefficient [13] and fidelity [64], is a general formula for comparison of two signals, vectors, or probability distribution

functions (PDFs) in an inner product space [113, 60, 72].

For two square-integrable complex-valued signals $x(t)$ and $y(t)$, Plancherel's theorem [113, p. 188] states that

$$\int_{\mathbb{R}} x(t)\overline{y(t)}\,\mathrm{d}t = \int_{\mathbb{R}} X(f)\overline{Y(f)}\,\mathrm{d}f. \tag{3.4}$$

In particular, by letting $x(t) = y(t)$ in (3.4), we have $\|x\|^2 = \|X\|^2$, which is the Parseval identity. By using (3.4) and the shift property of the Fourier transform, (3.3) can be expressed as

$$C(\tau) = \frac{1}{\|X\|\|Y\|}\int_{\mathbb{R}} X(f)\overline{Y(f)}\mathrm{e}^{-\mathrm{j}2\pi f\tau}\,\mathrm{d}f. \tag{3.5}$$

When $Y(f) = H(f)X(f)$, for some transfer function $H(f)$, (3.5) simplifies to

$$C(\tau) = \frac{1}{\|X\|\|HX\|}\int_{\mathbb{R}} |X(f)|^2\overline{H(f)}\mathrm{e}^{-\mathrm{j}2\pi f\tau}\,\mathrm{d}f, \tag{3.6}$$

which is more appropriate for numerical calculation as it does not require calculating the inverse Fourier transform of $H(f)$ and $H(f)X(f)$. The limits of integration in (3.6) depend on the frequency spectrum of the signal $x(t)$.

3.5 Reflection and Transmission Responses of Lossy Dielectric walls

In the rest of this chapter, a slab or a wall refers to a lossy dielectric wall, roof, ceiling, partitioning or similar structure in an indoor environment. The slab's width is arbitrary, but its length and height are assumed large compared to the wavelengths of interest. We assume its material to be linear, homogeneous and isotropic, and non-magnetic [5]. Its conductivity and relative permittivity are frequency dependent and given by the functions $\sigma(f)$ and $\varepsilon_{rr}(f)$. The parallel planar surfaces of the slab are denoted by S_1 and S_2 and its thickness is l meters (Fig. 3.2).

We consider a Cartesian coordinate system such that the origin, the point O in Fig. 3.2, is located on the plane S_1 and the z axis is normal to S_1 (and S_2). The totality of the slab is in the right half-space characterized by $z \geq 0$.

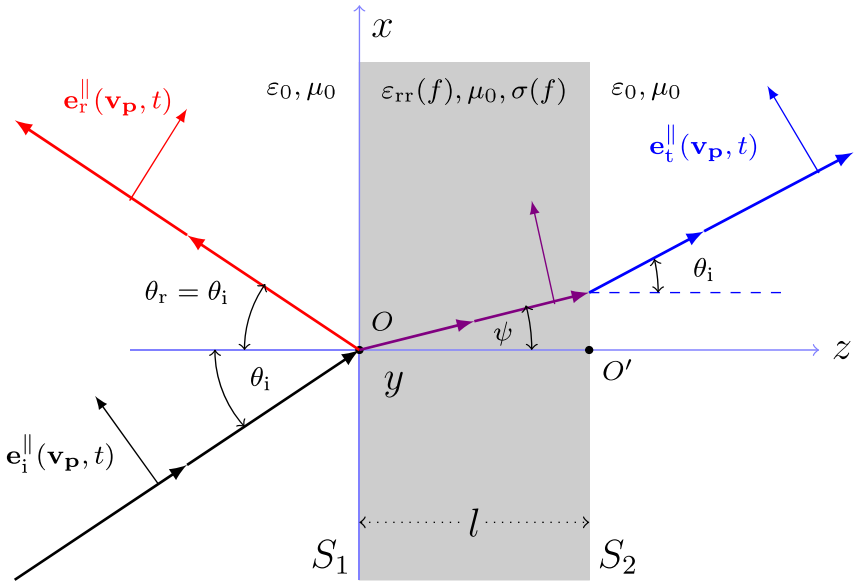

Figure 3.2: The geometry of reflection from and transmission through a lossy dielectric slab for parallel polarization.

A planar EM pulse with a linear transversal electric field (E-field) polarization is incident on interface S_1 with an angle of incidence θ_i. The time domain waveform of the pulse is given by $p(t) = p_{sr}(t)\exp(j2\pi f_c t)$, where f_c is the carrier frequency. By using the Fourier transform, the E-field of the incident pulse can be represented as a superposition of weighted time-harmonic components. To fix the time origin, we assume that all harmonic components have phase zero at the space origin O. Then at an arbitrary point $\mathbf{v_P}$ in the left half-space $z \leq 0$, the E-field of the incident pulse is represented as

$$\mathbf{e}(\mathbf{v_p}, t) = \frac{1}{2\pi}\hat{\mathbf{e}} \int_{\mathbb{R}} P(\omega) e^{j\omega t} e^{-j\beta_0(\omega)\hat{\mathbf{r}}\cdot\mathbf{v_P}}\, d\omega, \tag{3.7}$$

where

- $\hat{\mathbf{r}}$ is the direction of propagation,
- $\hat{\mathbf{e}}$ is the direction of polarization; assumed to be the same for all harmonics,
- $P(\omega) = \int_{\mathbb{R}} p(t) e^{-j\omega t}\, dt$, and
- $\beta_0(\omega) = \omega\sqrt{\mu_0\varepsilon_0}$ is the free-space wave number.

For oblique incidences, the phases of harmonic components are different at different points on S_1. Choosing the time and space origins is necessary to obtain correct space-time equations for the distorted pulses and their relative delays. With reference to the

geometry of Fig. 3.2, the perpendicular and parallel components of the overall reflected and transmitted pulse responses are given by

$$\mathbf{e}_{\mathrm{r}}^{\perp}(\mathbf{v_p},t) = \frac{1}{2\pi}(\hat{\mathbf{e}}.\mathbf{j})\mathbf{j}\int_{\mathbb{R}} R^{\perp}(\omega)P(\omega)\mathrm{e}^{-\mathrm{j}\,\beta_0(\omega)\,\hat{\mathbf{r}}\cdot\mathbf{v_P}}\mathrm{e}^{\mathrm{j}\omega t}\,\mathrm{d}\omega, \tag{3.8a}$$

$$\mathbf{e}_{\mathrm{r}}^{\parallel}(\mathbf{v_p},t) = \tag{3.8b}$$
$$\frac{1}{2\pi}((\hat{\mathbf{e}}.\mathbf{i})\mathbf{i}+(\hat{\mathbf{e}}.\mathbf{k})\mathbf{k})\int_{\mathbb{R}} R^{\parallel}(\omega)P(\omega)\mathrm{e}^{-\mathrm{j}\,\beta_0(\omega)\,\hat{\mathbf{r}}\cdot\mathbf{v_P}}\mathrm{e}^{\mathrm{j}\omega t}\,\mathrm{d}\omega,$$

$$\mathbf{e}_{\mathrm{t}}^{\perp}(\mathbf{v_p},t) = \tag{3.8c}$$
$$\frac{1}{2\pi}(\hat{\mathbf{e}}.\mathbf{j})\mathbf{j}\int_{\mathbb{R}} T^{\perp}(\omega)P(\omega)\mathrm{e}^{-\mathrm{j}\,\beta_0(\omega)\,\hat{\mathbf{r}}\cdot(\mathbf{v_P}-l\mathbf{k})}\mathrm{e}^{\mathrm{j}\omega t}\,\mathrm{d}\omega,$$

$$\mathbf{e}_{\mathrm{t}}^{\parallel}(\mathbf{v_p},t) = \tag{3.8d}$$
$$\frac{1}{2\pi}((\hat{\mathbf{e}}.\mathbf{i})\mathbf{i}+(\hat{\mathbf{e}}.\mathbf{k})\mathbf{k})\int_{\mathbb{R}} T^{\parallel}(\omega)P(\omega)\mathrm{e}^{-\mathrm{j}\,\beta_0(\omega)\,\hat{\mathbf{r}}\cdot(\mathbf{v_P}-l\mathbf{k})}\mathrm{e}^{\mathrm{j}\omega t}\,\mathrm{d}\omega,$$

where the subscripts r and t refer to reflection and transmission, and $\mathbf{i}$, $\mathbf{j}$ and $\mathbf{k}$ are the standard Cartesian unit vectors in the x-, y- and z-directions. The reflection and transmission transfer functions of the slab are given by [18, 95]

$$R^{(\perp,\parallel)}(\omega) = \frac{\rho(1-\exp(-2\gamma l\cos\theta_{\mathrm{t}}))}{1-\rho^2\exp(-2\gamma l\cos\theta_{\mathrm{t}}))}, \text{ and} \tag{3.9a}$$

$$T^{(\perp,\parallel)}(\omega) = \frac{(1-\rho^2)\exp(-\gamma l\cos\theta_{\mathrm{t}}))}{1-\rho^2\exp(-2\gamma l\cos\theta_{\mathrm{t}}))}, \tag{3.9b}$$

respectively. Here, $\rho = \rho^{(\perp,\parallel)}$ is the Fresnel reflection function for perpendicular ($\perp$) or parallel ($\parallel$) polarizations when the wave is incident from the left at interface S_1. It is given by (3.13) below. $\gamma = [\mathrm{j}\omega\mu_0(\sigma+\mathrm{j}\omega\varepsilon_{rr})]^{1/2}$ is the propagation constant[2] inside the slab and θ_{t} is the complex angle of refraction inside the slab [5, 95]. In (3.8a) and (3.8b), $\mathbf{v_P}$ is any point in the $z \leq 0$ half-space and in (3.8c) and (3.8d) it is any point in the $z \geq l$ half-space.

Equations (3.8) and (3.9) describe the total responses of reflection and transmission. They include both discrete and diffuse effects as described below. Since $|\rho^2\exp(-2\gamma l\cos\theta_{\mathrm{t}}))| < 1$, for all ω, we can expand $R^{(\perp,\parallel)}(\omega)$ and $T^{(\perp,\parallel)}(\omega)$ into absolutely convergent series as $R^{(\perp,\parallel)}(\omega) = \sum_{n=0}^{\infty} R_n^{(\perp,\parallel)}(\omega)$, and $T^{(\perp,\parallel)}(\omega) = \sum_{n=0}^{\infty} T_n^{(\perp,\parallel)}(\omega)$,

[2] In the current discussion it is more appropriate to call it the propagation function to reflect its frequency dependence.

with

$$R_0^{(\perp,\parallel)}(\omega) = \rho, \tag{3.10}$$

$$R_n^{(\perp,\parallel)}(\omega) = \rho^{2n-1}(\rho^2 - 1)\exp(-2n\gamma l\cos\theta_t), \tag{3.11}$$

for $n \geq 1$, and

$$T_n^{(\perp,\parallel)}(\omega) = \rho^{2n}(1 - \rho^2)\exp(-(2n+1)\gamma l\cos\theta_t), \tag{3.12}$$

for $n \geq 0$. The formula $1/(1-z) = \sum_{n=0}^{\infty} z^n$, valid for $|z| < 1$, is used for expanding the right hand sides of (3.9). That is, the transfer functions of transmission and reflection, are composed of infinitely many elementary transfer functions, each for an individual pulse reflected from or transmitted through the slab. In the equations, $n = 0$ corresponds to the first reflected or transmitted pulse. For lossy dielectric materials, the surface reflection coefficients $\rho^{\perp,\parallel}$, the propagation constant γ and the refraction angle θ_t (and hence $\cos\theta_t$) are complex functions of ω [131, 5, 95]. Hence each individual reflected and transmitted pulse is distorted in both amplitude and phase. The significance of each distortion depends on the thickness of the slab, the direction of incidence, the frequency spectrum of the incident pulse and the parameters of the material of the slab.

By using the complex relative permittivity $\varepsilon_{cr}(f) = \varepsilon_{rr}(f) - \mathrm{j}\sigma(f)/(2\pi\varepsilon_0 f)$, the Fresnel reflection functions for perpendicular and parallel polarizations are given by [95]

$$\rho^{\perp}(f) = \frac{\cos\theta_\mathrm{i} - \sqrt{\varepsilon_{cr} - \sin^2\theta_\mathrm{i}}}{\cos\theta_\mathrm{i} + \sqrt{\varepsilon_{cr} - \sin^2\theta_\mathrm{i}}}, \text{ and} \tag{3.13a}$$

$$\rho^{\parallel}(f) = \frac{\sqrt{\varepsilon_{cr} - \sin^2\theta_\mathrm{i}} - \varepsilon_{cr}\cos\theta_\mathrm{i}}{\sqrt{\varepsilon_{cr} - \sin^2\theta_\mathrm{i}} + \varepsilon_{cr}\cos\theta_\mathrm{i}}. \tag{3.13b}$$

The frequency dependence of $\varepsilon_{rr}(f)$ and $\sigma(f)$ is usually obtained by measurement for different materials in different frequency bands. Their values for different building materials over the frequency spectrum 0.1-100 GHz were obtained in [112] and [28] by fitting the available data to empirical functions of frequency. These functions are $\varepsilon_{rr}(f) = a(10^{-9}f)^b$ and $\sigma(f) = c(10^{-9}f)^d$. The values of the parameters a, b, c and d

Table 3.1: Parameter values for real relative permittivity and conductivity of building materials (from [28])

Material	$\varepsilon_{rr}(f)$		$\sigma(f)$		frequency
	a	b	c	d	GHz
Vacuum ($\approx$ air)	1	0	0	0	0.001-100
Concrete	5.31	0	0.0326	0.8095	1-100
Brick	3.75	0	0.038	0	1-10
Wood	1.99	0	0.0047	1.0718	0.001-100
Glass	6.27	0	0.0043	1.1925	0.1-100
Chipboard	2.58	0	0.0217	0.7800	1-100
Plasterboard	2.94	0	0.0116	0.7076	1-100
Metal	1	0	10^7	0	1-100
Medium dry ground	15	-0.1	0.035	1.63	1-10

for the building materials considered in this chapter are given in Table 3.1. Due to the complicated frequency dependence of the parameters of the material ($\varepsilon_{rr}(f)$, $\sigma(f)$) (and, consequently, $\rho = \rho^{\perp,\parallel}$, γ and θ_t), the analytical study of distortions of individual pulses is an intractable problem.

3.6 Distortion Analysis

Equations (3.10)-(3.12) show that the individual reflection and transmission transfer functions for a slab include the effects of surface reflections, surface transmissions and propagation inside the material. The distortion caused by each of these effects is quantified in this section. The MCC is used as the measure of distortion.

3.6.1 Surface reflections and transmissions

For lossy dielectrics, $\rho^{\parallel}(f)$ and $\rho^{\perp}(f)$ are complex-valued functions of frequency (3.13). Therefore, reflection causes magnitude and phase distortions. The theoretical magnitude response ($|\rho^{\perp,\parallel}(f)|$) and phase response ($\Phi(\rho^{\perp,\parallel})$) of the reflection for different materials in the frequency range 1-13 GHz are plotted in Figs. 3.3 and 3.4 where the angle of incidence is assumed to be $\theta_i = 45°$. We note that, the frequency range of validity of these graphs (and all discussion in this chapter) are according to the last column of Table 3.1.

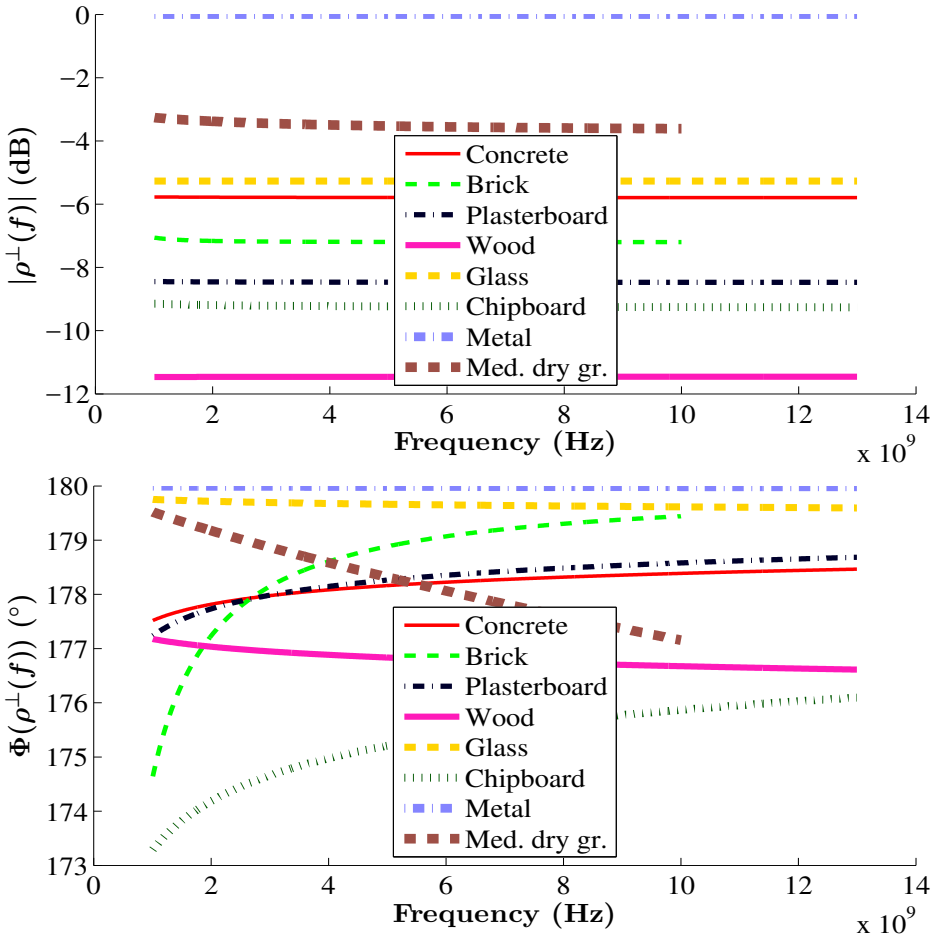

Figure 3.3: Magnitude and phase responses of Fresnel reflection coefficients: $\rho^{\perp}(f)$. The angle of incidence is $\theta_{\mathrm{i}} = 45°$.

It can be seen from Figs. 3.3 and 3.4 that, for all considered materials, the variations of the magnitude and phase responses within the frequency range 3.1-10.6 GHz are slight, and are not expected to cause appreciable pulse distortion. The distortions decrease with increasing frequency. The level of distortion, measured in terms of the MCCs of the incident pulse and the reflected pulses in three polarization directions, i.e., parallel, perpendicular and 45°-tilted direction are shown in Fig. 3.5. In this figure two angles of incidences ($\theta_{\mathrm{i}} = 30°, 60°$) are considered. The waveform changes are mainly due to phase distortions, referring to Figs. 3.3 and 3.4. In general, the waveforms of the orthogonal polarization components of the reflected pulse are different. Therefore, their combination at the output of an ideal dual-polarized antenna, which captures both polarization components without loss and superposes them, might be different from both of them. The transfer functions of reflection and transmissions for lossy dielectric slabs are due to a combination of the effects of interfaces S_1 and S_2 (multiple surface reflections and transmissions) and bulk of the material inside the

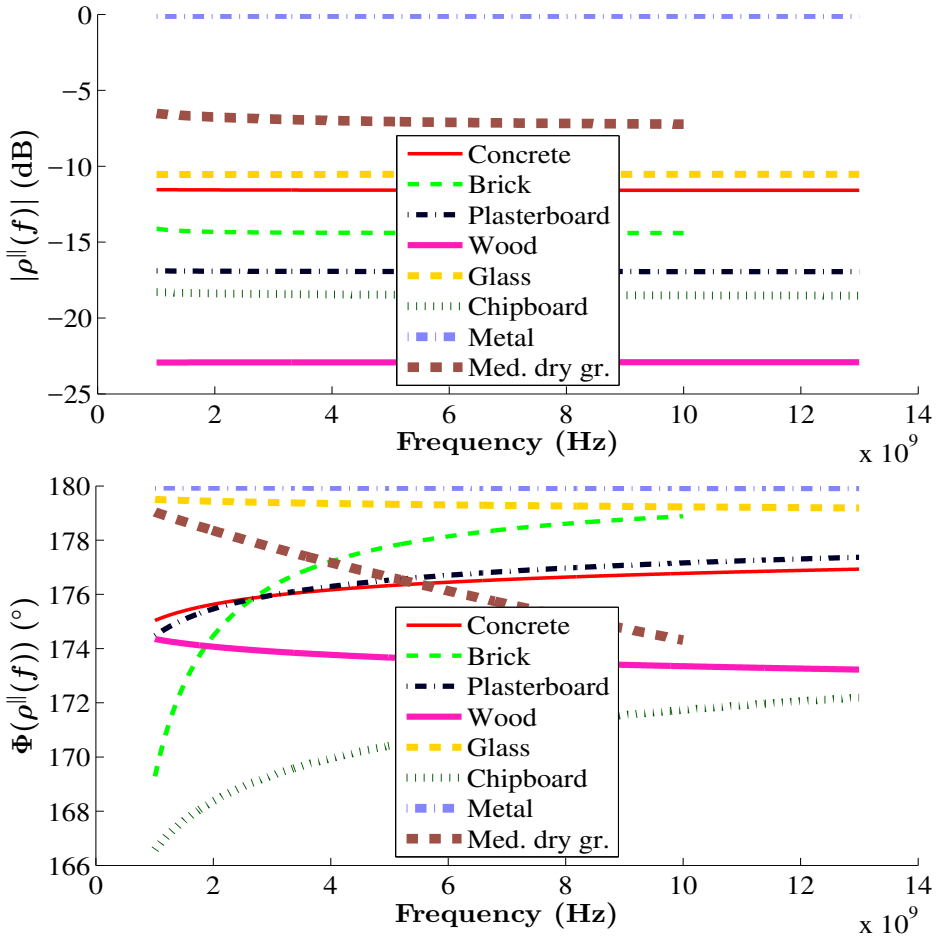

Figure 3.4: Magnitude and phase responses of Fresnel reflection coefficients: $\rho^{\parallel}(f)$. The angle of incidence is $\theta_{\mathrm{i}} = 45°$.

slab (material distortion). Since these effects are different, we quantify their effects on the nth reflected or transmitted pulse from the slab separately. The nth reflected pulse, after the first reflection, experiences two transmissions from interface S_1, in the two directions, and $2n-1$ internal reflections. We denote the transfer functions of transmissions through S_1, in opposite directions, by τ and τ', and the transfer function of the reflection from S_1, for the wave incident from the left, by ρ. We drop the superscripts $\perp$ and $\parallel$ as the discussion is valid for both polarizations. Then the overall transfer function for the surface transmissions and reflections that are experienced by the nth reflected pulse is $\tau\tau'(-\rho)^{2n-1}$. Since $\tau\tau' = 1+\rho(-\rho) = 1-\rho^2$ [5], the overall transfer function of the surface effects (excluding the effects of propagation inside the slab) is $\rho^{2n-1}(\rho^2-1)$. Similarly, for the nth transmitted pulse the transfer function of the surface effects is $\rho^{2n}(1-\rho^2)$. The resulting pulse distortion due to these surface effects were measured using the MCC formula (3.6), with $H = \rho^{2n-1}(\rho^2-1)$ for the nth reflected pulse and with $H = \rho^{2n}(1-\rho^2)$ for the nth transmitted pulse. For metal the

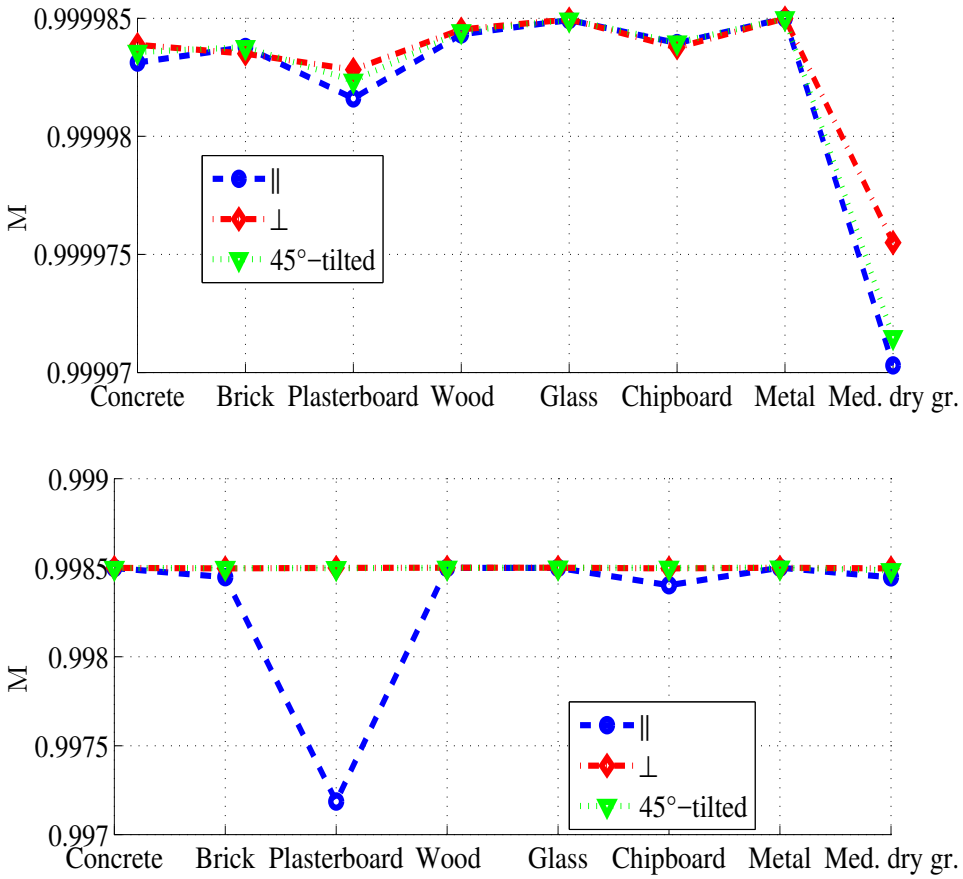

Figure 3.5: MCCs for the first reflected pulse (45° tilted with respect to the plane of incidence) and its orthogonal polarization components. Top: $\theta_i = 30°$, bottom: $\theta_i = 60°$. The dashed lines between materials are used to improve visibility and to separate the results for different polarization directions.

calculated MCCs are greater than 0.989 which corresponds to the fifth reflection $n = 4$. Noting that metal is a good conductor, it will reflect only one pulse corresponding to $n = 0$ with MCC equal to 0.99998. For other materials the MCCs are greater than 0.999 for $n \leq 4$.

To summarize, the calculations show that, as far as the pulse distortion loss is concerned, the effect of the factors $\rho^{2n-1}(\rho^2 - 1)$ and $\rho^{2n}(1 - \rho^2)$ ($\rho = \rho^{\parallel}$ or $\rho = \rho^{\perp}$) on distortion of the reflected and transmitted pulses can be ignored. These effects can cause significant magnitude loss which for a single reflection from S_1, for different materials, can be seen in Figs. 3.3 and 3.4.

3.6.2 Propagation in lossy dielectric medium

The distortion due to propagation inside the material is represented by the factor $\exp(-2n\gamma l \cos\theta_t)$ in the reflection and transmission transfer functions (3.11) and (3.12).

This seemingly simple expression includes several frequency-dependent effects (refraction angles, phase velocity and magnitude loss) that are described and quantified below.

The E-field of a time-harmonic EM wave with radian frequency ω inside the slab satisfies the Helmholtz equation [5]

$$\nabla^2 \mathbf{E}(\mathbf{v}_\mathrm{p}, \omega) - \gamma^2 \mathbf{E}(\mathbf{v}_\mathrm{p}, \omega) = 0, \tag{3.14}$$

where γ is the complex propagation constant. In (3.14), for a fixed ω, the E-field vector $\mathbf{E}$ is a function of space and time. The harmonic dependence on time is not shown in (3.14). The simplest nontrivial solution of (3.14), which is of interest to us, is given by [5]

$$\mathbf{E}(\mathbf{v}_\mathrm{p}, \omega) = E_0 \mathrm{e}^{-\gamma(\omega)\hat{\mathbf{r}}\cdot\mathbf{v}_\mathbf{P}} \hat{\mathbf{e}}, \tag{3.15}$$

where $\mathbf{v}_\mathrm{p}$ is the position vector of a point in space, $\hat{\mathbf{r}}$ is the direction of propagation and $\hat{\mathbf{e}}$ denotes the polarization direction.

In Fig. 3.2, the wave is incident upon interface S_1 at the angle θ_i and the refracted wave inside the material is travelling in the direction $\hat{\mathbf{r}} = \sin(\psi(f))\mathbf{i} + \cos(\psi(f))\mathbf{k}$, where the real refraction angle $\psi(f)$ is given by [131, p. 502] (or [5, p. 203])

$$\psi(f) = \tan^{-1}\left(\frac{2\pi f\sqrt{\varepsilon_0\mu_0}\sin\theta_\mathrm{i}}{\mathrm{Im}(\gamma\cos\theta_\mathrm{t})}\right), \tag{3.16}$$

The real refraction angle describes the direction of propagation of planes of constant phase (phase fronts) which is normal to these planes [5]. A time-limited pulse consists of harmonic waves with a continuum of frequencies. Each harmonic wave has a different propagation direction after refraction. Therefore, the ray tracing method of geometric optics cannot be used to describe the propagation of pulses in dispersive media. We assume the wall is in the far field of the wave source and, as a consequence, all harmonic components of the pulse incident upon the wall are planar with a common propagation direction. The common propagation direction is described by the plane of incidence (the xz-plane) and the angle of incidence θ_i. After refraction, the propagation directions of harmonics inside the wall are not the same. The dependence of the real refraction angle on the frequency is shown, schematically, in Fig. 3.6 where two rays corresponding to two harmonics with frequencies $f_1 \neq f_2$ are shown. This figure shows how two

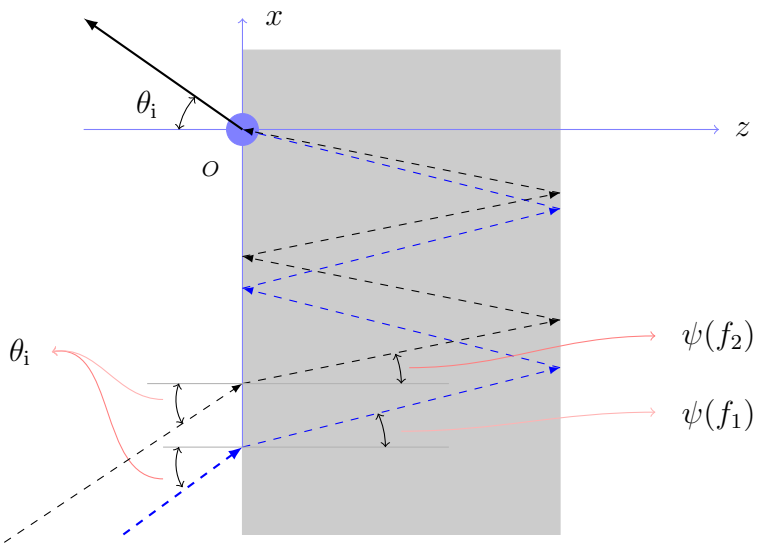

Figure 3.6: The ray model for two harmonics with frequencies $f_1 \neq f_2$, contributing to the formation of the third reflected pulse emerging at point O. The real refraction angles are different: $\psi(f_1) \neq \psi(f_2)$.

harmonics with different frequencies contribute to the formation of the third reflected pulse from the wall.

In order to find the phase of emerging harmonics at a single point, we need to choose a single direction and find the propagation in that direction for all harmonics. In the derivation of the transfer functions of reflection and transmission by slabs (3.9), obtained by solving Maxwell's equations with boundary conditions [18, 95, 50], this direction is chosen to be the transversal direction (or, the direction of the z-axis in Fig. 3.2). Therefore, for example, the expression $\exp(-(2n+1)\gamma l \cos\theta_t)$ for the nth transmitted pulse gives the phases and amplitudes of all harmonic components at point O', at the left of interface S_2, when the time and space origin for all harmonics is point O. The E-field's transversal component (i.e., in the direction of $\mathbf{k}$) is obtained by letting $\mathbf{v_P} = z\mathbf{k}$ and $\hat{\mathbf{r}} = \sin\theta_\mathrm{t}\mathbf{i} + \cos\theta_\mathrm{t}\mathbf{k}$ in (3.15) as

$$\mathbf{E}(z\mathbf{k},\omega) = E_0 \mathrm{e}^{-zp}\mathrm{e}^{-\mathrm{j}\,zq}\hat{\mathbf{e}}, \tag{3.17}$$

where $p + \mathrm{j}\,q = \gamma\cos\theta_\mathrm{t}$, p, q are real-valued functions of the frequency, and θ_t is the complex refraction angle [95]. The instantaneous E-field of (3.17), travelling in the z-direction, can be obtained by multiplying (3.17) with $\mathrm{e}^{\mathrm{j}\omega t}$ and finding its real part as

$$\mathrm{Re}\{\mathbf{E}((z\mathbf{k},\omega))\mathrm{e}^{\mathrm{j}\omega t}\} = E_0\mathrm{e}^{-zp}\cos(\omega t - zq)\hat{\mathbf{e}}. \tag{3.18}$$

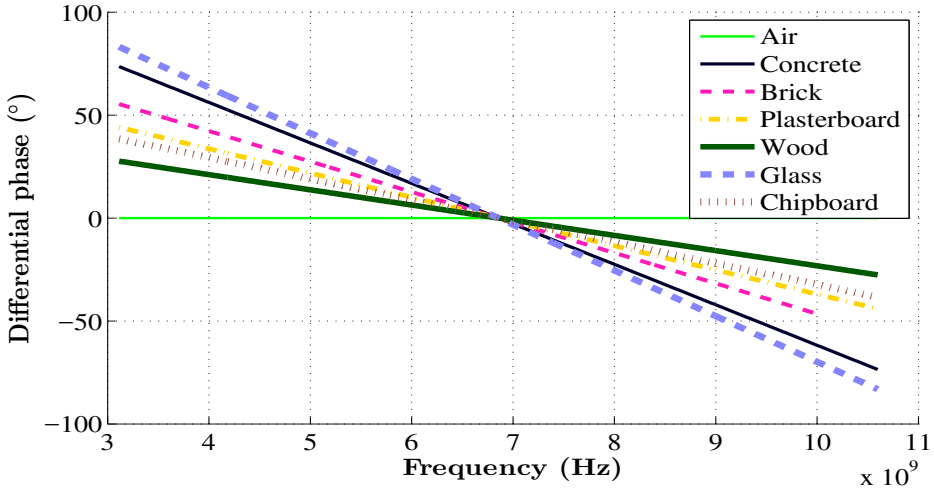

Figure 3.7: Estimates of differential phases of harmonic components with respect to the carrier wave with frequency $f_c = 6.85$ GHz after travelling 1 cm in different media; $\theta_i = 60°$.

The velocity of the wave in a lossy medium in the z-axis direction can be obtained from (3.18) by letting $\omega t - zq = \text{constant}$, and finding dz/dt as

$$u_z(\omega) = \frac{dz}{dt} = \frac{\omega}{q}. \tag{3.19}$$

Also, (3.18) shows that the amplitude is decaying in the z-direction with exponential rate $\exp(-zp)$.

Phase distortion

The frequency-dependent phase velocity in lossy media causes phase distortion. At the point where a pulse exits the slab, for example the point O in Fig. 3.2 for reflected pulses and the point O' for transmitted pulses, each harmonic has a different phase that depends on the distance it has travelled inside the material and the angle of incidence. The phase velocity is usually given in the direction of the propagation of the planes of constant phase [131, 5]. As discussed earlier, we need the component of the velocity vector in the transversal direction, i.e. the direction of the z-axis, which is given by (3.19). The frequency-dependent transversal velocities result in nonzero differential phases for harmonics after travelling equal distances. Assuming that all harmonics have zero initial phases, their phases after travelling l meters inside a material in the

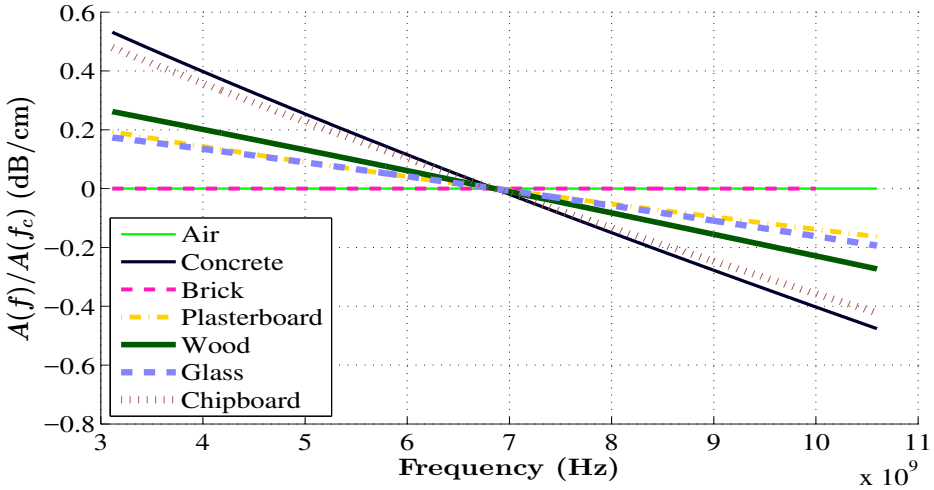

Figure 3.8: Magnitude gain of harmonic components with respect to the carrier wave ($f_c = 6.85$ GHz) after travelling 1 cm in different media. For metal the computed values of $A(f_c)$ are zero.

transversal direction are given by

$$\varphi(l, f) = \arg\{\mathrm{e}^{-\mathrm{j}lq(2\pi f)}\}, \tag{3.20}$$

where arg denotes the argument (or phase) of the embraced complex number. Note that q depends on the angle of incidence, the material's characteristics and the frequency of the incident harmonic wave. The phase distortion due to lossy dielectric medium can be measured using the phase difference of the harmonics after travelling l meters in the medium. To do this, we use the centre or carrier harmonic as a reference. Then, denoting the centre frequency by f_c, the differential phase of a harmonics with frequency f with respect to the centre frequency can be computed using the following formula:

$$\text{Differential phase} = \varphi(l, f) - \varphi(l, f_c). \tag{3.21}$$

The estimation of differential phases of the harmonics after travelling 1 cm in the transversal direction inside the material with respect to the phase of the carrier wave with frequency $f_c = 6.85$ GHz are shown in Fig. 3.7.

Magnitude distortion

When the material is lossy, part of the transmitted wave's energy is dissipated inside the slab. The resulting attenuation or magnitude loss depends on frequency. There-

Table 3.2: MCC after travelling l meter in the medium

	l=0.01	l=0.1	l=0.2
Concrete	0.99955	0.95773	0.85928
Brick	1.00000	1.00000	1.00000
Plasterboard	0.99994	0.99443	0.97812
Wood	0.99987	0.98754	0.95351
Glass	0.99994	0.99403	0.20087
Chipboard	0.99964	0.96567	0.88162
Metal*	NaN	NaN	NaN
Medium dry ground	0.98055	0.57373	0.03637

* For metal the MCCs are not defined as the signal vanishes inside the medium within these distances.

fore, the pulse experiences amplitude distortion as it propagates [5]. The attenuation of harmonic components after propagating in the transversal direction can be evaluated using $A(f) = \exp(-lp)$, where l is the distance travelled by the planes of constant amplitude, which is the direction of the z-axis for all harmonics [5], and $p = \mathrm{Re}\{\gamma \cos\theta_\mathrm{t}\}$. The magnitude gain of harmonics with frequencies in the range 3.1-10.6 GHz with respect to the gain of the carrier wave with frequency $f_c = 6.85$ GHz are shown in Fig. 3.8. For metal the computed absolute gains for all frequencies are zero. Among the remaining considered materials, within this frequency range, concrete shows relatively large gain variations of up to 1.1 dB/cm. The overall result of the above effects is distortion and attenuation of the pulse travelling inside the lossy medium. The MCC of the pulse after travelling l= 0.01, 0.1 and 0.2 meter inside the medium are given in Table 3.2. MCC is a decreasing function of the distance, l, that a pulse travels inside the medium. Comparison of figures of Table 3.2 with the MCC values obtained for surface effects shows that the material distortion affects the waveform more than mere reflections from or transmissions through surfaces. Thus, the materials and thicknesses of walls in the environment play an important role in pulse distortion. Due to significant phase distortion caused by glass (see, Fig. 3.7), the corresponding MCC values for glass decrease faster than the MCC values for other materials as the pulse travels inside the medium.

3.6.3 Polarisation-dependent distortion

The surface reflection/transmission transfer functions for parallel and perpendicular polarizations are different. That is, pulse distortion effects due to surface reflections and transmission in the two polarization directions are different. This is referred to as PDD. The distortion due to propagation inside a medium is independent of the polarization direction. For the first reflection occurring at interface S_1, the amplitude and phase responses, for parallel and perpendicular polarizations with elementary reflection coefficients $\rho^{\parallel}$ and $\rho^{\perp}$, are shown in Figs. 3.3 and 3.4. The figures show that over the frequency range of 3.1-10.6 GHz, their magnitude and phase *variations* are similar, but the attenuations are different. As a result, the reflected pulse waveforms in parallel and perpendicular polarization directions are similar, but their magnitudes are different. We calculated the MCC values for up to the fourth reflected and transmitted pulses for all materials in Table 3.1. For normal incidences ($\theta_{\mathrm{i}} = 0$) the two polarization components experience the same distortion as is expected. By increasing the angle of incidence, the MCC values for perpendicular polarization do not change but for parallel polarization they decrease. Due to significant attenuation of the parallel polarization component at large angles of incidence, this does not cause appreciable distortion in the resultant pulse obtained by vector sum of two polarization components. When $\theta_{\mathrm{i}} = 60^{\circ}$, the MCC values corresponding to the resultant (combined) reflected pulses were calculated. The figures are shown in Table 3.3. They are almost the same as MCC values for normal incidences. For multiple transmitted pulses the MCC values are similar. In producing this table for the combined pulse, we assumed that the incident pulse's E-field is tilted 45° with respect to the plane of incidence. Also, we assumed that an ideal dual polarized antenna receives the components of the reflected pulse in two orthogonal polarizations without loss and combines them algebraically.

In order to compare the pulse waveforms in two orthogonal polarization directions, the relative magnitudes and phases of the harmonics after the nth reflection (or transmission) over the frequency spectrum of the pulse need to be considered. In Fig. 3.9 this is shown for the third reflection from chipboard of arbitrary, but limited, thickness when the angle of incidence is $\theta_{\mathrm{i}} = 60^{\circ}$. The attenuation in the parallel polarization component is significant compared to the perpendicular component but its variations

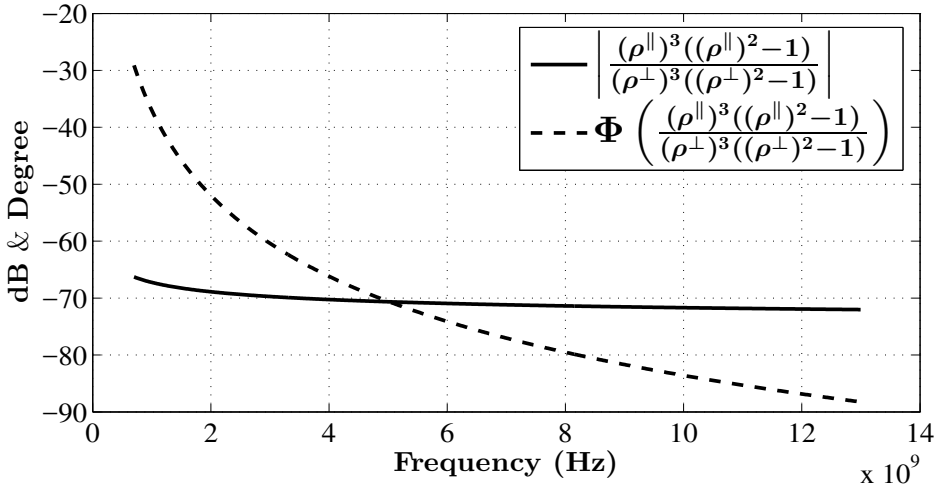

Figure 3.9: The frequency-dependent relative magnitude and relative phase of polarization components after third reflection (chipboard, $\theta_i = 60°$).

Table 3.3: MCC for reflected pulses (combined) excluding material distortion, $\theta_{\mathrm{i}} = 60°$.

	$n = 1$	$n = 2$	$n = 3$
Concrete	1.00000	1.00000	0.99999
Brick	1.00000	0.99998	0.99996
Plasterboard	1.00000	1.00000	1.00000
Wood	1.00000	0.99999	1.00000
Glass	1.00000	1.00000	1.00000
Chipboard	1.00000	0.99998	0.99996
Metal	0.98944	0.98946	0.98947
Medium dry ground	1.00000	0.99993	0.99971

over the frequency range is negligible. The phase variation is high at low frequencies. The variations of phase and amplitude for other materials, not shown here, are similar or less than those of chipboard.

3.6.4 Interpulse interference

For a single UWB pulse (3.7) incident on a wall surface, there are multiple reflected and transmitted pulses, as discussed in section 3.5. They may or may not overlap. This depends on the time duration of the pulse, thickness of the wall, angle of incidence, and characteristics of the material. This is because the spatial length of the UWB pulse is comparable to the thickness of the wall. When they do not overlap, the wall creates several separate pulses that are distorted due to the reflections and transmissions at the

Table 3.4: Typical thicknesses for materials considered in this chapter

Material	Concrete	Brick	Plasterboard	Wood	Glass	Chipboard
l(m)	0.15	0.15	0.01	0.05, 0.1	0.01	0.006, 0.01

interfaces S_1 and S_2, and the propagation in the lossy medium inside the wall. When the reflected or transmitted pulses partially overlap, the resulting signal's waveform can differ from that of the incident pulse. These partially overlapped pulses cannot be resolved by measurement if the time resolution is not sufficiently high and very fine time gating applied. In channel modelling it is desirable to distinguish between the IPI and the diffuse distortions caused by the materials as their estimation methods might be different [78, 79].

3.7 Power-Delay Profiles

In this section, the approximate PDPs for reflection and transmission responses of walls with representative physical and geometric characteristics are derived. The goal is to present the approach and to demonstrate some phenomena observed in measurements of UWB channels and incorporated in the standard UWB channel models in [88].

A precise model of a real channel is a continuous-time linear filter. In communication system design and performance evaluations usually a discrete-time model is used [102, 87]. Therefore, we wish to obtain a discrete tapped delay-line (TDL) model for wall effects on a UWB pulse. The time resolution of such a model depends on the bandwidth of the UWB pulse. A pulse with larger bandwidth provides better time resolution and consequently a better approximation to the real continuous-time channel response. We will consider a pulse with a relatively large bandwidth ($\approx$ 6.64 GHz). The resulting TDL models are also valid for smaller bandwidths.

The IEEE 802.15.4a UWB channel model is a modified Saleh-Valenzuela TDL model [115] given by

$$h(t) = \sum_{l=0}^{L} \sum_{k=0}^{K} a_{k,l} e^{j\phi_{k,l}} \delta(t - T_l - \tau_{k,l}), \tag{3.22}$$

where the phases $\phi_{k,l}$ are uniformly distributed in $[0, 2\pi)$. The number of clusters L is

a random variable that is Poisson distributed with mean $\overline{L}$. The cluster arrival times T_l and the ray arrival times within each cluster $\tau_{k,l}$ are also random and are described by two Poisson processes with different rates. The cluster powers, as well as the ray powers within each cluster, decay exponentially with delay. We refer readers to [88] for details of the standard UWB channels for various environments, and to [73] for physical interpretations of the channel parameters.

We want to relate the physical effects of single- and multiple-layer walls on UWB pulses to the TDL model (3.22) which is obtained by measurements. If there was no pulse waveform change, the multiple reflections and transmissions at walls could be easily modelled using standard TDL models. The distortions impose correlation loss when the reflected or transmitted pulse is correlated with the reference pulse. Therefore, it may be considered as a further attenuation when pulse matched filtering is performed. We include this loss in the path loss of each received pulse. The wall reflections and transmissions can then be approximated by a TDL filter. The delays and coefficients for each tap of the filter depend on the material and thickness of the wall and the angle of incidence of the pulses. The thicknesses of walls in indoor channels are various and usually depend on the material. For simulations we use typical thicknesses for building materials as given in Table 3.4. The approximate TDL model can be derived for each polarization and also for the overall received signal by an ideal dual-polarized antenna that captures the received signals in two orthogonal polarization directions and combines them algebraically. For brevity, we present the results for the overall received signal with the assumption that the polarization direction of the incident field is tilted 45° from the plane of incidence. We ignore signal attenuation due to spherical propagation of waves and consider only effects of the walls on planar EM pulses. The free-space propagation loss can be included later if it is desired.

The nth pulse, $r_n(t)$, reflected from or transmitted through a wall due to an incident pulse, $p(t) = p_{\text{sr}}(t)\exp(\mathrm{j}\,2\pi f_c t)$, is

$$r_n(t) = \mathscr{F}^{-1}\left\{P(f)H_n(f)\right\}, \tag{3.23}$$

where $H_n(f) = \big(R_n^{\perp}(f) + R_n^{\parallel}(f)\big)/\sqrt{2}$ for reflection, $H_n(f) = \big(T_n^{\perp}(f) + T_n^{\parallel}(f)\big)/\sqrt{2}$ for transmission and $P(f) = \mathscr{F}\{p(t)\}$. The factor $1/\sqrt{2}$ is for the decomposition of the

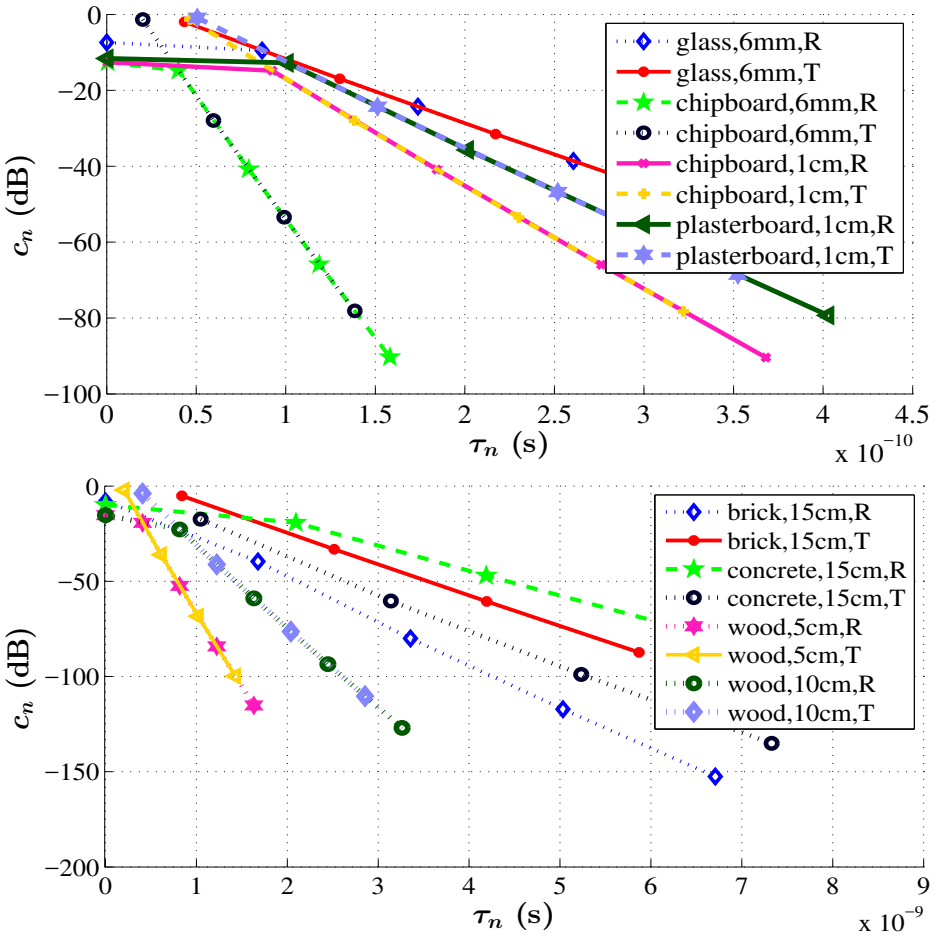

Figure 3.10: The PDPs for reflection and transmissions (R: reflection, T: transmission).

incident E-field vector into two equal length orthogonal vectors. Then the nth tap coefficient is

$$c_n = \|h_n\| \, m_c(p(t), r_n(t)), \tag{3.24}$$

and the corresponding tap delay, τ_n, is a delay point that maximizes the absolute value of the correlation function (3.3). For each c_n the corresponding delay is not necessarily unique as the maximum magnitude of the correlation function (3.3) can occur at several points. For all considered walls the maximum occurs at a single point. By using these characterizations of tap delays and tap coefficients, the derived PDPs for wall reflections and transmissions for representative materials are shown in Fig. 3.10. The first reflected pulses from some materials (e.g., glass and plasterboard) are weak. This is so because these materials are not good reflectors.

As shown in the figures, excluding the first reflection from S_1, both reflection and transmission responses of lossy dielectric walls have linear PDP in dB scale or

exponential PDP in linear scale. Therefore, the PDPs for reflections, $r_{\mathrm{PDP}}(t)$, and transmissions, $t_{\mathrm{PDP}}(t)$, for each wall can be represented as

$$r_{\mathrm{PDP}}(t) = c_0\delta(t) + \sum_{n=1}^{n=4} \mathrm{e}^{-\frac{\tau_n}{\gamma_\mathrm{r}}}\delta(t-\tau_n) \tag{3.25}$$

$$t_{\mathrm{PDP}}(t) = \sum_{n=1}^{n=4} \mathrm{e}^{-\frac{\tau'_n}{\gamma_\mathrm{t}}}\delta(t-\tau'_n), \tag{3.26}$$

where γ_r and γ_t are the exponential decay time constants equal to the slopes of the corresponding lines in Fig. 3.10. Then the TDL filter models are given by

$$r_{\mathrm{TDL}}(t) = \sqrt{c_0}\mathrm{e}^{\mathrm{j}2\pi\phi_0}\delta(t) + \sum_{n=1}^{n=4} \mathrm{e}^{-\frac{\tau_n}{2\gamma_\mathrm{r}}}\mathrm{e}^{\mathrm{j}2\pi\phi_n}\delta(t-\tau_n) \tag{3.27}$$

$$t_{\mathrm{TDL}}(t) = \sum_{n=1}^{n=4} \mathrm{e}^{-\frac{\tau'_n}{2\gamma_\mathrm{t}}}\mathrm{e}^{\mathrm{j}2\pi\phi'_n}\delta(t-\tau'_n), \tag{3.28}$$

where ϕ_n and ϕ'_n are the tap phases. The tap phases depend on the (unknown) carrier phase. For reflection, the first tap coefficient in (3.27) is an exception; its gain is almost the same as the second ray for the considered angle of incidence and polarization direction. For normal and close to normal incidences, i.e. for small values of θ_i, or in the case that the incident wave has a significant part of its strength in the perpendicular polarization component, the first ray reflected from some materials is weaker than the second ray which is reflected from the second interface (S_2 in Fig. 3.2). This is shown in Fig. 3.11 where the second reflected pulse from a wooden wall with 5 cm thickness is stronger than the first one. This is similar to the soft onset PDP of non-line-of-sight (NLOS) channels observed in various measurements [63, 121, 83]. However, comparing the relative delays of the first and second rays, we see that the soft onset phenomenon observed in measurement might be different from the phenomenon observed here. Due to the high resolution obtained using the numerical method used here, we can see a similar phenomenon but on a smaller scale.[3] The soft onset PDP refers to PDPs that are not exponentially decreasing, but that increase until reaching a maximum, then decrease. This effect is important in ranging systems [83].

[3]Therefore, we might call it a small-scale soft onset phenomenon.

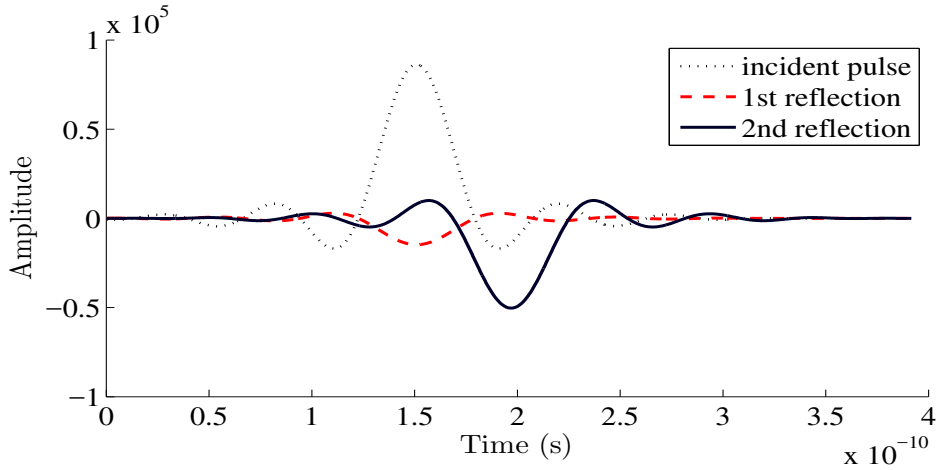

Figure 3.11: A soft onset phenomenon: 5 cm wooden slab, θ_i=0°

Now we consider the combined effect of two walls with impulse responses (IRs)

$$h_1(t) = A_1 \sum_{m=0}^{N_1-1} a_{1,m} \mathrm{e}^{\frac{-m\tau_\circ}{2\gamma_1}} \delta(t - m\tau_\circ), \text{ and}$$
$$h_2(t) = A_2 \sum_{m=0}^{N_2-1} a_{2,m} \mathrm{e}^{\frac{-m\tau_\circ}{2\gamma_2}} \delta(t - m\tau_\circ),$$

where γ_1 and γ_2 are the time constants of the corresponding exponential PDPs. This observation will provide a description for the random behaviour of the tap coefficients and the PDP of the clusters. This is a special case where the tap delays are the same for the two walls or layers. In general, the tap delays are different due to dependence on the thicknesses, angles of incidences and materials of the layers. In baseband transmission the coefficients $a_{1,m}$ and $a_{2,m}$ can only take the values ± 1. For bandpass transmission they are complex exponentials in the complex baseband model [102]. The convolution of these IRs, $h(t) = h_1(t) * h_2(t)$, gives the IR of the two walls. The nth tap coefficient of $h(t)$ is given by

$$c_n = A_1 A_2 \sum_{m=0}^{n} a_{1,m} a_{2,n-m} \mathrm{e}^{-\frac{m\tau_\circ}{2\gamma_1}} \mathrm{e}^{-\frac{(n-m)\tau_\circ}{2\gamma_2}}, \tag{3.29}$$

where $0 \leq n \leq N_1 + N_2$. Since $a_{1,m}$ and $a_{2,m}$ can take the values $\exp(\mathrm{j}\, 2\pi\phi)$ for some $\phi \in [0, 2\pi)$ (for bandpass transmission), the coefficients c_n have quasi-random behaviour. By assuming that ϕ is uniformly distributed in the interval $[0, 2\pi)$ and using the central limit theorem (CLT) [97], the distribution of c_n can be approximated

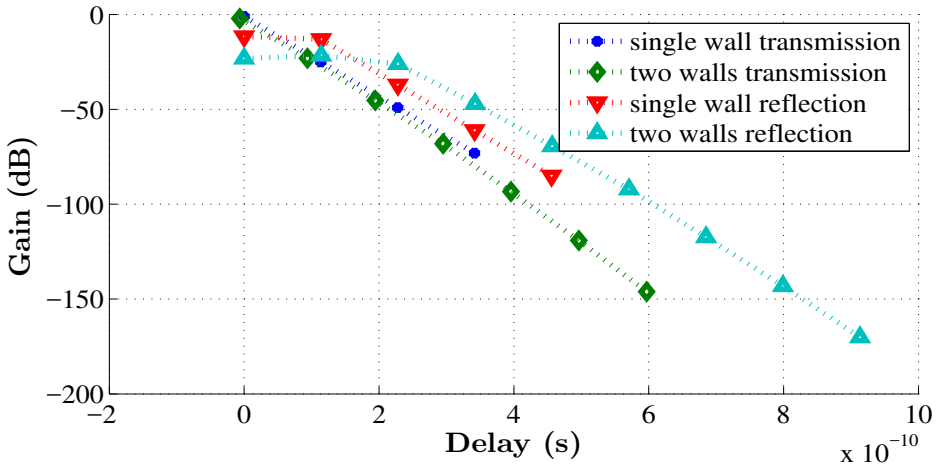

Figure 3.12: PDP of two similar walls (1 cm plasterboard). Normal incidence.

by a normal distribution with mean $\mu_n = 0$ and a variance given by

$$\sigma_n^2 = A_1^2 A_2^2 \sum_{m=0}^{n} \mathrm{e}^{-\frac{m\tau_o}{\gamma_1}} \mathrm{e}^{-\frac{(n-m)\tau_o}{\gamma_2}}. \tag{3.30}$$

As a result $|c_n|$ is Rayleigh distributed [97]. The CLT does not provide a good approximation if the number of summands in (3.30) is not sufficiently large. Therefore, the normality of the distributions of the leading and tail tap coefficients are not guaranteed by the CLT. In general, the PDP of this resultant system, $h_1(t) * h_2(t)$, is not exponential.

Example 3.7.1. For demonstration of PDP for multiple reflections and transmissions, we consider two plasterboard walls each of thickness 1 cm separated by a gap. The PDP of transmission through and reflection from a 1 cm plasterboard is shown in Fig. 3.10. The plots of PDP corresponding to the single and double walls are shown in Fig. 3.12. Note that the PDPs are not always exponential.

Example 3.7.2. Consider a double-layer wall, or two parallel walls in cascade, blocking the straight path connecting transmitter and receiver. The first wall consists of wood with thickness 5 cm and the second wall consists of concrete with thickness 8 cm. The PDP for the transmission through the double layer wall is shown in Fig. 3.13. As it is clear from the graph, the density of rays at both ends is less than the density of rays arriving in the middle. In systems that employ pulses with smaller bandwidth, several rays fall within one delay bin with size equal to the reciprocal of the bandwidth. Therefore, the mean values of the received power within equal size delay bins may not

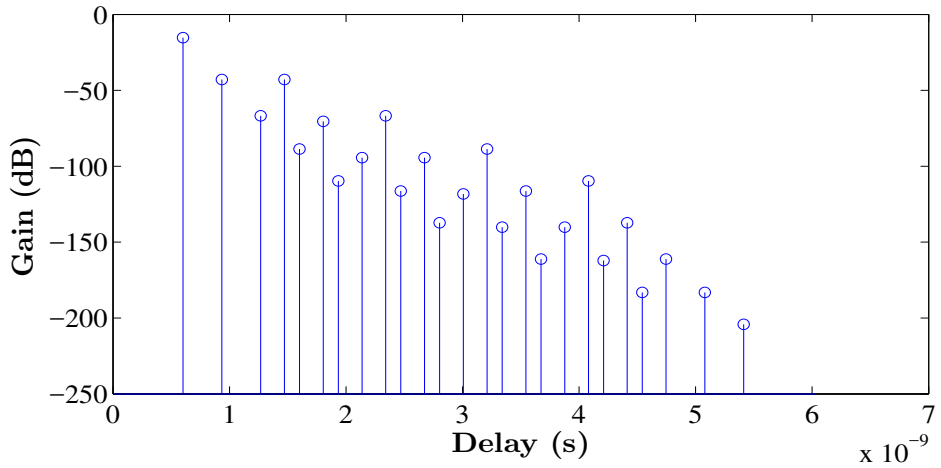

Figure 3.13: A cluster of rays created by transmission through two parallel walls: wood (5 cm) and concrete (8 cm). $\theta_i = 45°$.

have exponential decay.

3.8 Conclusion

In this Chapter, we analysed the interactions of UWB pulses with building walls. Single-layer walls create several distorted pulses when illuminated by UWB pulses. The distortion of individual pulses due to frequency dependence of parameters of typical building materials is not the major source of distortion. The major source of distortion is IPI which occurs when the reflected/transmitted pulses partially overlap. A method for derivation of the PDPs of wall reflection and transmission is introduced using the MCCs which incorporates pulse distortion as a power loss. The derived PDPs include the overall effect of wall transmissions and reflections. Excluding the first reflected pulse, the PDPs of reflections from and transmissions through single-layer walls are exponential. For multilayer walls, or combinations of multiple reflections and transmissions, the PDP is not exponential. Their PDPs are the convolutions of several exponential PDPs. The PDP derivation of this chapter describes the multicluster structure of the UWB channel models obtained by measurements. The approach can be used in deterministic and statistical modelling of UWB channels.

Chapter 4

Adaptive MMSE Receivers and Their Stability

Synopsis In communication systems that use a linear modulation scheme for transmission, the FS samples of the received signal from a channel constitute a wide-sense cyclostationary (WSCS) time series. Hence, standard Fourier transform techniques cannot be used to study the spectral characteristics of the received FS samples or to derive the TF of the corresponding digital MMSE receiver. In this chapter, an analytical expression for the TF of the FS MMSE equaliser is derived which includes the effects of the C/D converter used at the receiver front end. Using the the derived TF, the sources of instability of the FS LMS algorithm and the effects of the equaliser length and sampling phase on convergence of the LMS algorithm are explained. For stabilization of the FS LMS algorithm, conditions on the front-end C/D converter are provided that when satisfied the LMS algorithm becomes more stable. The learning characteristics of the modified receiver is better than the leaky-FS LMS algorithm. Theoretical results are corroborated by simulations.

4.1 Introduction

Modern digital receivers convert the received CT noisy signal into a DT signal at the receiver front end as early as possible [77]. This is done by passing the received signal through a filter and then sampling at a rate which is usually higher than the symbol rate [77, 102, 15, 40, 22]. The combination of prefilter and sampler, which converts the CT signal to a DT signal, is referred to as a C/D converter.

A linearly modulated transmit signal can be represented as [102]

$$s(t) = \sum_n \mathrm{d}_n p(t - nT), \tag{4.1}$$

where, $\{\mathrm{d}_n\}$ is the sequence of complex data symbols, $p(t)$ is the pulse shaping filter's IR, and T is the symbol interval. The two-sided bandwidth of $p(t)$ is usually less than $2/T$. Therefore, according to the sampling theorem [102], $T/2$-spaced samples of the received signal, $r(t)$, from a linear channel form a characterizing set. That is, $r(t)$ can be reconstructed from these samples and the samples can be used in a digital receiver to perform synchronization and equalization with no performance loss. Theoretically, any sampling rate satisfying the conditions of the sampling theorem [43] can be used, but due to its simple implementation, $2/T$ is the most common sampling rate [147, 42, 105].

A popular linear equaliser that is designed to perform channel equalization using $T/2$-spaced samples of the received signal is the FS MMSE equaliser [102]. When the sampling rate is $2/T$, the FS MMSE equaliser is implemented using a TDL filter whose tap spacing is $T/2$ [105, 102]. A major advantage of the FS MMSE equaliser over its symbol-spaced (SS) counterpart is its capability to compensate for sampling phase errors (which result in band edge distortions) and any other linear distortion caused by the communication channel [147, 42, 102].

Using the celebrated FS LMS algorithm [147, 40, 102, 8], the FS MMSE equaliser can be implemented adaptively. Adaptivity, simplicity and low complexity are major advantages of the LMS algorithm for equalizing *a priori* unknown and slowly time-varying channels [47, 117].

It is well known that the optimum infinite-length $T/2$-spaced MMSE equaliser is not unique, but the corresponding suboptimal finite-length MMSE equaliser is unique [41, 40, 105]. Therefore, a practical adaptive algorithm will converge to this unique filter when it is convergent. A major drawback of the FS LMS algorithm is its instability [41]. This is due to the increasing magnitudes of some of the equaliser tap weights [41]. A TDL equaliser with large tap gains is sensitive to input perturbations. Since in the LMS algorithm noisy estimates of the gradient of the MSE surface are used to update the tap weights [102], the FS LMS algorithm is unstable. According to this argument,

in order to stabilize the FS LMS algorithm, the tap gains of the equaliser should be restricted to small values. Usually this is done by modifying the cost function of the MMSE estimation, that is, by defining the modified cost function by

$$J_\mu(\mathbf{q}) = J_{\mathrm{MSE}}(\mathbf{q}) + \mu\|\mathbf{q}\|^2, \tag{4.2}$$

where $\mathbf{q}$ is the tap-weight vector, $J_{\mathrm{MSE}}(\mathbf{q})$ is the MMSE estimation cost function, and μ is the tap-leakage parameter [147, 41, 117]. The modified cost function penalizes the squared norm of the vector $\mathbf{q}$, and therefore, the tap gains cannot grow large when this modified cost function is used. The modified LMS algorithm based on the cost function $J_\mu(\mathbf{q})$ is referred to as the tap-leakage algorithm [41] or the leaky LMS algorithm [47, 117].

Using a leakage parameter in the tap leakage algorithm is an instance of the well-known regularization method of Tikhonov [140, 48] which is essentially a method to avoid the singularities that can exist in the FS MMSE equalization. It avoids the singularities by adding a multiple of the identity matrix to the correlation matrix of the input DT signal, or equivalently, by adding a virtual white noise process with power spectral density (PSD) μ to the input signal [47, 117]. When the leaky LMS algorithm is convergent, its limit differs from the optimum MMSE solution (Wiener solution) and its complexity is higher than that of the conventional LMS algorithm [117]. Its convergence and limit depend on the choice of parameter μ [47, 117]. By using the tap-leakage method the vanishing eigenvalues of the input samples correlation matrix can be removed, but this does not guarantee the convergence of the adaptive algorithm. Convergence of the modified LMS (leaky LMS) algorithm still depends on the eigenvalue spread of the correlation matrix.

There is a major difference between the SS sampling receiver and FS sampling receiver. Since the FS sampled received signal is not a wide-sense stationary process, the channel correlation matrix is not Toeplitz. Therefore, the impulse response (IR) and TF of the corresponding MMSE equaliser are time-variant. The Fourier transform, which is commonly used for derivation of the TF of the SS MMSE equaliser [40, 102, 117], cannot be used directly to study the eigenvalues of the correlation matrix of a FS sampled signal or to derive the TF of the FS MMSE equaliser. In this chapter, an

explicit formula for the TF of the FS MMSE equaliser is derived. Using the TF, all aspects of the FS MMSE equaliser can be studied.

The stability analysis of the adaptive FS equaliser, implemented using the LMS algorithm, is usually based on simplifying assumptions or approximations. For instance the analysis in [147] relies on a two-stage approximation of the channel correlation matrix. The first is the approximation of a non-Toeplitz channel matrix by a Toeplitz matrix and the second is the approximation of a non-cyclic Toeplitz matrix by a cyclic Toeplitz matrix. In the course of these approximations, the sources of instability are avoided.

In [42, 41], the instability of the FS LMS algorithm is attributed to the accumulation of noise along the eigenvectors of the correlation matrix of the input samples corresponding to small eigenvalues. There the claim is that the algorithm cannot control or constrain the equaliser filter taps along these eigenvectors, so after a while some of the tap weight magnitudes start to grow due to implementation noise. The same description has been followed later in other places [105, 102]. Using the TF of the FS MMSE equaliser, we show that the increasing tap weight magnitudes by recursion of the LMS algorithm can be a natural consequence of two phenomena: 1) constructive addition of frequency domain sinusoidals corresponding to time domain TDL filter over some frequency intervals over which the equaliser does not have control, 2) sampling time offsets which create spectral dips over the rolloff regions of the transmitted pulse. Then, the appropriate approach to control the tap weight magnitudes is introduced.

While the convergence and stability of the SS LMS algorithm has a refined theory [102, 117], the theory for FS LMS algorithm has not yet been completed [142]. Major contributions in stability analysis of the FS equalization are summarized in [105]. In the early stages of development of FS equalisers, the problem of instability of the LMS algorithm was a concern [44, 147, 41, 106, 42, 148]. In [147] it is stated that the instability of a $T/2$-spaced structure is due to insufficient precision in implementation of the LMS algorithm; otherwise the algorithm is stable. Later, in [41], the sources of the instability are investigated and the leaky LMS algorithm (which was already in [147]) is used to stabilize the algorithm. In [41], it was concluded that the instability is due to accumulation of implementation noise. In [15, p. 283, footnote], it was

commented that there seems to be a general agreement that the instability is not an issue and the regularization methods are not necessary in implementation of FS LMS algorithm. In [142] the instability issue is reconsidered and regarding that some open questions are explained. The diversity of views regarding convergence and stability of the adaptive FS MMSE equaliser indicates that the theory of FS MMSE equalisers is not complete yet.

Our approach to spectral analysis of the FS MMSE equaliser is different from the existing methods. The existing analyses of the FS MMSE equaliser are based on the statistical properties (covariance matrix) of the input sampled signal to the equaliser. Therefore, the behavior of the equaliser is indirectly speculated using the statistical properties of the input data. In this chapter, the properties of the FS MMSE equaliser are studied based on the derived TF of the optimum FS MMSE equaliser.

The contributions of this chapter are

1. Derivation of the TF of a FS MMSE equaliser (the Wiener solution for FS equaliser).
2. Analysis of the effects of the sampling phase on FS MMSE equaliser's TF.
3. Analysis of the effects of the C/D converter on the performance of FS MMSE equaliser and LMS algorithm.
4. Investigation of the convergence and stability of the LMS algorithm using properties of the optimum solution.
5. Explanation of the effect of the length of the equaliser on the stability of the LMS algorithm.
6. Introduction of ensemble-averaged equaliser norm as an appropriate tool for stability analysis of the LMS algorithm.

The remainder of this chapter is organised as follows. In Section 4.2, a mathematical model for the communication system and the structure of the front-end C/D converter of a typical digital receiver are described. Then in Section 4.3, the TF of a CT MMSE, without considering the front-end C/D converter, is described and

some issues involved in its description and applications are reviewed. The TF of a FS MMSE equaliser is derived in Section 4.4. The spectral characteristics of the FS MMSE equaliser, the effects of the C/D converter, the sampling phase and the equaliser length on its behavior are analyzed in Section 4.5. In Section 4.6, the stabilization of the FS LMS algorithm, without further computational cost, is described. In Section 4.7, the theoretical results are demonstrated by simulation. Conclusions are drawn in Section 5.

4.2 System Model

We assume that the baseband transmit pulse, $p(t)$, for transmission of symbols at rate $R \triangleq 1/T$ is real-valued and its two-sided bandwidth is $(1+\alpha)R$, for some rolloff factor $0 \leq \alpha \leq 1$. A linearly-modulated lowpass transmit signal, carrying complex symbols d_n [102], is given by (4.1). At the transmitter, $s(t)$ is upconverted to a real bandpass signal $s_c(t) = \mathrm{Re}[s(t)\mathrm{e}^{\mathrm{j}\,2\pi f_c t}]$ and transmitted over a real bandpass channel with IR $h_c(t,\tau)$. The real part of a complex number is denoted by $\mathrm{Re}[\cdot]$. At the receiver the received signal is filtered by a non-distorting bandpass filter to remove interferences from neighboring frequency channels. The output of the bandpass filter is down-converted using a local oscillator at frequency f_c' which is an approximation to the carrier frequency f_c. The down-converted complex-valued noisy CT signal can be represented as

$$r(t) = \int_{\mathbb{R}} h(t,\tau)s(t-\tau)\,\mathrm{d}\tau + z(t), \tag{4.3}$$

where $h(t,\tau)$ is the equivalent lowpass IR of the channel and $z(t)$ is the equivalent lowpass channel noise. We assume that $z(t)$ is a stationary circularly symmetric Gaussian process with zero mean and its PSD over the relevant frequency band is $2N_0$ [102]. When $f_c \neq f_c'$, and there is carrier phase offset, θ, the equivalent lowpass channel IR, $h(t,\tau)$, includes the effect of the carrier offset. That is, $h(t,\tau) = \mathrm{e}^{\mathrm{j}\,2\pi(f_c - f_c')t+\theta}h'(t,\tau)$, where $h'(t,\tau)$ is the lowpass channel IR with perfect carrier frequency and phase synchronization. In this chapter, we assume that $f_c = f_c'$ and $\theta = 0$.

The received baseband signal, $r(t)$, is passed through a C/D converter. The C/D

converter consists of a prefilter with IR $h_{\mathrm{PF}}(t)$ and a sampler whose sampling rate is $f_s = 1/T_s$. The samples at the output of the C/D converter are given by $r_{\mathrm{PF}}(kT_s - t_0) = u_k + z_k,\ k \in \mathbb{Z}$, where

$$u_k = \int u(t) h_{\mathrm{PF}}(kT_s - t_0 - t)\,\mathrm{d}t, \text{ and } z_k = \int z(t) h_{\mathrm{PF}}(kT_s - t_0 - t)\,\mathrm{d}t. \tag{4.4}$$

In (4.4), t_0 is the sampler clock delay with respect to a reference clock and $u(t)$ is the noise-free received signal. Since the noise is white (and hence stationary), its statistics are independent of the choice of t_0.

The first task of a digital receiver is the extraction of a countable set of variables from the received CT random signal $r(t)$ that retains all information about the channel $h(t, \tau)$ and the transmitted signal $s(t)$ that are available in the noise-free received signal. In extraction of the DT signal from the received CT signal, the irrelevant out-of-band part of the additive noise is removed. The statistics of the relevant part of the noise, which accompanies the extracted DT signal, plays an important role in the derivation of the optimum digital receivers [154, 139, 77].

For discretisation, the received signal $r(t)$ is filtered by a prefilter $h_{\mathrm{PF}}(t)$, referred to as a prefilter, and sampled at a rate f_s. The output of the sampler is a sequence $\{r_{\mathrm{PF}}(kT_s)\}_k$, where $T_s = 1/f_s$ is the sampling interval and $r_{\mathrm{PF}}(t) = r(t) * h_{\mathrm{PF}}(t)$. The sampling interval T_s is rarely equal to the symbol interval T [77]. The DT signal $\{r_{\mathrm{PF}}(kT_s)\}_k$ is quantized and forwarded for further digital signal processing. In digitally implemented receivers all major operations are performed in the digital domain [77]. These can include matched filtering, carrier phase and symbol-timing synchronizations, channel estimation and equalization [77]. The typical digital communication system, of interest, is shown in Fig. 4.1. Detailed block diagrams can be found in [77], [15] or [143]. The C/D converter is indicated by the dashed rectangle in Fig. 4.1.

We assume that the channel is stationary[1], that is, $h(t, \tau) = h(\tau)$. Then the

[1]This assumption is required over the training period of an adaptive equaliser. Slow variations of the channel can be tracked by adaptive receivers if the learning speed of the algorithm is sufficiently high [102].

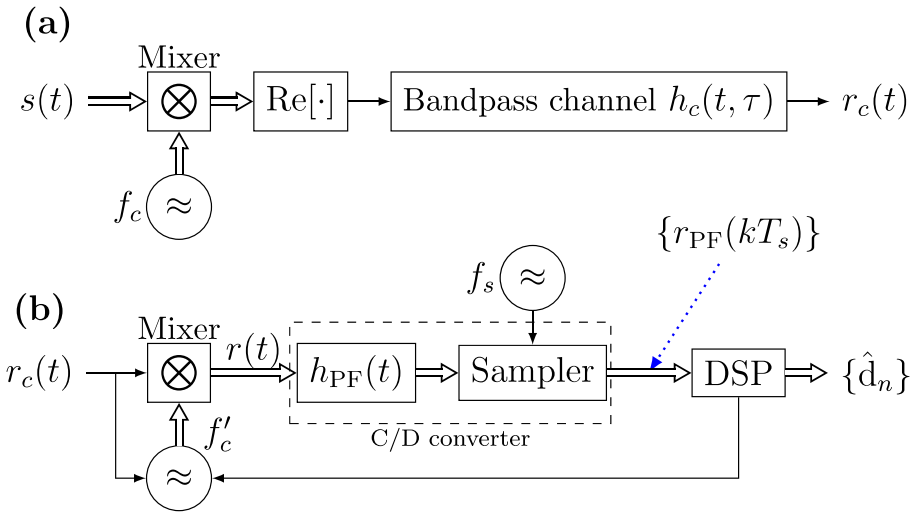

Figure 4.1: Digital communication system. Real-valued signal flows are shown by single-line arrows and the complex-valued signal flows are shown with double-line arrows. The signal presented to the prefilter $h_{\rm PF}(t)$ is the lowpass signal $r(t) = u(t) + z(t)$. f_c' is a coarse approximation to the carrier frequency f_c at the receiver front end. (a) Creation of the real bandpass received signal $r_c(t)$. (b) Processing blocks in the front-end of a typical digital receiver [77, 15, 143].

noise-free received signal can be represented as

$$u(t) = \sum_n {\rm d}_n h_{\rm PR}(t - nT), \tag{4.5}$$

where $h_{\rm PR}(t) = h(t) * p(t)$ is the pulse response of the channel. Due to the channel noise, the extracted statistic $\{r_{\rm PF}(kT_s)\}$ contains a random noise component. The statistical properties of the noise samples depend on the characteristics of the front-end prefilter $h_{\rm PF}(t)$ and the sampling rate f_s. Its PSD is given by (4.11).

4.3 Continuous-time MMSE equaliser

The CT MMSE equaliser TF can be obtained by using the basic principles of MMSE estimation. Assuming the transmitted lowpass signal (4.1) and the received lowpass signal (4.3), the CT MMSE equaliser, without any further constraint, is a linear filter $q(t)$ that minimizes the MSE cost function defined by

$$J_{\rm MSE} = {\rm E}[|{\rm d}_n - \hat{\rm d}_n|^2], \tag{4.6}$$

where $\hat{\mathrm{d}}_n = \int q(nT-\xi)r(\xi)\,\mathrm{d}\xi$ and ξ is a dummy integration variable. In (4.6) the expectation is with respect to the random input symbol d_n and the noise process $z(t)$. We assume that the data symbols are independent, identically distributed with zero mean and variance $\mathcal{P}_\mathrm{d} = \mathrm{E}[|\mathrm{d}_n|^2]$. We also assume that the data symbols are independent of the noise. By the orthogonality principle of the MMSE estimation method for CT stochastic processes [97, Chapter 13], the estimate $\hat{\mathrm{d}}_n$ is optimal in the MSE sense if and only if $\mathrm{E}[(\mathrm{d}_n - \hat{\mathrm{d}}_n)\overline{r(t)}] = 0$ for all $t \in \mathbb{R}$. By expansion, using the independence of symbols and noise samples, and then applying the CT Fourier transform, this equation leads to an equivalent functional equation in the Fourier domain given by [42, 40][2]

$$\left(\Phi^T_{h_\mathrm{PR}}(f) + \frac{2N_0}{\mathcal{P}_\mathrm{d}}\right) Q(f) = \overline{H_\mathrm{PR}(f)}, \tag{4.7}$$

where

$$\Phi^T_{h_\mathrm{PR}}(f) = \sum_k |H_\mathrm{PR}(f - \frac{k}{T})|^2. \tag{4.8}$$

Regarding (4.7) and its applications, we make the following comments:

1) $H_\mathrm{PR}(f)$ is the Fourier transform of the total IR of the channel from transmitter up to the receiver input. In digitally-implemented receivers, the equaliser is preceded by a C/D converter. The effect of the C/D converter cannot be seen explicitly from (4.7).

2) The input noise to the equaliser needs to be white to ensure the optimality and stability of the equaliser. If the input noise is not white, it needs to be whitened before feeding the equaliser. This is possible only if the noise process is not singular, i.e., its PSD function is bounded away from zero.

3) Since $\Phi^T_{h_\mathrm{PR}}(f) \geq 0$, in the presence of additive white noise with nonzero PSD, the equaliser can be defined by [40, 102]

$$Q(f) = \frac{\overline{H_\mathrm{PR}(f)}}{\Phi^T_{h_\mathrm{PR}}(f) + \frac{2N_0}{\mathcal{P}_\mathrm{d}}}. \tag{4.9}$$

[2]Using the orthogonality principle of the MMSE estimation method for CT stochastic process [97], simplifies the derivation of the TF of the CT MMSE equaliser compared to [40, p. 7.4].

As the denominator in (4.9) is T-periodic, the equaliser can be described as a cascade of the matched filter and possibly an infinite-length T-spaced transversal filter.

4) The equaliser defined by (4.9) is optimum in the MSE sense if the sampling at the equaliser output has zero phase offset. Otherwise, (4.9) should be replaced by $Q_{t_0}(f) \triangleq Q(f)\mathrm{e}^{\mathrm{j}2\pi t_0 f}$, where t_0 is a symbol timing error. t_0 is usually unknown *a priori* [77].

In Section 4.4, we will see how the TF of the MMSE equaliser (4.9) is changed when the C/D converter is included in the system.

4.4 Discrete-Time MMSE Equaliser and Its Transfer Function

In digital receivers, the MMSE equaliser is implemented in DT. The front end of such a receiver consists of a lowpass prefilter. The prefilter performs several functions including the suppression of the out of band additive noise and the interfering signals from neighbouring frequency channels which have not been removed by the bandpass front-end filter. Therefore, the bandwidth of the prefilter cannot be chosen to be arbitrarily large. On the other hand the prefilter should pass the useful received signal component without distortion, so its bandwidth cannot be chosen to be arbitrarily narrow. The output of the prefilter is sampled at a constant rate $1/T_s$. The extracted discrete time signal is then forwarded to a T_s-spaced TDL MMSE filter. Its output is sampled at the symbol rate, $1/T$, where each sample is an estimate of a transmitted symbol [102]. Theoretically, T_s can be any small real number such that $1/T_s \geq (1+\alpha)R$. When T/T_s is irrational, the equaliser cannot be implemented adaptively, because in this case the sampled signal has no stationarity property, and therefore, the optimum equaliser filter changes within one symbol interval. Therefore, this case should be excluded in practical considerations. When T/T_s is rational, i.e., $T/T_s = p_1/p_2$ for two relatively prime natural numbers p_1 and p_2, the T/p_2-spaced samples of the prefilter output can be used by a T/p_2-spaced MMSE equaliser which is optimized to minimize the MSE between the transmitted symbols and every p_1th output of the equaliser filter. That is, the implementation require sampling at rate p_2/T and equaliser with

tap spacing T/p_2. In summary, the sampling rate increases by a factor of p_2 and computational complexity of the TDL equaliser increases by a factor of $p_2(2L+1)$ multiplications and $(2Lp_2+1)Lp_2-(2L+1)L$ additions per symbol, assuming that the equaliser's time span is $(2L+1)T$. In high data-rate communications these sampling rates and complexity increases are not desirable. Therefore, usually, a smaller p_2 for practical purposes is suitable. As a result $p_2 = 2$ and $p_1 = 1$ is the most common choice [147, 42, 106], but this is not always the case [15, 102, 22].

In digital implementation of the MMSE receiver, the matched filter and the T-spaced TDL equaliser filter are combined and the resulting T_s-spaced TDL equaliser is responsible for performing their functions [42, 105].

In early studies of FS MMSE equalisers the effects of the prefilter on the equaliser performance and stability were usually ignored [42, 105, 102]. Improper choice of the front-end C/D converter can result in a malfunctioning adaptive equaliser. This can be seen through divergence of the tap-weight adaptation algorithm or by an indefinite increase of the equaliser tap weight magnitudes. The latter in turn results in an unstable equaliser. The leaky LMS algorithm [41] or its variants [128, 61, 148, 92] are usually applied to avoid this instability. Using this algorithm imposes a complexity cost and violates the optimality of the receiver as the residual MSE increases when the algorithm is applied [148] and the estimate obtained is biased [117]. By characterizing the sources of these problems and designing the front-end processing properly, they can be avoided without additional complexity or performance degradation caused by the leaky LMS algorithm.

In order to derive the TF of the FS MMSE equaliser, we use the block diagram of Fig. 4.1. The received signal $r(t)$ is prefiltered by $h_{\mathrm{PF}}(t)$ and sampled at a rate f_s. The output samples are given by

$$r_{\mathrm{PF}}(kT_s - t_0) \triangleq u_k + z_k, \ (k \in \mathbb{Z}), \tag{4.10}$$

where u_k and z_k are samples of the noise-free filtered signal (4.5) and filtered noise components, respectively, and t_0 is the sampler clock phase offset with respect to a reference clock. Since the noise is white (and hence stationary), its statistics are independent of the choice of t_0. Therefore, the sampler phase offset can be considered

as part of the channel IR and we can ignore its effects in the following. The PSD of the noise process $\{z_k\}$ is given by

$$S_{z_k}(f) = 2N_0\Phi^{T_s}_{h_{\rm PF}}(f), \tag{4.11}$$

where

$$\Phi^{T_s}_{h_{\rm PF}}(f) \triangleq \sum_m |H_{\rm PF}(f - mf_s)|^2. \tag{4.12}$$

Assume that the DT signal at the output of the C/D converter, $\{r_{\rm PF}(kT_s)\}_{k\in\mathbb{Z}}$, is input to a FS TDL equaliser with tap weights $\{q_k\}_{k\in\mathbb{Z}}$ and tap spacing $T_s = 1/f_s$. In the following, we assume that the sampling phase offset is zero ($t_0 = 0$). We will consider the effects of nonzero sampling phase offset later. Then, the T-spaced estimates $\hat{\rm d}_n$ of the transmitted data symbols ${\rm d}_n$ are obtained by sampling the output of the equaliser. That is

$$\hat{\rm d}_n = \sum_k q_k r_{\rm PF}(nT - kT_s), \qquad (n \in {\rm Z}). \tag{4.13}$$

The DT filter $\{q_k\}$ is the MMSE equaliser if and only if it satisfies the following orthogonality relations

$${\rm E}[({\rm d}_n - \hat{\rm d}_n)\overline{r_{\rm PF}(lT_s)}] = 0 \qquad \forall l \in \mathbb{Z}. \tag{4.14}$$

Using (4.13), (4.14) can be written as

$${\rm E}[{\rm d}_n\overline{r_{\rm PF}(lT_s)}] = {\rm E}[\sum_k q_k r_{\rm PF}(nT - kT_s)\overline{r_{\rm PF}(lT_s)}\ ]\ \forall l \in \mathbb{Z}. \tag{4.15}$$

We now derive the TF of a FS MMSE equaliser using (4.15). To this end, we use the Poisson summation formula (PSF) [43], specifically we use the form given by

$$\sum_l g_1(lW) = \frac{1}{W}\sum_l G_1(\frac{l}{W}), \tag{4.16}$$

which is valid for all $W > 0$ and a wide range of functions $g_1(t)$ including the practical signals of interest in the communication model used in this chapter (see [43] for details).

Noting that the data symbols and the noise samples are white and independent of each other, we can write

$$\mathrm{E}[\mathrm{d}_n \overline{r_{\mathrm{PF}}(lT_s)}] = \mathcal{P}_{\mathrm{d}} \overline{g(lT_s - nT)}, \tag{4.17}$$

where $g(t) = h_{\mathrm{PR}}(t) * h_{\mathrm{PF}}(t)$ and $\mathcal{P}_{\mathrm{d}} = \mathrm{E}[|\mathrm{d}_n|^2]$. Similarly

$$\begin{aligned} &\mathrm{E}[\sum_k q_k r_{\mathrm{PF}}(nT - kT_s) \overline{r_{\mathrm{PF}}(lT_s)} \,] = \\ &\mathcal{P}_{\mathrm{d}} \sum_k q_k \Big[\sum_m g((n-m)T - kT_s) \overline{g(lT_s - mT)} \\ &+ \frac{2N_0}{\mathcal{P}_{\mathrm{d}}} \int h_{\mathrm{PF}}(nT - kT_s - t) \overline{h_{\mathrm{PF}}(lT_s - t)} \, \mathrm{d}t \Big]. \end{aligned} \tag{4.18}$$

Our goal is to find the equaliser tap-weight sequence $\{q_k\}$, whose DT Fourier transform is given by

$$Q_{T_s}(f) = \sum_k q_k \mathrm{e}^{-\mathrm{j}\,2\pi k T_s f}. \tag{4.19}$$

We calculate the DT Fourier transform of both sides of (4.15), given by (4.17) and (4.18), with respect to l and employ the PSF. For simplification, we assume that $T = \nu T_s$ for some $\nu \in \mathbb{N}$. Then $\mathrm{e}^{-\mathrm{j}\,2\pi m p \frac{T}{T_s}} = 1$. The DT Fourier transform of $\{\mathcal{P}_{\mathrm{d}} \overline{g(lT_s - nT)}\}_{l \in \mathbb{Z}}$ is

$$\begin{aligned} &\mathcal{P}_{\mathrm{d}} \sum_l \overline{g(lT_s - nT)} \mathrm{e}^{-\mathrm{j}\,2\pi l T_s f} \\ &\quad = \frac{\mathcal{P}_{\mathrm{d}}}{T_s} \mathrm{e}^{-\mathrm{j}\,2\pi n T f} \sum_p \overline{G(-f - \frac{p}{T_s})} \mathrm{e}^{-\mathrm{j}\,2\pi n p \frac{T}{T_s}} \\ &\quad = \frac{\mathcal{P}_{\mathrm{d}}}{T_s} \mathrm{e}^{-\mathrm{j}\,2\pi n T f} \sum_p \overline{G(-f - \frac{p}{T_s})}, \end{aligned} \tag{4.20}$$

where the first equality follows from the PSF with $g_1(t) = \overline{g(t - nT)} \mathrm{e}^{-\mathrm{j}\,2\pi t f}$ and $W = T_s$. Similarly, the DT Fourier transform of the first expression within the square brackets in (4.18), with respect to l, is calculated as

$$\sum_m g((n-m)T - kT_s) \sum_l \overline{g(lT_s - mT)} e^{-\mathrm{j}\,2\pi l T_s f} \tag{4.21}$$

$$= \sum_m g((n-m)T - kT_s) \left(\frac{1}{T_s} \mathrm{e}^{-\mathrm{j}2\pi mTf} \sum_p \overline{G(-f - \frac{p}{T_s})} \right)$$
$$= \frac{1}{T_s} \sum_p \overline{G(-f - \frac{p}{T_s})} \sum_m g((n-m)T - kT_s) \mathrm{e}^{-\mathrm{j}2\pi mTf}$$
$$= \frac{1}{TT_s} \mathrm{e}^{-\mathrm{j}2\pi f(nT - kT_s)} \sum_p \overline{G(-f - \frac{p}{T_s})} \sum_m G(-f - \frac{m}{T}) \mathrm{e}^{\mathrm{j}2\pi km/\nu}, \tag{4.22}$$

where we have used the PSF in obtaining the second and third equalities.

Using the PSF and properties of the CT Fourier transform, the DT Fourier transform of the second expression within square brackets in (4.18), with respect to l, is given by

$$\frac{2N_0}{\mathcal{P}_\mathrm{d}} \int h_\mathrm{PF}(nT - kT_s - t) \left(\frac{1}{T_s} \mathrm{e}^{-\mathrm{j}2\pi tf} \sum_p \overline{H_\mathrm{PF}(-f - \frac{p}{T_s})} \mathrm{e}^{-\mathrm{j}2\pi t(\frac{p}{T_s})} \right) \mathrm{d}t \tag{4.23}$$
$$= \frac{2N_0}{T_s \mathcal{P}_\mathrm{d}} \sum_p \overline{H_\mathrm{PF}(-f - \frac{p}{T_s})} \int h_\mathrm{PF}(nT - kT_s - t) \mathrm{e}^{\mathrm{j}2\pi t(-f - \frac{p}{T_s})} \, \mathrm{d}t$$
$$= \frac{2N_0}{T_s \mathcal{P}_\mathrm{d}} \sum_p \overline{H_\mathrm{PF}(-f - \frac{p}{T_s})} H_\mathrm{PF}(-f - \frac{p}{T_s}) \mathrm{e}^{-\mathrm{j}2\pi(nT - kT_s)(\frac{p}{T_s} + f)}$$
$$= \frac{2N_0}{T_s \mathcal{P}_\mathrm{d}} \mathrm{e}^{-\mathrm{j}2\pi f(nT - kT_s)} \sum_p |H_\mathrm{PF}(-f - \frac{p}{T_s})|^2. \tag{4.24}$$

Finally, using (4.20), (4.22) and (4.24), after simplifying some common factors and changing the variable f to $-f$ on both sides, we can express (4.15) in the Fourier domain as

$$\sum_p \overline{G(f - \frac{p}{T_s})} = \sum_k q_k \mathrm{e}^{-\mathrm{j}2\pi fkT_s} \left[\frac{1}{T} \sum_p \overline{G(f - \frac{p}{T_s})} \sum_m G(f - \frac{m}{T}) \mathrm{e}^{\mathrm{j}2\pi \frac{km}{\nu}} \right. \tag{4.25}$$
$$\left. + \frac{2N_0}{\mathcal{P}_\mathrm{d}} \sum_p |H_\mathrm{PF}(f - \frac{p}{T_s})|^2 \right]. \tag{4.26}$$

In the above equation the TF of the equaliser, i.e., $Q_{T_s}(f) = \sum_k q_k \mathrm{e}^{-\mathrm{j}2\pi fkT_s}$, appears at the right-hand side, but the expression inside the square brackets depends on the time index k. Let $\mathbb{Z}_\mu = \{k\nu + \mu : \ k \in \mathbb{Z}\}$ for $\mu = 0, \cdots, \nu - 1$. We can rewrite (4.25)

as

$$A(f) = \sum_{\mu=0}^{\nu-1} \sum_{l\in\mathbb{Z}_\mu} q_l \mathrm{e}^{-\mathrm{j}\,2\pi f l T_s} \left[\frac{1}{T} A(f) \sum_m G(f - \frac{m}{T}) \mathrm{e}^{\mathrm{j}\,2\pi \frac{m\mu}{\nu}} + \frac{2N_0}{\mathcal{P}_\mathrm{d}} \sum_p |H_{\mathrm{PF}}(f - \frac{p}{T_s})|^2 \right], \tag{4.27}$$

or, more concisely, as

$$A(f) = Q_0(f)B_0(f) + Q_1(f)B_1(f) + \cdots + Q_{\nu-1}(f)B_{\nu-1}(f), \tag{4.28}$$

where

$$A(f) = \sum_p \overline{G(f - \frac{p}{T_s})}, \tag{4.29}$$

$$Q_\mu(f) = \sum_{l\in\mathbb{Z}_\mu} q_l \mathrm{e}^{-\mathrm{j}\,2\pi f l T_s}, \tag{4.30}$$

$$B_\mu(f) = \frac{1}{T} A(f) \sum_m G(f - \frac{m}{T}) \mathrm{e}^{\mathrm{j}\,2\pi \frac{m\mu}{\nu}} + \frac{2N_0}{\mathcal{P}_\mathrm{d}} \sum_p |H_{\mathrm{PF}}(f - \frac{p}{T_s})|^2. \tag{4.31}$$

Assuming that $Q_\mu(f)$ are known for $\mu = 0, \cdots, \nu-1$, we could find $Q_{T_s}(f) = \sum_{\mu=0}^{\nu-1} Q_\mu(f)$. In order to find the MMSE solution, we use the ν-periodicity of the FS MMSE equaliser filter and the fact that, replacing kT_s by $(k-\eta)T_s$, $\eta = 0, \cdots, \nu-1$, in (4.15), is equivalent to introducing a delay by ηT_s to the channel. When a delay by ηT_s is introduced to the channel, the equaliser tap weights will be different from the previous one. Denoting them by q'_k, we have $q'_k = q_k \mathrm{e}^{\mathrm{j}\,2\pi\eta T_s f}$. Applying this modification will result in the following equations corresponding to (4.25)

$$\mathrm{e}^{\mathrm{j}\,2\pi\eta T_s f} A(f) = \sum_k q_k \mathrm{e}^{\mathrm{j}\,2\pi\eta T_s f} \mathrm{e}^{-\mathrm{j}\,2\pi f k T_s} \left[\frac{1}{T} A(f) \sum_m G(f - \frac{m}{T}) \mathrm{e}^{\mathrm{j}\,2\pi \frac{(k+\eta)m}{\nu}} \right. \tag{4.32}$$

$$\left. + \frac{2N_0}{\mathcal{P}_\mathrm{d}} \sum_p |H_{\mathrm{PF}}(f - \frac{p}{T_s})|^2 \right], \tag{4.33}$$

or

$$A(f) = \sum_k q_k \mathrm{e}^{-\mathrm{j}\,2\pi f k T_s} \left[\frac{1}{T} A(f) \sum_m G(f - \frac{m}{T}) \mathrm{e}^{\mathrm{j}\,2\pi \frac{(k+\eta)m}{\nu}} \right. \tag{4.34}$$

$$\left. + \frac{2N_0}{\mathcal{P}_\mathrm{d}} \sum_p |H_{\mathrm{PF}}(f - \frac{p}{T_s})|^2 \right]. \tag{4.35}$$

By substituting $\eta = 0, \cdots, \nu - 1$ in (4.34), and noting that $Q_\mu(f)$ is ν-periodic with respect to μ, we obtain the following equations corresponding to (4.28)

$$\begin{aligned} A(f) &= Q_0(f)B_0(f) + \cdots + Q_{\nu-1}(f)B_{\nu-1}(f), \\ A(f) &= Q_0(f)B_1(f) + \cdots + Q_{\nu-1}(f)B_0(f), \\ &\vdots \\ A(f) &= Q_0(f)B_{\nu-1}(f) + \cdots + Q_{\nu-1}(f)B_{\nu-2}(f). \end{aligned} \tag{4.36}$$

By adding these equations, we find that

$$Q_{T_s}(f) = \sum_{\mu=0}^{\nu-1} Q_\mu(f) = \nu A(f) \Big/ \sum_{\mu=0}^{\nu-1} B_\mu(f), \tag{4.37}$$

where

$$A(f) = \sum_p \overline{G(f - \frac{p}{T_s})}, \; G(f) = H_{\rm PR}(f)H_{\rm PF}(f), \tag{4.38}$$

$$B_\mu(f) = \frac{1}{T}A(f)\sum_m G(f - \frac{m}{T})\mathrm{e}^{\mathrm{j}2\pi\frac{\mu m}{\nu}} + \frac{1}{\mathcal{P}_{\rm d}}S_{z_k}(f), \tag{4.39}$$

and $\nu = T/T_s$. Note that:

1. In the above discussion we have assumed that the symbol timing error is zero. In order to see the effect of a nonzero symbol timing error, t_0, on the TF of the FS MMSE equaliser, we substitute $h(t)$ by $h(t - t_0)$ in (4.37)-(4.39). Then the TF of the equaliser with symbol timing error becomes

$$Q_{T_s}^{(t_0)}(f) = \nu \mathrm{e}^{\mathrm{j}2\pi f t_0} A(f) \Big/ \sum_{\mu=0}^{\nu-1} B_\mu^{(t_0)}(f), \tag{4.40}$$

   where

$$B_\mu^{(t_0)}(f) = \frac{1}{T}A(f)\sum_m G(f - \frac{m}{T})\mathrm{e}^{\mathrm{j}2\pi m(\frac{\mu}{\nu} + \frac{t_0}{T})} + \frac{1}{\mathcal{P}_{\rm d}}S_{z_k}(f), \tag{4.41}$$

2. In a T_s-spaced sampling receiver, there are $\nu = T/T_s$ samples within every time interval T at the output of the equaliser. A decision for the symbol transmitted

in that interval can be made based on any of these ν samples. The FS MMSE equaliser TF will depend on which sample is used for detection. All of these ν equaliser TFs can be obtained from (4.40) and (4.41) by letting $t_0 = \eta T/\nu$ for $\eta = 0, \cdots, \nu - 1$.

3. In the special case where $T_s = T$, $A(f)$ in (4.38) reduces to

$$A(f) = \sum_m \overline{G(f - \frac{m}{T})}, \tag{4.42}$$

which is the TF of a DT filter matched to the T-spaced sampled signal at the output of the C/D converter. Similarly, the denominator, $B(f)$, reduces to

$$B(f) = \frac{1}{T}\left|\sum_m G(f - \frac{m}{T})\right|^2 + \frac{2N_0}{\mathcal{P}_{\rm d}} \sum_m \left|H_{\rm PF}(f - \frac{m}{T})\right|^2. \tag{4.43}$$

Assuming that the transmit filter and the prefilter are the same and equal to a square root Nyquist filter [35], the equaliser TF takes the following famous form [105, 102]

$$Q_T(f) = \frac{\sum_m \overline{H(f - \frac{m}{T})}}{\frac{1}{T}\left|\sum_m H(f - \frac{m}{T})\right|^2 + \frac{2N_0}{\mathcal{P}_{\rm d}}}. \tag{4.44}$$

4. When $T_s = T/2$ and the channel bandwidth is less than or equal to $2/T$, the equaliser TF takes the form

$$Q_{T/2}(f) = \frac{\overline{G(f)}}{\frac{1}{T}|G(f)|^2 + \frac{2N_0}{\mathcal{P}_{\rm d}} \sum_m \left|H_{\rm PF}(f - \frac{2m}{T})\right|^2}. \tag{4.45}$$

It can be seen that, the SS equaliser (4.44) does not have control over the rolloff regions due to spectral folding, but the $T/2$-spaced equaliser (4.45) can invert the channel effects and/or the sampling phase errors over the whole bandwidth of the CT received signal. This can be seen by letting $2N_0 = 0$ in the two equations.

4.5 Spectral analysis of FS MMSE equalisers and the convergence of the FS LMS algorithm

In spite of the theoretical advantages of the MMSE receiver, its digital implementation using FS LMS algorithm can be problematic. Experimental measurements and simulated performance evaluations show that the tap-weight magnitudes of the FS TDL equaliser grow with iteration of the LMS algorithm [41]. The large tap-weight magnitudes can render the FS LMS algorithm non-convergent or unstable. Because, the FS LMS algorithm uses the noisy gradient instead of the true gradients [117, 102]. To describe the problem and find the possible reasons for large tap-weight magnitudes, we use the most common implementation of a digital MMSE receiver in which the sampling rate is twice the symbol rate, that is, $T = 2T_s$, and the pulse shaping filter and the receiver prefilter are the same and have square root raised cosine (SRRC) spectral characteristics with a rolloff factor $0 \leq \alpha \leq 1$ [147, 42, 105, 102]. We denote the TF of this filter by $p_{\text{srrc}}(t)$. The cascade of the transmit filter and the receiver prefilter has the raised cosine (RC) spectral characteristics, $p_{\text{rc}}(t) = p_{\text{srrc}}(t) * p_{\text{srrc}}(t)$. Under this model, the input to the equaliser is the sequence

$$r_{\text{PF}}(kT/2) = \sum_n \mathrm{d}_n g\left(kT/2 - nT\right) + z_k, \tag{4.46}$$

where $g(t) = h(t) * p_{\text{rc}}(t)$ and $z_k = z(t) * p_{\text{srrc}}(t)_{|_{t=kT/2}}$. There are two $T/2$-spaced MMSE equalisers according to whether odd indexed samples or even indexed samples at the output of the equaliser are used for detection. Assuming that the channel bandwidth is less than or equal to $2/T$, these two equalisers are given by

$$Q^e_{\frac{T}{2}}(f) = \frac{\overline{H(f)}}{\frac{1}{T}P_{\text{rc}}(f)|H(f)|^2 + \frac{2N_0}{\mathcal{P}_{\text{d}}}}, \text{ and} \tag{4.47}$$

$$Q^o_{\frac{T}{2}}(f) = \mathrm{e}^{\mathrm{j}\pi T f} Q^e_{\frac{T}{2}}(f). \tag{4.48}$$

To illustrate the magnitude responses of $Q^e_{\frac{T}{2}}(f)$ (and $Q^o_{\frac{T}{2}}(f)$) graphically, we assume that the channel is ideal, $h(t) = \delta(t)$. In this case, over the interval $[-1/T, 1/T]$ which

is one period of $Q^e_{\frac{T}{2}}(f)$,

$$Q^e_{\frac{T}{2}}(f) = \begin{cases} \dfrac{1}{\frac{1}{T}P_{\rm rc}(f) + \frac{2N_0}{\mathcal{P}_{\rm d}}}, & |f| < \frac{(1+\alpha)}{2T} \\ \text{indeterminate}, & \frac{1+\alpha}{2T} \leq |f| \leq \frac{1}{T}. \end{cases} \tag{4.49}$$

The magnitude response of the equaliser is shown in Fig. 4.2 (black curve). Since in the considered case the channel has RC spectral characteristics, the equaliser magnitude response looks like the reciprocal of the RC spectrum, but due to the additive noise its values at the band edges do not grow indefinitely (as they would do in the ZF equaliser).

As can be seen from Fig. 4.2 (the black curve corresponding to $t_0 = 0$), magnitude response of a FS MMSE equaliser with perfect symbol timing , even for an ideal channel, is large at band edges and the equaliser is indeterminate over some frequency bands.

In practice, where the receiver sampling clock is running independently from the transmitter and the channel is not ideal, (4.49) is not the optimum MMSE equalisers. The FS MMSE equaliser's TF, under the assumptions mentioned above, and in the presence of a symbol timing error, t_0, is given by

$$Q^e_{\frac{T}{2}}(f) = \begin{cases} \dfrac{1}{\frac{1}{T}\mathrm{e}^{\mathrm{j}2\pi t_0 f}P_{\rm rc}(f) + \frac{2N_0}{\mathcal{P}_{\rm d}}}, & |f| < \frac{(1+\alpha)}{2T} \\ \text{indeterminate}, & \frac{1+\alpha}{2T} \leq |f| \leq \frac{1}{T}. \end{cases} \tag{4.50}$$

The magnitude responses of the equaliser with various symbol timing errors are shown in Fig. 4.2. The FS MMSE equaliser compensates for the timing errors by increasing its magnitude responses around the rolloff region. This has consequences for the stability of the FS LMS algorithm discussed in Section 4.6.

For frequencies satisfying $(1 + \alpha)/2T < |f| < 1/T$ the equaliser TF is indeterminate. Actually, for MMSE equalization, the TF is not required to be determined over these intervals. Due to the matched filtering which is a part of the optimum equaliser' task, the input noisy signal is projected onto the subspace generated by the noise free received signal. Therefore, the relevant frequency band is the one over which the input signal's energy spectral density is nonzero. However, the indeterminacy or freedom of

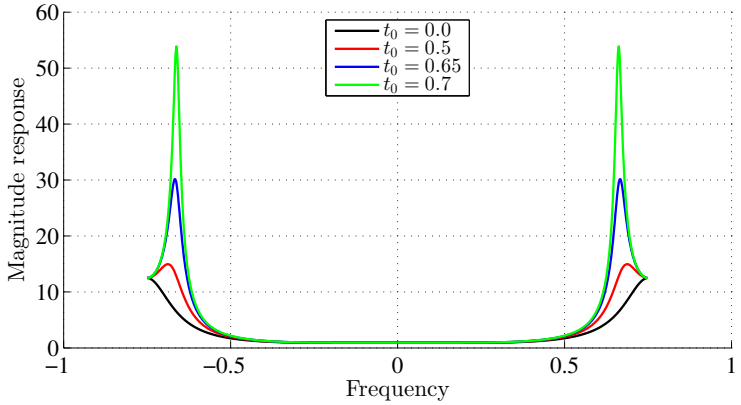

Figure 4.2: Magnitude response of the equaliser defined by (4.50) for various values of sampling phase, t_0, and with assumptions $T = 1$, $\mathcal{P}_{\rm d} = 1$, and $2N_0 = 0.04$ (SNR≈14 dB).

the equaliser TF over some frequency intervals can cause instability in implementation of the equaliser using the LMS algorithm. This is discussed in detail in Section 4.6.

When the input signal to the equaliser has frequency components outside the interval $[-(1+\alpha)/2T, (1+\alpha)/2T]$, due to time variation of the channel (Doppler spread) or carrier frequency error, these frequency components will excite the equaliser over their frequencies and the adaptive equaliser will adjust its tap weights to minimize the MSE error. Outside of the frequency band of the input signal there is no restriction on the equaliser TF except the initial conditions which are used at the start of the adaptation algorithm.

The effects of a FS equaliser's length on its stability and performance is an important issue when it is used for a channel with long delay spread like broadband channels [88]. In general, instability increases with increasing length of the equaliser. By reducing the length of an unstable equaliser, it can be made stable. In the limit, where the equaliser has only one tap, there is no instability problem but then the equaliser will perform as a memoryless threshold detector with an unacceptable MSE. The role of equaliser length on its behavior and performance deserves further explanation as it has significant consequences for the design of receivers for channels with large delay spread as in these channels the steady-state MSE of the equaliser increases when the equaliser is not sufficiently long. Some open questions regarding the effects of the FS equaliser length on its behavior have been described in [142]. The instability of longer FS equalisers, when the prefilter is the same as the transmit filter with some rolloff factor $\alpha \leq 1$, can be described as a result of large magnitude response of the

synthesized equaliser at some frequencies. Two possible reasons for larger magnitude response of the longer equalisers are 1) as described above, due to the sampling phase offset, the TF of the optimum $T/2$-spaced equaliser can have large magnitudes over the rolloff region. With increasing the $T/2$-spaced equaliser's length, its TF approaches the optimum values over the rolloff region, and hence its magnitude becomes large; 2) the equaliser TF is unconstrained over the frequencies $(1+\alpha)/2T < |f| < 1/T$. Over these intervals the values of the equaliser's TF is determined by constructive or deconstructive addition of various frequency domain harmonics noting that the TDL equalisers TF is a trigonometric polynomial. With increasing length of the equaliser, the number of participating harmonics in this build-up process grows and the possibility of constructive addition of a large number of harmonics increases. As a result, the magnitudes of some equaliser tap weights can grow large. In turn, successive approximations of the optimum equaliser tap weights, provided by iteration of the LMS algorithm, and hence the equaliser norm also increase. Note that this is different from the explanation of the phenomenon given in [41, 105, 102]. This resolves the inconsistency problem between the theory and practice of FS MMSE equalization highlighted in [142].

In digital implementation of the MMSE receiver, the matched filter and the T-spaced TDL equaliser filter are combined together and the resulting T_s-spaced TDL equaliser is responsible for performing their functions [42, 105]. The possibility of matched filtering using a DT filter depends on the spectral characteristics of the additive noise [154]. In particular, when the PSD of the noise is not strictly positive, the matched filter is not defined. In [29], projected matched filtering is used when the noise PSD is not strictly positive. When the noise PSD is not bounded away from zero the matched filter might be unstable. To avoid these problems the front-end C/D converter should be designed properly. Improper choice of the front-end C/D converter can result in a malfunctioning adaptive equaliser. This can be seen through divergence of the tap-weight adaptation algorithm or by an indefinite increase of the equaliser tap weight magnitudes. The latter can in turn result in an unstable equaliser. The leaky LMS algorithm [41] or its variants [128, 61, 148, 92] are usually applied to avoid this instability. Using this algorithm imposes a complexity cost and violates the optimality of the receiver as the residual MSE increases when the algorithm is applied [148] and the

obtained estimate is biased [117]. By characterizing the sources of these problems and designing the front-end processing properly, they can be avoided without additional complexity or performance degradation caused by the leaky LMS algorithm.

4.6 Stabilizing FS LMS algorithm

The LMS algorithm is a simple iterative procedure to approximate the optimum MMSE equaliser by a finite-length TDL filter [102]. The algorithm starts with a given initial-state vector $\mathbf{q}_0$ (usually $\mathbf{q}_0 = \mathbf{0}$) and updates the equaliser tap weight vector according to a recursion formula given by [102, 117]

$$\mathbf{q}_{k+1} = \mathbf{q}_k + \Delta(\mathrm{d}_k - \hat{\mathrm{d}}_k)\overline{\mathbf{r}_{\mathrm{PF}}},\ k \geq 0, \tag{4.51}$$

where $\mathbf{q}_k$ is the tap weight vector after the kth iteration, Δ is the step size, and $\mathbf{r}_{\mathrm{PF}}$ is the input vector to the equaliser at the kth iteration. In its kth iteration, the estimated noisy negative gradient vector, $(\mathrm{d}_k - \hat{\mathrm{d}}_k)\overline{\mathbf{r}_{\mathrm{PF}}}$, is used as an unbiased estimate of the true negative gradient vector of the quadratic MSE surface given by

$$\nabla J_{\mathrm{MSE}}(\mathbf{q})_{|\mathbf{q}=\mathbf{q}_k} = \mathrm{E}[(\mathrm{d}_k - \hat{\mathrm{d}}_k)\overline{\mathbf{r}_{\mathrm{PF}}}]. \tag{4.52}$$

Due to application of the noisy gradient vector, the LMS algorithm will not converge to a steady state if it is not sufficiently robust against perturbations.

For SS adaptive MMSE equalisers, the LMS algorithm is convergent in the mean if $0 < \Delta < 2/\lambda_{\max}$, where $\lambda_{\max}$ is the largest eigenvalue of the correlation matrix of the SS input signal to the equaliser [102]. With this choice of Δ, the speed of convergence of the algorithm depends on the smallest eigenvalue, $\lambda_{\min}$, of the input correlation matrix [102]. The correlation matrix of SS samples of the received signal is strictly positive definite [102], and according to (4.9), its smallest eigenvalue is larger than or equal to the additive noise PSD, $2N_0$. Convergence of the sequence $\{\mathbf{q}_k\}_{k=0}^{\infty}$ to steady state and stability of the LMS algorithm under perturbations depends on the choice of the step size and the condition number $\rho = \lambda_{\max}/\lambda_{\min}$ of the input signal's correlation matrix [158, 117, 102].

The statistical properties of the FS sampled received signal are different from the SS sampled signal in that, it is not a WSS process, but a WSCS process [36, 38, 149]. As a result, the optimum FS MMSE equaliser solution (4.47), and the convergence of the sequence of tap weight vectors obtained by iteration of the FS LMS algorithm to the optimum solution depend on the sampling phase. This is because the correlation matrix of the FS samples of the received prefiltered signal $r_{\mathrm{PF}}(t)$ is Hermitian semi-positive definite, but not Toeplitz [41, 105]. In the following, we will use the explicit TF of the FS MMSE equaliser, given by (4.47), instead of using the correlation matrix of the input samples.

When the sampling interval, T_s, is an integer fraction of the symbol interval, i.e., $T = \nu T_s$, for some $\nu \in \mathbb{N}$, the equaliser's TF will be a periodically time-varying filter with period T. Since the tap spacing of the TDL equaliser is T_s, it will be time varying if the observation instants are T_s-spaced rather than T-spaced. Due to time dependence of the TF, the convergence and stability of the equaliser depends on the observation instants, or equivalently, on the sampling phases at the receiver front end (C/D converter) and the equaliser output.

When the equaliser TDL filter is finite length, its frequency response is only conditioned over the interval $|f| < (1+\alpha)/2T$, and therefore, depending on the channel characteristics, it can have large magnitudes over indeterminate intervals characterized by $(1+\alpha)/2T \leq |f| < 1/T$. A natural approach in order to condition the TF over indeterminate intervals is to force the frequency response to be zero over those intervals. In practice, the leaky LMS algorithm is commonly used to do the job. But the leaky LMS algorithm has disadvantages as described in Section 4.1, and it cannot always stabilize an unstable LMS algorithm. In short, the solution obtained using the leaky LMS algorithm is different from the optimum solution over the interval $|f| \leq (1+\alpha)/2T$, is zero over the intervals $(1+\alpha)/2T < |f| < T/2$ and, more importantly, it has jump discontinuities at boundaries, $f = \pm(1+\alpha)/2T$. The jump discontinuities cannot be properly approximated using finite Fourier series and Gibbs' overshooting phenomenon occurs at discontinuities [98] and cannot be avoided by increasing the filter length.

In the following, we propose a simple approach to regularize the FS MMSE equaliser that avoids the disadvantages of the leaky LMS algorithm and performs

significantly better. This approach retains the theoretical advantages of CT MMSE equalization in digital implementation without extra cost. This is done by modifying the prefilter in order to preserve the regularizing effect of the additive noise. Assume that the prefilter is not the same as the transmit pulse shaping filter, but a filter, $h_{\mathrm{PF}}(t)$, with a wider bandwidth such that the PSD of the sampled noise at its output is bounded away from zero. The PSD of the sampled noise, given by (4.11), is bounded away from zero if there is an $\varepsilon > 0$ such that

$$\Phi_{h_{\mathrm{PF}}}^{T/2}(f) = \sum_k \left| H_{\mathrm{PF}}(f - \frac{k}{T_s}) \right|^2 > \varepsilon \quad \forall f. \tag{4.53}$$

This will happen if the passband of the prefilter includes the interval $|f| \leq 1/T$.

Using such a prefilter, the denominator of the infinite-length equaliser TF, defined by (4.47), will be nonzero over all frequencies. Therefore, the TF values over the indeterminate region will be zero and the transition from the nonzero spectrum to zero spectrum will be smooth.

A variety of filters can be used as a prefilter in order to regularize the FS MMSE equaliser. In summary, a preferred prefilter has the following properties:

1. it is realizable,
2. its bandwidth is wide enough to pass noise over the band $[-1/T, 1/T]$,
3. time shifts of its IR, i.e., the set $\{h_{\mathrm{PF}}(t - k/2T)\}$ form an orthonormal set.

The third property is not necessary, but advisable. When the shifts are not orthonormal, the spectral characteristics of the sampled noise will be different from the input noise to the prefilter. Since the FS MMSE equaliser performs matched filtering, the modifications caused by the prefilter will be reversed by the equaliser, which is an extra job imposed on the equaliser.

A suitably realizable prefilter can be chosen in a variety of ways. For example, the filters obtained by dilating the SRRC pulse used for pulse shaping, or by increasing the rolloff factor of the prefilter to more than one, in such a way that the spectra of the $1/2T$ frequency shifted pulses overlap with each other can be used. Then, the sampled noise PSD satisfies (4.53). Increasing the rolloff factor of the SRRC pulse to more than

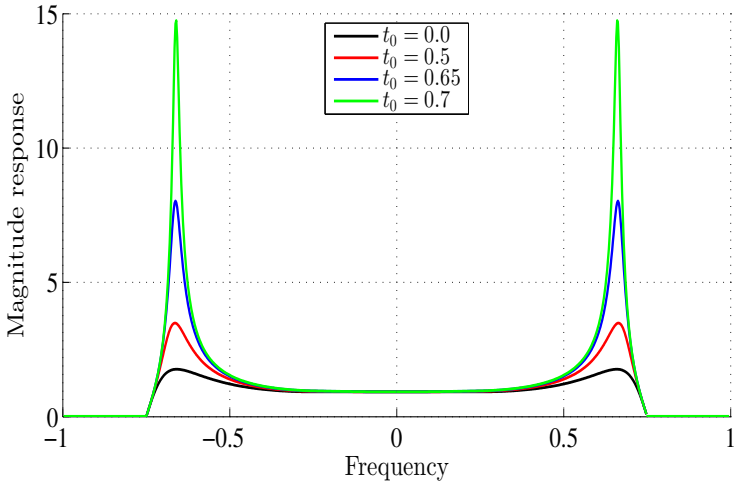

Figure 4.3: Magnitude responses of FS MMSE equalisers, when a dilated prefilter is employed, corresponding to those shown in Fig. 4.2, for various values of sampling time error, t_0, under the assumptions $T = 1$, $\mathcal{P}_{\rm d} = 1$, and $2N_0 = 0.04$ (SNR=14 dB).

one destroys the orthogonality of its time shifts and therefore, a dilated filter which preserves the orthogonality property is preferred. Alternatively, a SRRC filter with small rolloff factor but wider bandwidth can be used.

The effects of using the dilated SRRC as a prefilter on TF of the FS equaliser, is demonstrated in Fig. 4.3, where we have plotted the magnitude responses for various sampling time errors. In this figure, we have plotted the magnitude responses of the equaliser when the prefilter's IR is a dilated version of the pulse shape, that is, $h_{\rm PF}(t) = \sqrt{2}p_{\rm srrc}(2t)$. A comparison with Fig. 4.2 shows the effect of a dilated prefilter on the magnitude responses of the equalisers when there are sampling phase errors. The dilated prefilter has two effects: 1) it forces the magnitude responses to be zero over indeterminate intervals, 2) it reduces the magnitude responses over the rolloff region resulting a more stable equaliser.

4.7 Simulations

In this section, the effectiveness of the proposed method on stabilizing the LMS algorithm is demonstrated by simulations. For this purpose, we consider TDL channel models whose tap spacings are integer multiples of the symbol interval T. We use two channels, titled Ch1 and Ch2, with power delay profiles and magnitude responses shown in Fig. 4.4.

Ch1 is a typical of a good quality telephone channel [102, Fig. 9.4-5a] and Ch2 is representative of a bad quality channel, typical of a broadband channel. Ch2 is a SS discretised version of a realization of an ultrawideband channel model [88]. Ultrawideband channels consist of one or several clusters of multipath components and are usually highly frequency selective. As can be seen from Fig. 4.4, at some frequencies, the magnitude response of channel Ch2 is small. This kind of channel has large eigenvalue spreads and therefore, the steady-state MSE of the equaliser, using the LMS algorithm, applied to them is comparatively larger than for good quality channels like Ch1.

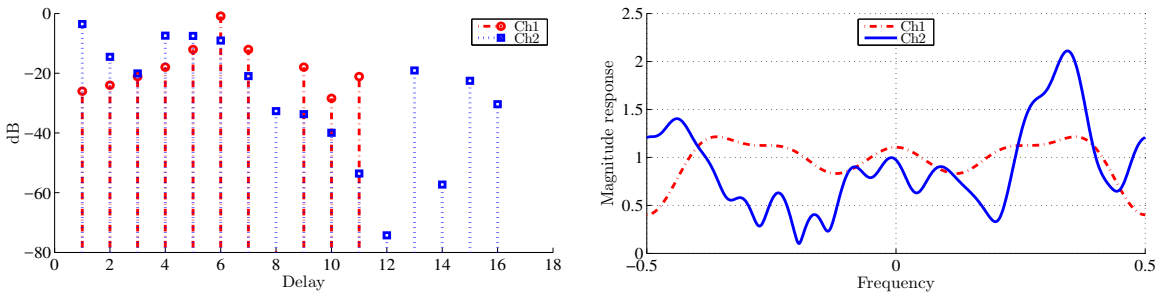

Figure 4.4: PDPs (left) and magnitude responses (right) of Ch1 and Ch2. The delay scale of the PDPs is equal to the symbol interval T. Both channels IRs are normalized to have unit energy.

The complex lowpass transmit signal $s(t)$ is given by (4.1), where the sequence of complex symbols are chosen from the 4-QAM constellation points $\{\frac{1}{\sqrt{2}}(\pm 1 \pm \mathrm{j})\}$.The modulation order does not affect the presented learning curves or the norm curves, because the mean square errors are calculated using error magnitude and the pulse energy and variance of the transmit symbols are normalised. The transmit pulse shape has SRRC spectral characteristics and is normalized to unit energy. The rolloff factor of the transmit pulse is $\alpha = 1/3$. The time span of the pulse is $10T$. For transmission, the complex baseband signal $s(t)$ is upconverted to a real bandpass signal $s_c(t) = 2\mathrm{Re}\{s(t)\mathrm{e}^{\mathrm{j}2\pi f_c t}\}$, where $f_c = 50/T$. That is, the fractional bandwidth of the system is about 2.67%.

In order to simulate a realistic CT waveform channel and noise, the channel IR is upsampled to 300 samples per symbol interval. The noise-free received signal, $u(t)$, is obtained by convolving the upsampled channel IR with $s_c(t)$. Then real-valued white Gaussian noise samples with standard deviation σ are generated and added to the noise-free signal to obtain the real bandpass received signal $r_c(t) = u(t) + z(t)$. At

the receiver, the signal $r_c(t)$ is frequency-shifted through multiplication by $\mathrm{e}^{-\mathrm{j}\,2\pi f_c t}$. It is assumed that the carrier frequency is provided by a carrier synchronization system [77]. In practice, frequency down conversion is usually accomplished by extracting the in-phase and quadrature components of $r_c(t)$ which is equivalent to what we have simulated.

The receiver front end consists of a prefilter which suppresses the channel noise and removes the double-frequency component of $r_c(t)\mathrm{e}^{-\mathrm{j}\,2\pi f_c t}$. In simulations, four different prefilters were used. Each prefilter is obtained from the SRRC filter by dilation. That is, for δ=1, 3/2, 2, 3, $D_\delta p_{\mathrm{srrc}}(t) \triangleq \sqrt{\delta} p_{\mathrm{srrc}}(\delta t)$. Both T-spaced and $T/2$-spaced equalisers use the LMS algorithm in order to adjust the equaliser tap weights.

Two graphical methods are used to demonstrate the performance of each design and the evolution of the tap weights of the equalisers. The first one is the so-called MSE learning curve [47, 117] which is a function of the iteration number of the LMS algorithm and is obtained by averaging the squares of the error magnitudes at the ith iteration of the LMS algorithm for several realization of the algorithm. Each realization corresponds to one training period. In order to obtain the learning curves in the simulations, a sequence of known, but random, symbols $\{\mathrm{d}_{i,k}\}_{i=1}^{I}$ at the kth realization (training) are generated at the transmitter and transmitted through the channel. The T-spaced samples of the equaliser output, $\{\hat{\mathrm{d}}_{i,k}\}_{i=1}^{I}$, are compared with the transmitted symbols. This process is repeated several times (the number of realizations M_r) and finally, for each i, the squared error magnitudes are averaged over all realizations. That is, the learning curves are obtained by the formula

$$LC(i) = \frac{1}{M_r} \sum_{k=1}^{M_r} |\mathrm{d}_{i,k} - \hat{\mathrm{d}}_{i,k}|^2, \;\; i = 1, \cdots, I. \tag{4.54}$$

The second measure of performance is the equaliser norm. At the ith iteration of the LMS algorithm at the kth realization (training), the equaliser's transient state is given by the equaliser tap-weight vector $\mathbf{q}_{i,k} = (q_{i,k,-L}, \cdots, q_{i,k,L})$. The corresponding transient tap-weight vector norm is $\|\mathbf{q}_{i,k}\|_2 = (\sum_l |q_{i,k,l}|^2)^{1/2}$. The norm curves are

obtained by averaging $\|\mathbf{q}_{i,k}\|_2$ over the realization index k:

$$NC(i) = \frac{1}{M_r} \sum_k \|\mathbf{q}_{i,k}\|_2, \ i = 1, \cdots, I. \tag{4.55}$$

The ensemble-averaged equaliser norm (4.55) is the appropriate measure to study the equaliser's tap weight behaviour. It is equal to the largest eigenvalue of the equaliser. Also, it is an upper bound on the tap weights. A small value of the equaliser norm guarantees its stability against perturbation. This can be seen by the fact that [114]

$$\|\mathbf{q}_i\|_2 = \sup_{\mathbf{x}} \frac{\sum_{l=-L}^{L} x_l \overline{q_{i,l}}}{\|\mathbf{x}\|_2}, \tag{4.56}$$

where the supremum is over all nonzero complex vectors of length L; $\mathbf{x} = (x_{-L}, \cdots, x_L)$. The numerator in (4.56) is the equaliser output when the input vector is $\mathbf{x}$. When the equaliser norm at its transient or steady state is large, a small perturbation in the input, due to the channel variations or the noisy gradient, can cause large deviations at the output and, because of that, the equaliser may lose track and drift away from the optimum solution. Also, an equaliser with large norm means that some of the equaliser tap weights are large. In practice, large tap weights can saturate some of the finite-memory registers in the receiver which can have a disastrous effect on performance [40, 143].

The advantage of using the norm curves is that the behaviour of the tap weight magnitudes and the equaliser eigenvalues can be observed from the norm curves. This is not possible using the corresponding learning curves. A learning curve describes the average performance of the equaliser, not the sources of its misbehaviour. It is also important to know how much power the equaliser is spending on reducing the average error and whether the increasing MSE is due to saturation of the registers or the algorithm's intrinsic instability.

The SS TDL model for the real physical channel is a rough model. In reality, the channel taps corresponding to multipath components are not equidistant. According to sampling and basis expansion models [59, 9, 77], a mathematically exact channel model has fractional tap spacing and infinite length. Due to this, the performance of

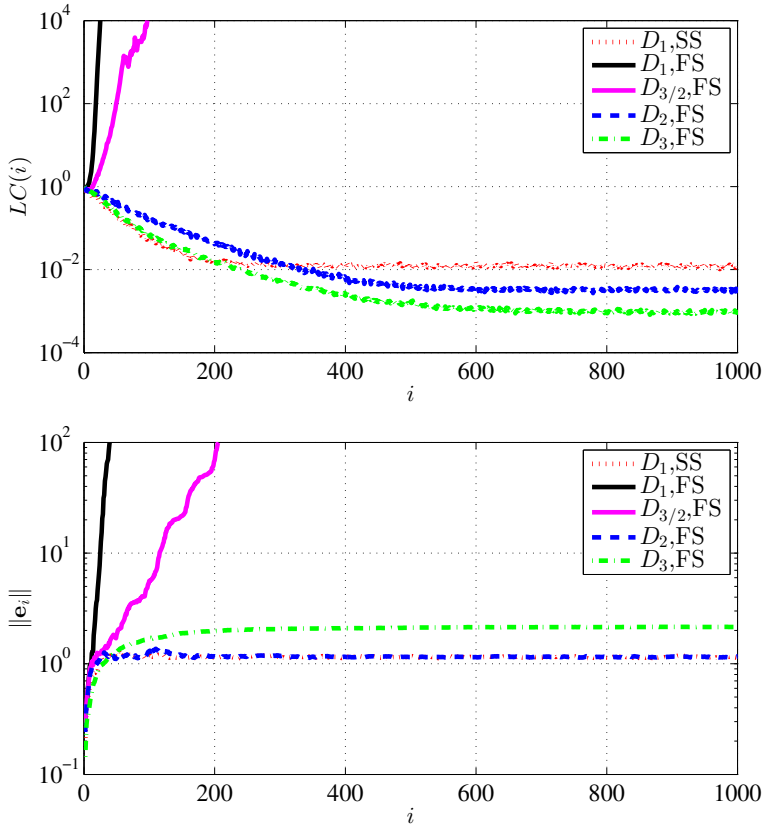

Figure 4.5: Learning (top) and norm (bottom) curves of the LMS algorithm for SS and FS sampled signals. The simulated channel is Ch1. Simulation parameters are $\Delta = 0.08$, $2N_0 = 0.04$ and SNR = 14 dB.

the SS equalisers applied to a real physical channel will be between the best and the worst simulated performances corresponding to the best and worst sampling phases. FS equalisers which are sufficiently long can compensate for sampling phase offsets by adjusting the tap weights, but SS equalisers cannot.

In all simulations presented in this section, the equaliser time duration is twice the delay spread of the channel. Therefore, the number of taps of the SS equaliser is twice the number of taps of the channel, and for FS equalisers the number of the taps are four times the number of taps of the channel.

Fig. 4.5 shows the learning curves (left) and the norm curves (right) corresponding to five equalisers for Ch1. The curves denoted by D_1,SS correspond to a receiver with the front-end filter the same as the transmit filter followed by SS sampling. The samples are input to a SS MMSE equaliser which employs the LMS algorithm to adjust equaliser tap weights and the sampling time offset is $t_0 = 0$ (perfect sampling time). The other curves, each denoted by D_δ,FS, with δ=1, 2/3, 2, 3, correspond to receivers with normalized dilated prefilters defined by $p_\delta(t) = \sqrt{\delta}p(\delta t)$ followed by $T/2$-spaced

sampling. In each case, the samples are input to a $T/2$-spaced MMSE equaliser which employs the conventional LMS algorithm. The time span of all equalisers in Fig. 4.5 is twice the delay spread of the channel. The step size for all equalisers is $\Delta = 0.08$. The FS equaliser with prefilter matched to the transmit filter (D_1,FS) is extremely unstable as can be seen from the corresponding norm curve in Fig. 4.5. In this case the equaliser norm and the MSE increase exponentially with the iteration index, i, of the LMS algorithm. The steady-state MSE of the FS receivers with prefilters $\sqrt{2}p(2t)$ and $\sqrt{3}p(3t)$ are lower than the SS equaliser with perfect symbol timing. The performance of these FS equalisers are insensitive to sampling phases.

The receiver with prefilter $\sqrt{3/2}\,p_{\text{srrc}}(3t/2)$ is also unstable, but the rate of increase of its learning and norm curves is lower than D_1,SS. By decreasing the step size Δ to less than 0.06 it can be stabilized. We intentionally did not do that in producing the figures to show that the instability of the FS LMS algorithm is not solely because of the indeterminacy of the equaliser over some frequencies as described in [41]. The SRRC pulse has rolloff factor 1/3 and therefore, the passband of the dilated pulse $\sqrt{3/2}\,p_{\text{srrc}}(3t/2)$ is equal to the whole frequency interval $(-1/T, 1/T)$. Therefore, the equaliser TF vanishes outside of the frequency band of the noise-free received signal. This shows that, this misbehaviour of the LMS algorithm, compared to the other cases with dilated prefilters, is due to the large magnitude response of the optimum MMSE equaliser over the rolloff region of the pulse and not due to the indeterminacy of the TF over some frequencies.

Next we repeat the simulation for Ch2. By using the same parameters as before, all equalisers are divergent (unstable) except the one denoted by D_3-FS, which preserves its performance. However, due to frequency selectivity of Ch2, the steady-state MSE is much higher than what is shown in Fig. 4.5 (about 0.1). To compare the relative sensitivity of different designs, we decreased the step size to 0.029. The resulting learning and norm curves are shown in Fig. 4.6. The figure shows that by increasing the dilation factor stability improves and the steady-state MSE decreases. Even with dilation factor $\delta = 3$, the MSE is below the case of SS equaliser with perfect sampling phase.

Finally, we compare the performance of the leaky LMS algorithm with the method

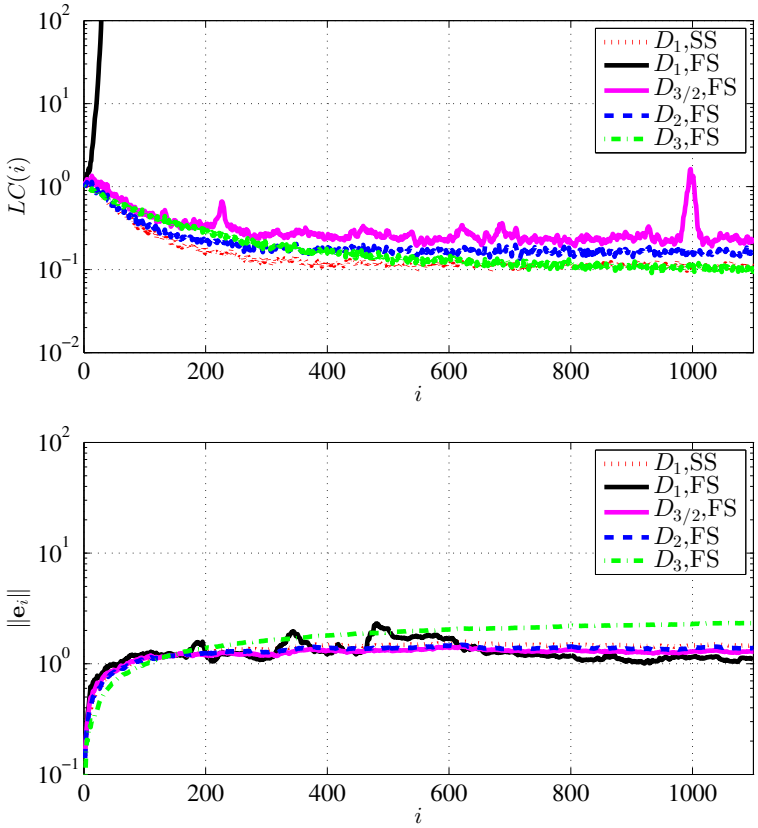

Figure 4.6: Learning (top) and norm (bottom) curves of the LMS algorithm for SS and FS sampled signals. The simulated channel is Ch2. Simulation parameters are $\Delta = 0.029$, $2N_0 = 0.04$ and SNR $= 14$.

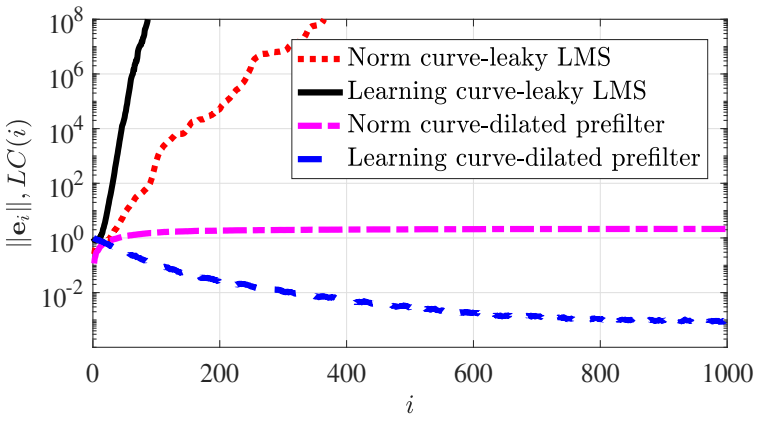

Figure 4.7: Comparison with the leaky LMS algorithm. The simulated channel is Ch1. Simulation parameters are $\Delta = 0.06$, $\mu = 0.1$, $2N_0 = 0.04$ and SNR $= 14$ dB.

presented in this section. To this end, we use the same channel and parameters as Fig. 4.5, in conjunction with the leaky LMS algorithm. Using the dilated prefilters in the receiver stabilizes the norm curves and decreases the steady-state MSE as shown in Fig. 4.5. The use of the leaky LMS algorithm with the same step size $\Delta = 0.08$ as before, and various tap-leakage parameters $0 < \mu < 1$ does not stabilize the norm curve and hence, the learning curve is increasing (with some random oscillations) during the

training period of 1000 symbols. Increasing the tap-leakage parameter does not solve the problem. For sufficiently small step sizes (e.g., $\Delta < 0.008$) the leaky LMS algorithm becomes stable but, with such small step sizes the LMS algorithm is stable without using tap leakage. Also, with a smaller step size, i.e. when $\Delta = 0.06$, we tried to stabilize the algorithm by increasing the tap-leakage parameter from zero to one, but the learning curve remained above one. In Fig. 4.7, the norm curve and the learning curve obtained by using the parameter values $\Delta = 0.06$ and $\mu = 0.1$ are shown. The simulation shows the failure of the leaky LMS algorithm to achieve an acceptable MSE level for the channel and parameters used in simulation. The norm and learning curves of the equaliser with dilated prefilter $\sqrt{3}\,p_{\text{srrc}}(3t)$ is stable and its steady-state MSE is less than 0.001.

4.8 Conclusion

This chapter studies spectral characteristics of the FS MMSE equaliser and the stability of the LMS algorithm. The TF of the FS MMSE equaliser is derived including the effects of the front-end receiver C/D converter and the sampling phase. It is a periodically time-varying function of the frequency. Using the explicit TF, the sources of instability and non-convergence of the LMS algorithm are characterized. It is shown that the large magnitude response of the FS MMSE equaliser over the transition band of the employed transmit pulse is a major source of instability along with the indeterminacy of the TF over frequencies outside the spectrum of the received signal. It is explained how the magnitude response over the transition frequency band depends on the sampling phase of the received signal. For equalizing highly frequency selective channels that have long delay spread, such as broadband channels, the LMS algorithm can be extremely unstable and to guarantee its stability small step sizes are required. Using small step sizes reduces the learning speed of the LMS algorithm. Lower learning speed means longer training period and inferior tracking capability. To remedy this problem we proposed using a wider bandwidth prefilter before sampling at the receiver in such a way that the folding spectrum, caused by sampling, has overlaps over the transition band. Using such a prefilter automatically decreases the magnitude response of the equaliser synthesized by the repetition of the FS LMS algorithm. This approach

does not have any extra computational cost and performs better than the leaky LMS algorithm. Simulations showed the effectiveness of the proposed approach.

Chapter 5

Conclusion

5.1 Summary

In Chapter 2, we derived a mathematical expression for the lowpass received signal from a wireless channel which includes the frequency dependent effects of the channel. Using this expression, we determined the characteristics of a front-end receiver C/D converter including a realisable lowpass filter, and the lowest sampling rate with the property that its output provides a sufficient statistic for any optimum receiver. A DT TDL channel model with tap spacing equal to a fraction of the symbol interval is derived.

In Chapter 3, we analysed the interactions of UWB pulses with building walls. Single-layer walls create several distorted pulses when illuminated by UWB pulses. The distortion of individual pulses due to frequency dependence of parameters of typical building materials is not the major source of distortion. The major source of distortion is IPI which occurs when the reflected/transmitted pulses partially overlap. A method for derivation of the PDPs of wall reflection and transmission is introduced using the MCCs which incorporates pulse distortion as a power loss. The derived PDPs include the overall effect of wall transmissions and reflections. Excluding the first reflected pulse, the PDPs of reflections from and transmissions through single-layer walls are exponential. For multilayer walls, or combinations of multiple reflections and transmissions, the PDP is not exponential. Their PDPs are the convolutions of several exponential PDPs. The PDP derivation of this chapter describes the multicluster structure of the UWB channel models obtained by measurements. The approach can

be used in deterministic and statistical modelling of UWB channels.

The experimental approach for model derivation for channels with large absolute bandwidths is expensive and time consuming. Chapter 3 introduces a new theoretical approach for derivation of the TDL models and PDPs for multilayer building structures. Overall channel effects are determined by objects in the environment and their dynamics. Therefore, characterisation of the effects of the channel *constituents* is important and can be used to to find suitable channel models.

In Chapter 4, we studied spectral characteristics of the FS MMSE equaliser and the stability of the LMS algorithm. The TF of the FS MMSE equaliser is derived including the effects of the front-end receiver C/D converter and the sampling phase. It is a periodically time-varying function of the frequency. Using the explicit TF, the sources of instability and non-convergence of the LMS algorithm are characterized. It is shown that the large magnitude response of the FS MMSE equaliser over the transition band of the employed transmit pulse is a major source of instability along with the indeterminacy of the TF over frequencies outside of the spectrum of the received signal. It is shown that the magnitude response over the transition frequency band depends on the sampling phase of the received signal. For equalizing highly frequency selective channels that have long delay spread, such as broadband channels, the LMS algorithm can be extremely unstable and to guarantee its stability small step sizes are required. Using small step sizes reduces the learning speed of the LMS algorithm. Lower learning speed means longer training periods and inferior tracking capability. To remedy this problem we proposed the use of a prefilter before sampling at the receiver which has wider bandwidth in a way that the folding spectrum, caused by sampling, has overlaps over the transition band. Using such a prefilter automatically decreases the magnitude response of the equaliser synthesized by the repetition of the FS LMS algorithm. This approach does not have any extra computational cost and performs better than the leaky LMS algorithm. The effectiveness of the proposed approach is demonstrated by simulations.

While the celebrated LMS algorithm has many advantages, it is not widely used due to its instability and sensitivity. The characterisation of the FS MMSE equaliser provides new insights on behaviour of the LMS algorithm and the stabilisation method

proposed can be employed in designing low-cost linear equalisers for future single carrier broadband systems.

The following sections include some applications and possible extensions of the results summarised above.

5.2 Directions for Further Research

The work of this thesis can be continued is several directions. The followings are the most interesting directions due to the emerging developments in 5G systems using BB signals.

5.2.1 From deterministic to stochastic channel model

In Chapter 2 a deterministic CT baseband model for a generic broadband channel presented that includes major effects of a broadband channel. Then, a DT channel model derived which is *realisable* and captures all characteristics of the CT model. The results of Chapter 2 can be combined with the approach used in Chapter 3 to find a theoretical model for BB channels.

In a deterministic channel model the channel parameters depend deterministically on the geometrical and physical properties of the communication environment. For communication system design, its mathematical analysis and performance evaluations a statistical model is required.

Usually, the stochastic channel models are derived using experimental measurements. Behind all standard channel models there are measurement results supporting the validity of the model for particular communication environments. This is a general approach for model derivation which is common in all branches of science and engineering. For wireless communication channel modelling there is another approach which complements the experimental model. After all, in any wireless communication channel, messages are transmitted by using electromagnetic or acoustic waves. There are physical theories describing the propagation of these waves and their interactions with objects in the environment. Maxwell's equations describe all electromagnetic phenomena, but in many practical situations, where there are interacting objects with

complicated geometries and material characteristics, determining the boundary conditions and finding the solutions of these equation are not possible. In fact, there is no tractable unified theory describing all interactions of electromagnetic waves with objects in the environment.

In spite of difficulty of solving Maxwell's equations in general, some experimental observations of the electromagnetic propagation phenomena can be explained much easier than others by using principles of electromagnetics. In Chapter 3 we use this method to describe the main source of clustering phenomena observed mainly in indoor channels. This approach can be extended to include other effects of communication channels such as diffraction and scattering.

In BB channels, due to the frequency dependency of diffraction and scattering, the pulses diffracted or scattered by objects in the environment will be distorted.[1] Therefore, diffraction and scattering can also be approximately modelled as TDL filters. Doing this, each path of a multipath channel can be modelled as a cascade of TDL filters. We did this for a multilayer wall in Examples 3.7.1 and 3.7.2 for multilayer walls. Then statistical models for dense multipath channel models can be derived mathematically. A possible approach is explained in Section 3.7.

5.2.2 Equalisation for faster than Nyquist signalling systems

Faster-than-Nyquist (FTN) signalling systems modulate and transmit information symbols in a rate higher than the Nyquist rate of the channel. Nyquist rate is the maximum rate that the symbols can be transmitted through an ideal AWGN channel without ISI [102]. In a system with a given bandwidth W, the Nyquist rate is W. Therefore, transmitting symbols at any rate higher than W will introduce unavoidable ISI at the transmitter. In addition to this, the frequency-selective channel also introduces ISI. In 1975, Mazo [71] studied the possibility of FTN signalling and proved that in an ideal AWGN channel it is possible to increase the transmission rate up to 25% without decreasing the minimum Euclidean distance [71, 8] between two distinct received symbols. That is, by introducing ISI at the transmitter the bandwidth efficiency of the system can be increase by 25%. Due to demand for higher bandwidth efficiency, recently, FTN

[1] However, the distortions caused by diffraction and scattering tend to be diffuse.

signalling has received increasing research interest[2]. Following this line of research and considering the FS MMSE equaliser's TF given in (4.37)-(4.39), it can be seen by some manipulation of the formula for special values of ν that, the FS MMSE equaliser is capable of equalising the ISIs introduced by FTN signalling and the channel. It can be shown that, theoretically the signalling rate can be increased and still it is possible to design realisable low complexity linear equalisers to remove the intentional and channel introduced ISI. With increasing signalling rate, the complexity of the receiver increases. Increasing complexity limits the signalling rate in practice. This is a follow up research to the results presented in Chapter 4 and [91]. This approach can be extended to the case of OFDM systems where each sub-carrier can be fed with symbol streams at rates higher than Nyquist rate of the corresponding sub-channel. The corresponding OFDM receiver is more complex than the conventional OFDM receiver in that, each sub-carrier requires a simple short length equaliser after performing FFT at the receiver.

[2]A search for the keyword "Faster than Nyquist" in IEEExplore resulted in 35 articles and book chapters published from January to September 2017.

Appendices

Appendix A

Modelling Activities for UWB and mm-Wave Channels

Due to the large bandwidth of BB signals, characterisation of propagation channel models for these signals requires more parameters. In general, channel models for BB communication systems are more complicated than the channel models for NB systems.

Most channel models proposed in the literature are mainly based on experimental measurements. In this thesis, we emphasised the importance and usefulness of the physics-based mathematical channel models in Chapters 2 and 3. For readers' convenience we provide some important references for various experimental models for UWB and mm-wave channels.

Since the advent of UWB communications one of the main challenges was finding suitable channel models for these systems. A lot of experimental measurements have been undertaken since the first measurement results reported in [160]. The results of all measurements were analysed and compiled in a report [33] by the channel modelling subcommittee of the IEEE 802.15.3a working group in 2003. Later, a reference UWB channel model was released for indoor high data rate UWB applications known as IEEE 802.15.3a channel model. In 2004, another UWB channel model for low data rate UWB application was released which is referred to as IEEE 802.15.4a standard channel model [55, 88]. Models for various frequency ranges and environments are provided in [55]. There, also MATLAB programs and numerical values for 100 impulse response realisations in each environment are provided. IEEE 802.15.4a includes all scenarios already considered in IEEE 802.15.3a and therefore it is the most comprehensive reference for UWB channel models.

Pathloss models for UWB systems are different from NB models. In UWB channel

models pathloss is frequency dependent. In [55], a method for calculation of pathloss is recommended. The frequency-dependent pathloss is defined by

$$PL(f,d) = \mathrm{E}\left[\int_{f-\Delta f/2}^{f+\Delta f/2} |H(\tilde{f},d)|^2 \,\mathrm{d}\tilde{f}\right], \tag{A.1}$$

where $H(\tilde{f},d)$ is the TF from antenna connector to antenna connector, and Δf is chosen small enough so that diffraction coefficients, dielectric constants, etc., can be considered constant within that bandwidth. Then , the total pathloss is obtained by integrating over the whole bandwidth of interest. The operations of integrating over the frequency and calculation of the expectation essentially have the same effect, namely averaging out the small-scale fading [55]. The parameters of IEEE 802.15.4a models are described comprehensively in [55] and [88]. Therefore, we do not repeat them here and refer the interested reader to these readable references.

Channel modelling research activities for mm-wave systems have gain a huge momentum recently. This is mainly due to the promise of multi-gigabit per second data transfers offered by the use of mm-wave frequencies. Thus, many research groups and standardisation bodies have developed or are developing channel models for mm-wave frequencies. Recently, the 3rd Generation Partnership Project (3GPP), the global standards body of the wireless industry, have released channel models covering frequencies from 0.5 to 100 GHz in the technical report 3GPP TR 38.901 version 14.0.0 Release 14 [133]. It includes scenarios such as urban microcell (UMi), urban macrocell (UMa), indoor, backhaul, device to device (D2D), vehicle to vehicle (V2V) and other scenarios such as stadium and gym.

Research projects including industry and academia have been developing 5G channel propagation models including mmWaves. These include but are not limited to METIS [82], MiWEBA [80], NYU WIRELESS [108, 67, 116], and mmMagic [81].

Researchers at New York University (NYU) have also developed a statistical spatial channel model for BB mm-wave wireless communication systems. They have also developed a channel simulation software named NYUSIM [93, 134], which can be used to generate temporal and spatial channel responses to support physical and link layer simulations and design for fifth generation (5G) cellular communications.

Up-to-date information on path loss and shadowing models for frequency range 0.5-100 GHz is surveyed in [107] which is the most recent publication on channel models for mm-wave BB channels.

Appendix B

Signal Spaces and a Generalised Sampling Formula

In this appendix, some mathematical preliminaries are provided. This Appendix includes an introduction to the geometry of SI subspaces and sampling theory.

B.1 Hilbert Spaces

All physical signals have finite energy. Therefore, an appropriate context for geometrical study of signals is the space of all finite-energy signals with certain reasonable conditions that make the analysis, processing and synthesis of signals mathematically tractable. Hilbert spaces are abstract vector spaces that provide a suitable geometrical framework for studying a wide class of signals. To define Hilbert spaces, we need the concepts of inner product, norm and completeness.

An inner product on a complex (real) vector space H is a mapping

$$\langle \cdot, \cdot \rangle : H \times H \to \mathbb{C}\ (\mathbb{R}), \tag{B.1}$$

for which

- $\langle \alpha x + \beta y, z \rangle = \alpha \langle x, z \rangle + \beta \langle y, z \rangle,\ \forall x, y, z \in H,\ \forall \alpha, \beta \in \mathbb{C}$;
- $\langle x, y \rangle = \overline{\langle y, x \rangle},\ \forall x, y \in H$;
- $\langle x, x \rangle \geq 0,\ \forall x \in H$, and $\langle x, x \rangle = 0 \iff x = 0$.

A vector space with an inner product is called an inner product space. An inner product

space can be equipped with a norm

$$\|x\| \triangleq \sqrt{\langle x, x\rangle},\ x \in H. \tag{B.2}$$

An inner product space H is called complete if any Cauchy sequence in H is convergent to a vector in H. Recall that a sequence $\{x_k\}_{k=1}^{\infty}$ in H is Cauchy if for each $\epsilon > 0$ there exists $N \in \mathbb{N}$ such that $\|x_k - x_l\| \leq \epsilon$ whenever $k, l \geq N$. A *Hilbert space* is a complete inner product space.

Relevance of the theory of Hilbert spaces to signal analysis can be witnessed by the following important examples of Hilbert spaces.

Example B.1.1 (Example 1.)**.** The space of all real-valued finite-energy signals, $\mathcal{L}_2$, is a real Hilbert space. Each vector in this space is a real-valued function on $\mathbb{R}$. The inner product is defined by

$$\langle f(t), g(t)\rangle = \int_{-\infty}^{\infty} f(t)g(t)\,\mathrm{d}t. \tag{B.3}$$

Technically the functions are assumed to be Lebesgue measurable and the integration in B.3 is with respect to Lebesgue measure, otherwise the space is not completer. In signal processing applications these technical assumptions can usually be ignored as practical signals are usually Riemann integrable.

The space of complex-valued Lebesgue measurable finite-energy signals defined on $\mathbb{R}$ is a complex Hilbert space. This space is also denoted by $\mathcal{L}_2$ but it should be clear from the context which space is under consideration. For this space the inner product is defined by

$$\langle f(t), g(t)\rangle = \int_{-\infty}^{\infty} f(t)\overline{g(t)}\,\mathrm{d}t, \tag{B.4}$$

where overbar denoted the complex conjugation operator.

Example B.1.2 (Example 2.)**.** The space of finite-energy discrete-time (DT) signals (or sequences), $\ell_2(\mathbb{Z})$, is a Hilbert space. The on-sided variant of $\ell_2(\mathbb{Z})$, denoted by $\ell_2(\mathbb{N})$, is also a Hilbert space. When the sequences are real valued, the space is a real Hilbert space and when they are complex valued, the space is a complex Hilbert space.

The inner product in $\ell_2(\mathbb{Z})$ is defined by

$$\langle \{f_k\}_{k\in\mathbb{Z}}, \{g_k\}_{k\in\mathbb{Z}} \rangle = \sum_{-\infty}^{\infty} f_k \overline{g_k}, \tag{B.5}$$

for $\{f_k\}_{k\in\mathbb{Z}}$ and $\{g_k\}_{k\in\mathbb{Z}} \in \ell_2(\mathbb{Z})$. While all realized signals in electrical engineering are continuous-time (CT) signals, in digital signal processing it is appropriate to use DT signals. DT signals are usually obtained by a sampling or correlation process. As a result of sampling an element of the Hilbert space $\mathcal{L}_2$ is mapped to an element of $\ell_2(\mathbb{Z})$.

The elements of $\mathcal{L}_2$ are functions. Therefore, it is suitable to refer to its elements by using the function names. For example, it is preferred to write $f \in \mathcal{L}_2$ instead of $f(t) \in \mathcal{L}_2$. Similarly, it is more relevant to write $\langle f, g \rangle$, rather to write $\langle f(t), g(t) \rangle$, as $f(t)$ and $g(t)$ are real or complex numbers. However, in this thesis we have not followed this notation rule as it is not common in engineering literature [164, 122, 74, 75].

Example B.1.3 (Example 3.)**.** The spaces of real and complex vectors of length N, denoted respectively by $\mathbb{R}^N$ and $\mathbb{C}^N$, are Hilbert spaces. The Hilbert space inner product for these spaces correspond to the usual inner product (or, dot product) of vectors. In digital signal processing, these are the most relevant spaces.

B.2 Shift-Invariant Spaces

We consider only closed subspaces of $\mathcal{L}_2$. Finitely-generated subspaces are always closed. A subspace V of $\mathcal{L}_2$ which is invariant with respect to α-shifts if

$$T_{k\alpha} f(t) \triangleq f(t - k\alpha) \in V;\ \forall k \in \mathbb{Z},\ \forall f(t) \in V. \tag{B.6}$$

Apparently, $\mathcal{L}_2$ is an $\alpha-$shift-invariant ($\alpha-$SI) subspace. An $\alpha-$SI subspace is called an $\alpha-$principal shift invariant ($\alpha-$PSI) if it is generated by a $\alpha-$shifts of a single function. That is V is an $\alpha-$PSI subspace if there exists $\varphi(t) \in \mathcal{L}_2$ such that

$$V = \overline{\text{span}}\{\varphi(t - k\alpha) :\ k \in \mathbb{Z}\}, \tag{B.7}$$

where $\overline{\text{span}}$ denotes the closed linear span.

PSI subspaces of $\mathcal{L}_2$ appear in various topics of mathematics and engineering [4, 21]. Here, we are interested in the following appearance of PSI subspaces in communication theory.

Example B.2.1. In communication theory, transmission of information is made possible by using pulses. In mathematical terms, each pulse is a function with a short duration and essentially-limited bandwidth. In systems employing a linear modulation scheme [102], each pulse is multiplied by a real or complex number and then the sequence of modulated pulses are transmitted. In some cases the multipliers are chosen from a finite set of symbols, i.e., the constellation points. In some cases, the multipliers are not chosen from a finite set. For example, in OFDM systems a finite sequence of information symbols are transformed using the inverse discrete Fourier transform (IDFT) (implemented by IFFT) into a set of complex numbers. Then these complex numbers are transmitted by using a pulse. In any case, the baseband transmitted signal can be represented as

$$s(t) = \sum_k d_k p(t - kT_d) \tag{B.8}$$

where T_d is the symbol interval and the summation is over a finite set. Therefore, the transmitted signal belongs to the T_d-PSI subspace generated by the pulse, $p(t)$.

B.3 Sampling Theorems

The sampling theorem of Shannon (or, Whittaker-Kotelnikov-Shannon sampling theorem [57]) is fundamental for digital communications. It states that any finite-energy bandlimited function can be characterised by a sequence of equidistant samples of that function. We say $g(t)$ is bandlimited to W if $G(f) = 0$ for $|f| > W$. The space of all $\mathcal{L}_2$ functions bandlimited to W is called a Paley-Wiener space [46] and is usually denoted by PW_W. PW_W is a Hilbert subspace of $\mathcal{L}_2$. If t is the time variable measured in seconds, f and W are frequencies in Hertz. The following theorem is often referred to as Shannon sampling theorem in communication theory literature. The same appellation is common in other engineering fields. Apparently, this theorem has much longer history in mathematical literature [51, 11, 70].

Theorem B.3.1 (Shannon Sampling Theorem)**.** *Let* $g(t) \in \mathrm{PW}_W$*. Then,*

$$g(t) = \frac{1}{2W} \sum_{k=-\infty}^{\infty} g\left(\frac{k}{2W}\right) \operatorname{sinc}\left(\frac{t-k}{2W}\right), \tag{B.9}$$

where the series is convergent in $\mathcal{L}_2-$*norm, absolutely and uniformly on* $\mathbb{R}$*.*

The function $\operatorname{sinc}(t)$ and its unitary dilations defined by

$$D_\beta \operatorname{sinc}(t) = \sqrt{\beta} \operatorname{sinc}(\beta t),\ \beta \in \mathbb{R}, \tag{B.10}$$

are sampling functions. That is, for every finite-energy signal continuous at t_0, we have

$$\Big\langle g(t), \sqrt{\beta} \operatorname{sinc}(\beta t - t_0) \Big\rangle = g\left(\frac{t_0}{\beta}\right). \tag{B.11}$$

Therefore, using the Hilbert space notations the series in (B.9) can be written as

$$g(t) = \sum_{k=-\infty}^{\infty} \Big\langle g(t), D_{\frac{1}{2W}} \operatorname{sinc}(t-k) \Big\rangle D_{\frac{1}{2W}} \operatorname{sinc}(t). \tag{B.12}$$

(B.11) and (B.12) show the sampling and interpolation process which is used in many applications. Sampling process usually consists of a lowpass prefiltering to reduce the out-of-band noise and other irrelevant signal components. (B.11) represents the operations of lowpass prefiltering by an ideal lowpass filter with two-sided bandwidth β, and ideal sampling which is mathematically equivalent to multiplication by the shifted Dirac's delta distribution, $\delta(t - t_0/\beta)$, and integration over $\mathbb{R}$. Both sinc function and δ distribution are not realisable in practice. That is, absolute band limiting and instantaneous sampling are impossible in practice. Modern analogue-to-digital converter (ADC) designs try to increase the precision of sampling operation [155]. The ideal lowpass filtering is usually approximated by other non-ideal lowpass filters. Historically, the most widely used lowpass filters are Butterworth, Chebychev and elliptic filters [94].

Theorem B.3.2 (A Generalised Sampling Theorem)**.** *Let* $0 < W_0 \leq W_1$*,* $s(t) \in \mathrm{PW}_{W_1}$

and $S(f)$ be a bounded function with the property that

$$\forall f \in \mathbb{R},\ \sum_{k=-\infty}^{\infty} S(f - 2kW_0) = 1. \tag{B.13}$$

Then,

$$\forall g(t) \in \mathrm{PW}_{W_0},\ g(t) = \frac{1}{2W_0} \sum_{k=-\infty}^{\infty} g\left(\frac{k}{2W_0}\right)\, s\left(t - \frac{k}{2W_0}\right), \tag{B.14}$$

where the series is convergent in $\mathcal{L}_2-$norm, absolutely and uniformly on $\mathbb{R}$.

This theorem follows from Theorem 9.1 in [156] and the characterisation if shift invariant subspaces on page 43. In the special case where $W_0 = W_1$, statement of Theorem B.3.2 reduces to that of Theorem B.3.1. Theorem B.3.2 is more useful than the Shannon sampling theorem for two reasons: 1) the function $s(t)$ can be chosen to have smooth spectral rolloff and then the convergence rate of the generalised sampling expansion is higher than the Shannon sampling expansion, and 2) the interpolating filter in the generalised sampling theorem is realisable. These are practical advantages of the generalised sampling formula.

Appendix C

Electromagnetics

In Chapter 3, we have used electromagnetics wave propagation properties in our study of pulse distortion in indoor environments. This appendix provides a short route to derive Maxwell's field equations from fundamental rules of physics and introduces the frequency-dependent constitutive parameters of materials. All textbooks on electromagnetics cover this topic in detail, but it takes several chapters [5]. I found very helpful to have a handy reference to these mathematically elegant and practically ubiquitous equations.

C.1 Coulomb's Law

There is a force between small charged bodies (point charges) which is directly proportional to the charge magnitudes and inversely proportional to the square of their distance. Denoting the force vector magnitude by F, the coulomb's law states that

$$F = \frac{Q_1 Q_2}{4\pi\epsilon d^2}, \tag{C.1}$$

where, F is in newtons (N), Q_1 and Q_2 are the charge magnitudes in coulombs (C), d is the distance in metres (m). $\epsilon > 0$ is the permittivity of the medium with the units $\mathrm{C}^2/\mathrm{N.m}^2 = \mathrm{F/m}$, where F is the unit of capacitance, farad. For free space or vacuum, $\epsilon = \epsilon_0 = 8.854 \times 10^{-12}$ F/m. For media other than free space, $\epsilon = \epsilon_0\epsilon_r$, where ϵ_r is the relative permittivity or dielectric constant of the medium.

C.2 Electric Field and Electric Flux Density

Assume that a point charge with magnitude Q is located at the origin of a spherical coordinate system in a medium permittivity ϵ. The electric field at a point P in the space, due to this charge, is given by

$$\mathbf{E} = \frac{Q}{4\pi\epsilon r^2}\,\mathbf{a}_r, \tag{C.2}$$

where $\mathbf{a}_r$ is the radial unit vector pointing towards P and r is the radial distance of P from the origin. The units of the magnitude of the electric field is newtons per coulomb (N/C) or the equivalent, volts per metre (V/m).

Point charges do not exist unless as part of a mass. The smallest division is found to be an electron or proton. In dealing with volume charges, it is useful to consider a continuous charge distribution and to define a charge density by $\rho_\nu = \mathrm{d}Q/\,\mathrm{d}v$ (C/m^3), where $\mathrm{d}v$ is the volume element and $\mathrm{d}Q$ is the differential charge. Each differential charge produce a differential electric field

$$\mathrm{d}\mathbf{E} = \frac{\mathrm{d}Q}{4\pi\epsilon R^2}\mathbf{a}_R, \tag{C.3}$$

at an observation point P, where $\mathbf{a}_R$ is the radial unit vector with initial point located at the differential charge element pointing towards P. The total electric field at point P is the integral of (C.3) over the charge volume. Note that this integral depends on the volume charge's geometrical shape, the charge density distribution and the medium.

The electric flux density, $\mathbf{D}$, due to a volume charge within a closed surface S is a vector field on S related to the electric field on S through $\mathbf{D} = \epsilon\mathbf{E}$. By Gauss's law, the total electric flux, Ψ, passing through the closed surface S is equal to the total charge enclosed by the surface. That is,

$$\Psi = \oint_S \mathbf{D}\cdot\,\mathrm{d}\mathbf{S} = Q, \tag{C.4}$$

where $\mathrm{d}\mathbf{S} = \mathbf{n}\,\mathrm{d}S$, $\mathbf{n}$ being the unit normal vector field on S. By using divergence

theorem and shrinking the closed surface to a point we obtain

$$\nabla \cdot \mathbf{D} = \rho_\nu, \tag{C.5}$$

where ρ_ν is the volume charge density function. This is a localised version of Gauss's law.

C.3 Magnetic Field and Magnetic Flux Density

Assuming that a current I is flowing a filamentary conductor with a differential vector length $\mathrm{d}\mathbf{L}$. By the experimental law of Biot-Savart, at a point P the magnitude of the magnetic field produced by the differential element is the differential magnetic field

$$\mathrm{d}\mathbf{H} = \frac{I\,\mathrm{d}\mathbf{L} \times \mathbf{a}_R}{4\pi R^2}, \tag{C.6}$$

where, $\mathbf{a}_R$ is a unit vector with initial point located at the differential element pointing towards P and R is the distance of the differential length element from P. The units of the magnetic field magnitude are amperes per metre (A/m).

For distributed sources, such as volume current density $\mathbf{J}$ (A/m^2) and surface current density $\mathbf{K}$ (A/m), the Biot-Savart's law reads as

$$\mathbf{H} = \int_S \frac{\mathbf{K} \times \mathbf{a}_R}{4\pi R^2}\,\mathrm{d}S, \text{ and} \tag{C.7}$$

$$\mathbf{H} = \int_V \frac{\mathbf{J} \times \mathbf{a}_R}{4\pi R^2}\,\mathrm{d}V. \tag{C.8}$$

The vector field $\mathbf{H}$ evaluated at each point P in the space gives the magnetic field vector at that point induced by volume or surface current with given densities.

Ampère's circuital law states that the line integral of $\mathbf{H}$ about any closed path is exactly equal to the direct current enclosed by that path,

$$\oint \mathbf{H} \cdot\, \mathrm{d}\mathbf{L} = I. \tag{C.9}$$

The point form of Amère's circuital law can be obtained by considering differential-sized closed paths in (C.9) (the shrinking technique) and using the notion of curl of a

vector field, as

$$\nabla \times \mathbf{H} = \mathbf{J}. \tag{C.10}$$

By using Stokes's theorem (C.9) can be derived from (C.10). This is a localised version of Ampère's law.

Similar to the electric flux density, the magnetic flux density in a medium with magnetic permeability μ is defined as

$$\mathbf{B} = \mu\mathbf{H}, \tag{C.11}$$

where $\mathbf{B}$ is measured in webers per square metre ($\mathrm{Wb/m^2}$) or teslas (T), where μ is called the permeability of the medium. For free space

$$\mu = \mu_0 = 4\pi \times 10^{-7}\,\mathrm{H/m}. \tag{C.12}$$

The magnetic flux, Φ, is defined as the flux passing through any designated surface area,

$$\Phi = \int_S \mathbf{B} \cdot \mathrm{d}\mathbf{S}, \tag{C.13}$$

and is measured in webers. Gauss's law for the magnetic field is

$$\oint_S \mathbf{B} \cdot \mathrm{d}\mathbf{S} = 0. \tag{C.14}$$

(C.14) states that the net magnetic charge within a closed surface is always zero. An application of the divergence theorem shows that

$$\nabla \cdot \mathbf{B} = 0, \tag{C.15}$$

which is a localised version of (C.14).

C.4 Time-Varying Fields and Maxwell's Equations

Faraday's law states that a time-varying magnetic flux passing through a surface S with boundary L produces an electromotive force (emf) along L. Quantitatively,

$$\text{emf} \triangleq \oint_L \mathbf{E} \cdot \mathrm{d}\mathbf{L} = -\frac{\mathrm{d}\Phi}{\mathrm{d}t} = -\frac{\mathrm{d}}{\mathrm{d}t}\int_S \mathbf{B} \cdot \mathrm{d}\mathbf{S}. \tag{C.16}$$

where the third equality follows from (C.13). Assuming a stationary path, the time derivative can be moved inside the integral. Then, applying Stoke's theorem yields

$$\int_S (\nabla \times \mathbf{E}) \cdot \mathrm{d}\mathbf{S} = -\int_S \frac{\partial \mathbf{B}}{\partial t} \cdot \mathrm{d}\mathbf{S}. \tag{C.17}$$

By shrinking the surface to a point we obtained

$$\nabla \times \mathbf{E} = -\frac{\partial \mathbf{B}}{\partial t}. \tag{C.18}$$

This is a localised version of Faraday's law.

Equations (C.10) and (C.18) are inconsistent with the equation of continuity,

$$\nabla \cdot \mathbf{J} = -\frac{\partial \rho_\nu}{\partial t}, \tag{C.19}$$

which is a necessary condition for the principle of conservation of charge to be valid. To guarantee the consistency of these equations it is sufficient to modify Ampère's circuital law as

$$\nabla \times \mathbf{H} = \mathbf{J} + \frac{\partial \mathbf{D}}{\partial t}. \tag{C.20}$$

The term $\frac{\partial \mathbf{D}}{\partial t}$ is called a displacement current density. It is introduced by Maxwell. (C.20) is referred to as the generalised Ampère's law. It's integral form can be obtained by using Stoke's theorem as

$$\oint_L \mathbf{H} \cdot \mathrm{d}\mathbf{L} = \int_S (\mathbf{J} + \frac{\partial \mathbf{D}}{\partial t}) \cdot \mathrm{d}\mathbf{S}, \tag{C.21}$$

where S is a surface with contour L.

Table C.1: Maxwell's equations.

Reference	Differential Form	Integral Form	Equations
Gauss's law	$\nabla \cdot \mathbf{D} = \rho_\nu$	$\Psi = \oint_S \mathbf{D} \cdot \mathrm{d}\mathbf{S} = Q$	(C.5),(C.4)
Faraday's law	$\nabla \times \mathbf{E} = -\frac{\partial \mathbf{B}}{\partial t}$	$\oint_L \mathbf{E} \cdot \mathrm{d}\mathbf{L} = -\int_S \frac{\partial \mathbf{B}}{\partial t} \cdot \mathrm{d}\mathbf{S}$	(C.18),(C.16),(C.17)
Gauss's law	$\nabla \cdot \mathbf{B} = 0$	$\oint_S \mathbf{B} \cdot \mathrm{d}\mathbf{S} = 0$	(C.15),(C.14)
Ampère's law	$\nabla \times \mathbf{H} = \mathbf{J} + \frac{\partial \mathbf{D}}{\partial t}$	$\oint_L \mathbf{H} \cdot \mathrm{d}\mathbf{L} = \int_S (\mathbf{J} + \frac{\partial \mathbf{D}}{\partial t}) \cdot \mathrm{d}\mathbf{S}$	(C.20),(C.21)

In this subsection, up to this point, we have obtained the four fundamental equations of electromagnetic, referred to as Maxwell's equations. These equations, together with their integral forms are summarized in Table C.1.

C.5 Constitutive Parameters

The electromagnetic constitutive parameters of material are its permittivity ϵ, permeability μ, and conductivity σ. The electrical permittivity is related to the resistance of a material against formation of electric field. This can be seen from the equation of Coulomb's law (C.1). Permeability is the magnetic analogue of the permittivity. The following relations between electric and magnetic fields and flux densities exist:

$$\mathbf{D} = \epsilon \mathbf{E}, \ \mathbf{B} = \mu \mathbf{H}, \tag{C.22}$$

which are usually referred to as th constitutive relations. These relations are valid as far as the material is homogeneous. ϵ and μ are usually very small numbers. Therefore, the corresponding parameters for vacuum are considered as bases and the relative permittivity (dielectric constant) and relative permeability (magnetic constant) are defined as

$$\epsilon_r = \frac{\epsilon}{\epsilon_0}, \text{ and } \mu_r = \frac{\mu}{\mu_0}, \tag{C.23}$$

where,

$$\epsilon_0 \approx \frac{1}{36\pi} \times 10^{-9}, \text{ and } \mu_0 = 4\pi \times 10^{-7}. \tag{C.24}$$

The units of ϵ and μ, derived from (C.22), are F/m (farads per metre) and H/m (henries per metre).

ϵ and μ characterize the electric and magnetic properties of a material (or the vacuum!). The conductivity, σ, characterizes the ease with which charges can move freely in a material. Given an electric field $\mathbf{E}$, the current density created in the material is $\mathbf{J} = \sigma\mathbf{E}$. In particular, $\sigma = 0$ means that charges (electrons) cannot move more than atomic distance. However, electron cloud polarization can occur. These materials are called perfect dielectrics. $\sigma = \infty$ means that electrons can move freely throughout the material, which is then called a perfect conductor.

C.6 Time-Harmonic (TH) Electric Fields

All vector fields described above, and denoted by boldface letters, can be time dependent. In particular, the time dependence can be harmonic. This means that

$$\mathbf{E}(\mathbf{p}; t) = \tilde{\mathbf{E}}(\mathbf{p}) \cos(2\pi f t + \phi_0) \tag{C.25}$$

$$= \mathrm{Re}[\tilde{\mathbf{E}}(\mathbf{p}) \mathrm{e}^{\mathrm{j}\, 2\pi f t + \phi_0}], \tag{C.26}$$

where,

- $\mathbf{p}$ is the position vector,
- f is the frequency of the harmonic,
- ϕ_0 is the phase of the harmonic, and
- $\tilde{\mathbf{E}}(\mathbf{p})$ is the phasor vector.

Knowing f and ϕ_0, $\mathbf{E}$ can be characterized by using $\tilde{\mathbf{E}}$. Assuming a constant frequency and phase, we will use boldface capital letters without tilde to represent the phasor vectors.

By using the constitutive relations (C.22) and $\mathbf{J} = \sigma\mathbf{E}$, Maxwell's equations assume the following form in phasor domain

$$\nabla \cdot \mathbf{E} = \frac{\rho_\nu}{\epsilon}, \tag{C.27}$$

$$\nabla \times \mathbf{E} = -\mathrm{j}2\pi f\mu\mathbf{H}, \tag{C.28}$$

$$\nabla \cdot \mathbf{H} = 0, \text{ and} \tag{C.29}$$

$$\nabla \cdot \mathbf{H} = (\sigma + \mathrm{j}2\pi f\epsilon)\mathbf{E}. \tag{C.30}$$

By defining the complex permittivity as $\epsilon_\mathrm{c} = \epsilon - \mathrm{j}\frac{\sigma}{2\pi f}$, (C.30) can be rewritten as

$$\nabla \times \mathbf{H} = \mathrm{j}2\pi f\epsilon_c\mathbf{E}. \tag{C.31}$$

For perfect dielectrics ($\sigma = 0$), $\epsilon_c = \epsilon$. For other lossy dielectrics, ϵ_c is frequency dependent. The frequency dependency of ϵ_c causes pulse distortion when pulses propagate inside a lossy dielectric, reflects off, or transmits through a surface.

References

[1] IEEE 802.11ad-2012. *Wireless LAN Medium Access Control (MAC) and Physical Layer (PHY) Specifications Amendment 3: Enhancements for Very High Throughput in the 60 GHz Band*. IEEE, 2012.

[2] IEEE 802.15.4-2011. *IEEE Standard for Local and metropolitan area networks–Part 15.4: Low-Rate Wireless Personal Area Networks (LR-WPANs)*. IEEE, 2011.

[3] IEEE 802.15.4-2015. *IEEE Standard for Low-Rate Wireless Networks*. IEEE, 2015.

[4] Akram Aldroubi and Karlheinz Gröchenig. "Nonuniform Sampling and Reconstruction in Shift-Invariant Spaces". In: *SIAM Review* 43.4 (2001), pp. 585–620.

[5] C. A. Balanis. *Advanced Engineering Electromagnetics*. 2nd ed. John Wiley & Sons, 2012.

[6] C. A. Balanis. *Antenna Theory: Analysis and Design*. Wiley-Interscience, 2005. ISBN: 0471714623.

[7] P.R. Barnes and F.M. Tesche. "On the direct calculation of a transient plane wave reflected from a finitely conducting half space". In: *IEEE Trans. Electromagn. Compat.* 33.2 (1991), pp. 90–96. ISSN: 0018-9375. DOI: 10.1109/15.78345.

[8] J. R. Barry, E. A. Lee, and D. G. Messerschmitt. *Digital Communication*. Springer US, 2004.

[9] P. Bello. "Characterization of Randomly Time-Variant Linear Channels". In: *IEEE Trans. Commun. Systems* 11.4 (1963), pp. 360–393. ISSN: 0096-1965. DOI: 10.1109/TCOM.1963.1088793.

[10] P.A. Bello. "Evaluation of mobile ultra wideband modems in dense multipath-part 1: channel model". In: *IEEE Trans. Wireless Commun.* 6.11 (2007), pp. 4145–4153. ISSN: 1536-1276. DOI: 10.1109/TWC.2007.060268.

[11] J.J. Benedetto and P.J.S.G. Ferreira. *Modern Sampling Theory: Mathematics and Applications*. Applied and Numerical Harmonic Analysis. Birkhäuser Basel, 2001.

[12] S. Benedetto and E. Biglieri. *Principles of Digital Transmission with Wireless Applications*. New York: Plenum, 1998.

[13] A. Bhattacharyya. "On a measure of divergence between two multinomial populations". In: *The Indian Journal of Statistics* 7.4 (1946), pp. 401–406.

[14] E. Biglieri, J. Proakis, and S. Shamai. "Fading channels: information-theoretic and communications aspects". In: *IEEE Trans. Inf. Theory* 44.6 (1998), pp. 2619–2692.

[15] J.A.C. Bingham. *The Theory and Practice of Modem Design*. Wiley, 1988.

[16] Carl de Boor, Ronald A. Devore, and Amos Ron. "Approximation from Shift-Invariant Subspaces of $L^2(\mathbb{R}^d)$". English. In: *Transactions of the American Mathematical Society* 341.2 (1994), pp. 787–806.

[17] D. M. Brady. "An adaptive coherent diversity receiver for data transmission through dispersive media". In: *Conf. Rec. ICC 70*. 1970, pp. 21.35–21.40.

[18] L.M. Brekhovskikh. *Waves in Layered Media*. Applied mathematics and mechanics. Academic Press, 1980.

[19] R. M. Buehrer et al. *Ultra-wideband Propagation Measurements and Modeling*. Tech. rep. DARPA NETEX Program Final Report.

[20] D. Cassioli, M. Z. Win, and A. F. Molisch. "The ultra-wide bandwidth indoor channel: from statistical model to simulations". In: *IEEE Journal on Selected Areas in Communications* 20.6 (2002), pp. 1247–1257.

[21] O. Christensen. *An Introduction to Frames and Riesz Bases*. Boston: Birkhäuser, 2003.

[22] J. M. Cioffi. *Signal Processing and Detection*. class notes. Department of Electrical Engineering, Stanford University. URL: http://web.stanford.edu/group/cioffi/.

[23] R.J.-M. Cramer, R.A. Scholtz, and M.Z. Win. "Evaluation of an ultra-wideband propagation channel". In: *IEEE Trans. Antennas Propag.* 50.5 (2002), pp. 561–570.

[24] I. Daubechies. *Ten Lectures on Wavelets*. Philadelphia, PA: SIAM, CBMS-NSF Regional Conference Series in Applied Mathematics, vol. 61, 1992.

[25] M. A. Davenport et al. "A wideband compressive radio receiver". In: *Proc. MILCOM*. 2010, pp. 1193–1198. DOI: 10.1109/MILCOM.2010.5680108.

[26] M. G. diBenedetto et al., eds. *UWB Communication Systems, A Comprehensive Overview*. Hindawi Publishing Corporation, 2006.

[27] M. Dobroslovacki and H Fan. "Wavelet-based linear system modeling and adaptive filtering". In: *IEEE Trans. Signal Process.* 44.5 (1996), pp. 1156–1167.

[28] *Effects of building materials and structures on radiowave propagation above about 100 MHz*. ITU Recommendation P.2040-1 (07/2015). 2015. URL: http://www.itu.int/rec/R-REC-P.2040-1-201507-I.

[29] Yonina C. Eldar, Alan V. Oppenheim, and Dianne Egnor. "Orthogonal and projected orthogonal matched filter detection". In: *Signal Processing* 84.4 (2004), pp. 677 –693.

[30] B. Farhang-Boroujeny. *Adaptive Filters: Theory and Applications*. Wiley, 2013.

[31] *FCC First Report and Order, Revision of Part 15 of the Commission's Rules Regarding Ultra-wideband Transmission Systems, ET-Docket 98-153*. 2002.

[32] D. Ferreira et al. "A review on the electromagnetic characterisation of building materials at micro- and millimetre wave frequencies". In: *The 8th European Conference on Antennas and Propagation (EuCAP 2014)*. 2014, pp. 145–149. DOI: 10.1109/EuCAP.2014.6901713.

[33] Channel modeling sub-committee report (final). *IEEE P802.15 Wireless Personal Area Networks*. 2003.

[34] G. Forney. “Maximum-likelihood sequence estimation of digital sequences in the presence of intersymbol interference”. In: *IEEE Trans. Inform. Theory* 18.3 (1972), pp. 363–378.

[35] R.G. Gallager. *Principles of Digital Communication*. Cambridge University Press, 2008.

[36] W.A. Gardner. *Cyclostationarity in communications and signal processing*. New York, NY: IEEE Press, 1994.

[37] D. Ghosh et al. “Transmission and Reception by Ultra-Wideband UWB Antennas”. In: *IEEE Antennas Propag. Mag.* 48.5 (2006), pp. 67–99.

[38] G. B. Giannakis. “Cyclostationary signal analysis”. In: *Digital Signal Processing Fundamentals*. Ed. by Vijay Madisetti. 2nd ed. Boca Raton, FL: CRC Press, Inc., 2009.

[39] G.B. Giannakis and C. Tepedelenlioglu. “Basis expansion models and diversity techniques for blind identification and equalization of time-varying channels”. In: *Proc. IEEE* 86.10 (1998), pp. 1969–1986. ISSN: 0018-9219. DOI: 10.1109/5.720248.

[40] R. D. Gitlin, J. Hayes, and S. B. Weinstein. *Data Communications Principles*. Springer US, 1992.

[41] R. D. Gitlin, H. C. Meadors, and S. B. Weinstein. “The tap-leakage algorithm: An algorithm for the stable operation of a digitally implemented, fractionally spaced adaptive equalizer”. In: *Bell Syst. Tech. J.* 61.8 (1982), pp. 1817–1839.

[42] R.D. Gitlin and S.B. Weinstein. “Fractionally-spaced equalization: An improved digital transversal equalizer”. In: *Bell Syst. Tech. J.* 60.2 (1981), pp. 275–296.

[43] K. Gröchenig. *Foundations of Time-Frequency Analysis*. Boston, MA: Birkhäuser, 2001.

[44] L. Guidoux. “Egaliseur autoadaptif à double échantillonnage”. In: *L’Onde Electrique* 55 (1975), pp. 9–13.

[45] D. Halliday, R. Resnick, and J. Walker. *Fundamentals of Physics*. John Wiley & Sons, 2010.

[46] G. H. Hardy. "Notes on special systems of orthogonal functions, IV: The orthogonal functions of Whittaker's cardinal series". In: *Proc. Cambridge Philos. Soc.* (1941), pp. 331–348.

[47] Simon Haykin. *Adaptive filter theory*. 4th. Upper Saddle River, NJ: Prentice Hall, 2002.

[48] Simon Haykin. *Neural Networks: A Comprehensive Foundation*. 3rd ed. Upper Saddle River, NJ: Prentice-Hall, Inc., 2007.

[49] R. He et al. "On the clustering of radio channel impulse responses using sparsity-based methods". In: *IEEE Trans. Antennas Propag.* 64.6 (2016), pp. 2465–2474. ISSN: 0018-926X. DOI: 10.1109/TAP.2016.2546953.

[50] O.S. Heavens. *Optical Properties of Thin Solid Films*. Dover Publications, 1991.

[51] J. R. Higgins. "Five short stories about the cardinal series". In: *Bull. Amer. Math. Soc. (N.S.)* 12.1 (Jan. 1985), pp. 45–89.

[52] R. Hoctor and H. Tomlinson. "Delay-hopped transmitted-reference RF communications". In: *IEEE Conference on Ultra Wideband Systems and Technologies*. 2002, pp. 265–269.

[53] Lars Hörmander. "Estimates for translation invariant operators in L^p spaces". In: *Acta Math.* 104.1-2 (1960), pp. 93–140.

[54] B. Hu and N. C. Beaulieu. "Pulse shapes for ultrawideband communication systems". In: *IEEE Trans. Wireless Commun.* 4.4 (2005), pp. 1789–1797. ISSN: 1536-1276. DOI: 10.1109/TWC.2005.850311.

[55] *IEEE 802.15.4a channel model - final report*. URL: https://mentor.ieee.org/802.15/dcn/04/15-04-0662-00-004a-channel-model-final-report-r1.pdf (visited on 2017).

[56] W.C. Jakes. *Microwave mobile communications*. IEEE Press classic reissue. IEEE Press, 1974. ISBN: 9780780310698.

[57] A. J. Jerri. "The Shannon sampling theorem−Its various extensions and applications: A tutorial review". In: *Proc. IEEE* 65.11 (1977), pp. 1565–1596. ISSN: 0018-9219. DOI: 10.1109/PROC.1977.10771.

[58] Ye Jiang and A. Papandreou-Suppappola. "Discrete time-scale characterization of wideband time-varying systems". In: *IEEE Trans. Signal Process.* 54.4 (2006), pp. 1364–1375. ISSN: 1053-587X. DOI: 10.1109/TSP.2006.870558.

[59] T. Kailath. *Sampling Models for Linear Time-variant Filters.* Tech. rep. MIT: Research Laboratory of Electronics, 1959.

[60] T. Kailath. "The Divergence and Bhattacharyya Distance Measures in Signal Selection". In: *IEEE Trans. Commun. Technol.* 15.1 (1967), pp. 52–60.

[61] G. Karam, P. Moreau, and H. Sari. "Stabilizing fractionally-spaced equalizers". In: *GLOBECOM '91.* 1991, 1807–1811 vol.3.

[62] H. Krim and M. Viberg. "Two decades of array signal processing research: the parametric approach". In: *IEEE Signal Processing Magazine* 13.4 (1996), pp. 67–94.

[63] J. Kunisch and J. Pamp. "Measurement results and modeling aspects for the UWB radio channel". In: *IEEE Conference on Ultra Wideband Systems and Technologies, 2002. Digest of Papers.* 2002, pp. 19–23.

[64] D. Lamensdorf and L. Susman. "Baseband-pulse-antenna techniques". In: *IEEE Antennas Propag. Mag.* 36.1 (1994), pp. 20–30.

[65] H. J. Landau and H. O. Pollak. "Prolate spheroidal wave functions, Fourier analysis and uncertainty; III: The dimension of the space of essentially time- and band-limited signals". In: *Bell Syst. Tech. J.* 41.4 (1962), pp. 1295–1336.

[66] C.A. Gutierrez-Dtaz-de Leon, M. Cabrera-Bean, and M. Patzold. "On the Problems of Symbol-Spaced Tapped-Delay-Line Models for WSSUS Channels". In: *IEEE 66th Vehicular Technology Conference, 2007. VTC-2007 Fall.* 2007, pp. 920–925. DOI: 10.1109/VETECF.2007.201.

[67] G. MacCartney et al. "Indoor office wideband millimeter-wave propagation measurements and channel models at 28 GHz and 73 GHz for ultra-dense 5G wireless networks". In: *IEEE Access* 3 (2015), 2388–2424.

[68] W.Q. Malik, D.J. Edwards, and C.J. Stevens. "Frequency Dependence of Fading Statistics for Ultrawideband Systems". In: *IEEE Trans. Wireless Commun.* 6.3 (2007), pp. 800–804.

[69] A.R. Margetts, P. Schniter, and A. Swami. "Joint scale-lag diversity in wideband mobile direct sequence spread spectrum systems". In: *IEEE Trans. Wireless Commun.* 6.12 (2007), pp. 4308–4319. ISSN: 1536-1276. DOI: 10.1109/TWC.2007.05141.

[70] R.J. Marks. *Handbook of Fourier Analysis & Its Applications*. Oxford University Press, 2009.

[71] J. Mazo. "Faster-than-Nyquist signaling". In: *Bell Syst. Tech. J.* 54 (1975), pp. 1451–1462.

[72] J. S. McLean, H. Foltz, and R. Sutton. "Pattern descriptors for UWB antennas". In: *IEEE Trans. Antennas Propag.* 53.1 (2005), pp. 553–559.

[73] A. Meijerink and A. F. Molisch. "On the Physical Interpretation of the Saleh-Valenzuela Model and the Definition of Its Power Delay Profiles". In: *IEEE Trans. Antennas Propag.* 62.9 (2014), pp. 4780–4793.

[74] D. G. Messerschmitt. "A Geometric Theory of Intersymbol Interference". In: *Bell Syst. Tech. J.* 52.9 (1973), pp. 1483–1519.

[75] D. G. Messerschmitt. "A Geometric Theory of Intersymbol Interference". In: *Bell Syst. Tech. J.* 52.9 (1973), pp. 1521–1539.

[76] Yves Meyer. "Principe d'incertitude, bases hilbertiennes et algèbres d'opérateurs". fre. In: *Séminaire Bourbaki* 28 (1985-1986), pp. 209–223.

[77] Heinrich Meyr, Marc Moeneclaey, and Stefan Fechtel. *Digital Communication Receivers: Synchronization, Channel Estimation, and Signal Processing*. NY, USA: John Wiley & Sons, Inc., 1997. ISBN: 0471502758.

[78] N. Michelusi et al. "UWB Sparse/Diffuse Channels, Part I: Channel Models and Bayesian Estimators". In: *IEEE Trans. Signal Process.* 60.10 (2012), pp. 5307–5319.

[79] N. Michelusi et al. "UWB Sparse/Diffuse Channels, Part II: Estimator Analysis and Practical Channels". In: *IEEE Trans. Signal Process.* 60.10 (2012), pp. 5320–5333.

[80] *Millimetre-Wave Evolution for Backhaul and Access, D5.1, Channel Modeling and Characterization*. URL: https://www.metis2020.com/wp-content/uploads/METIS_D1.4_v3.pdf (visited on 2014).

[81] *mm-Wave Based Mobile Radio Access Network for 5G Integrated Communications, W2.1, 6-100 GHz Channel Modelling for 5G: Measurement and Modelling Plans in mmMAGIC*. URL: https://bscw.5g-mmmagic.eu/pub/bscw.cgi/d76988/mmMAGIC_WhitePaper-W2.1.pdf (visited on 2017).

[82] *Mobile and Wireless Communications Enablers for the Twenty-Twenty Information Society, D1.4, METIS Channel Models*. URL: https://www.metis2020.com/wp-content/uploads/METIS_D1.4_v3.pdf (visited on 2017).

[83] A. F. Molisch. "Ultrawideband propagation channels and their impact on system design". In: *International Symposium on Microwave, Antenna, Propagation and EMC Technologies for Wireless Communications*. 2007, pp. 1–5.

[84] A. F. Molisch, J. R. Foerster, and M. Pendergrass. "Channel models for ultrawideband personal area networks". In: *IEEE Wireless Commun.* 10.6 (2003), pp. 14–21.

[85] A.F. Molisch. "Ultra-Wide-Band Propagation Channels". In: *Proc. IEEE* 97.2 (2009), pp. 353–371. ISSN: 0018-9219. DOI: 10.1109/JPROC.2008.2008836.

[86] A.F. Molisch. "Ultrawideband propagation channels-theory, measurement, and modeling". In: *IEEE Trans. Veh. Technol.* 54.5 (2005), pp. 1528–1545. ISSN: 0018-9545. DOI: 10.1109/TVT.2005.856194.

[87] A.F. Molisch. *Wireless Communications*. Wiley - IEEE. Wiley, 2012. ISBN: 9781118355688.

[88] A.F. Molisch et al. "A Comprehensive Standardized Model for Ultrawideband Propagation Channels". In: *IEEE Trans. Antennas Propag.* 54.11 (2006), pp. 3151–3166. ISSN: 0018-926X. DOI: 10.1109/TAP.2006.883983.

[89] Florent Munier et al. "On the Effect of Antennas on UWB Systems". In: *Proceedings URSI General Assembly*, p. 2005.

[90] G. Narimani, P. A. Martin, and D. P. Taylor. "Analysis of Ultrawideband Pulse Distortion Due to Lossy Dielectric Walls and Indoor Channel Models". In: *IEEE Trans. Antennas. Propag.* 64.10 (2016), pp. 4423–4433.

[91] G. Narimani, P. A. Martin, and D. P. Taylor. "Spectral Analysis of Fractionally-Spaced MMSE Equalisers and Stability of the LMS Algorithm". In: *IEEE Trans. Commun.* (2017), *accepted*.

[92] V. H. Nascimento and A. H. Sayed. "Unbiased and stable leakage-based adaptive filters". In: *IEEE Trans. Signal Process.* 47.12 (1999), pp. 3261–3276. ISSN: 1053-587X.

[93] *NYUSIM*. URL: `http://wireless.engineering.nyu.edu/5gmillimeter-wave-channel-modeling-software/`.

[94] Alan V. Oppenheim and Ronald W. Schafer. *Discrete-Time Signal Processing*. 3rd ed. Upper Saddle River, N.J.: Prentice Hall, 2009.

[95] S. J. Orfanidis. *Electromagnetic Waves and Antennas*. Piscataway, NJ, July 2, 2014. URL: `http://www.ece.rutgers.edu/~orfanidi/ewa`.

[96] Recommendation ITU-R P.676-11. *Attenuation by atmospheric gases*. ITU, 2016.

[97] A. Papoulis and S. U. Pillai. *Probability, Random Variables, and Stochastic Processes*. Tata McGraw-Hill, 2002.

[98] Athanasios Papoulis. *The Fourier Integral and its Applications*. NY: McGraw-Hill, 1962.

[99] J.D. Parsons. *The mobile radio propagation channel*. second. John Wiley & Sons Ltd, 2000.

[100] Matthias Patzold. *Mobile Fading Channels*. NY: John Wiley & Sons, Inc., 2003.

[101] David M. Pozar. "Closed-form approximations for link loss in a UWB radio system using small antennas". In: *IEEE Trans. Antennas Propag.* 51.9 (2003), pp. 2346–2352.

[102] J. G. Proakis and M. Salehi. *Digital Communications*. 5th. Cambridge: McGraw-Hill, 2008.

[103] R. C. Qiu. "A generalized time domain multipath channel and its application in ultra-wideband (UWB) wireless optimal receiver design-Part II: physics-based system analysis". In: *IEEE Trans. Wireless Commun.* 3.6 (2004), pp. 2312–2324.

[104] R. C. Qiu. "A study of the ultra-wideband wireless propagation channel and optimum UWB receiver design". In: *IEEE J. Sel. Areas Commun.* 20.9 (2002), pp. 1628–1637.

[105] S. U. H. Qureshi. "Adaptive equalization". In: *Proc. IEEE* 73.9 (1985), pp. 1349–1387. ISSN: 0018-9219. DOI: 10.1109/PROC.1985.13298.

[106] S. U. H. Qureshi and G. D. Forney. "Properties and performance of $T/2$ equalizer". In: *Conf. Rec. NTC 77*. 1977, pp. 11.1.1–11.1.14.

[107] T. S. Rappaport et al. "Overview of Millimeter Wave Communications for Fifth-Generation (5G) Wireless Networks-with a Focus on Propagation Models". In: *IEEE Trans Antennas Propag. Early access* (2017).

[108] T. S. Rappaport et al. "Wideband millimeter-wave propagation measurements and channel models for future wireless communication system design". In: *IEEE Trans. Commun.* 63.9 (2015), 3029–3056.

[109] Theodore S. Rappaport et al. *Millimeter wave wireless communications*. Upper Saddle River, NJ: Prentice Hall, 2015.

[110] T.S. Rappaport. *Wireless Communications: Principles and Practice*. Prentice Hall communications engineering and emerging technologies series. Prentice Hall PTR, 2002.

[111] S. T. Rickard et al. "Canonical Time-frequency, Time-scale, and Frequency-scale Representations of Time-varying Channels". In: *Commun. Inf. Syst.* 05.2 (2005), pp. 197–226.

[112] Richard Rudd et al. *Building Materials and Propagation, Final Report*. Tech. rep. Ofcom, 2014. URL: http://stakeholders.ofcom.org.uk/binaries/research/technology-research/2014/building-materials-propagation/Building_Materials_and_Propagation.pdf.

[113] Walter Rudin. *Functional analysis*. 2nd ed. McGraw-Hill, 1991.

[114] Walter Rudin. *Real and complex analysis*. 3rd ed. McGraw-Hill, 1987.

[115] A. A. M Saleh and R. A. Valenzuela. “A statistical model for indoor multipath propagation”. In: *IEEE J. Sel. Areas Commun.* (1987), pp. 128–137.

[116] M. K. Samimi and T. S. Rappaport. “Statistical Channel Model with Multi-Frequency and Arbitrary Antenna Beamwidth for Millimeter-Wave Outdoor Communications”. In: *IEEE Globecom Workshops*. 2015, pp. 1–7.

[117] A. H. Sayed. *Fundamentals of Adaptive Filtering*. Hoboken, NJ: John Wiley & Sons Inc., 2003.

[118] A. Sayeed and B. Aazhang. “Joint multipath-Doppler diversity in mobile wireless communications”. In: *IEEE Trans. Commun.* 47.1 (1999), pp. 123–132.

[119] H. Schantz. *The Art and Science of Ultrawideband Antennas*. Artech House antennas and propagation library. Artech House, 2005.

[120] H.G. Schantz. “Dispersion and UWB antennas”. In: *Proc. IEEE Ultrawideband Systems and Technologies*. 2004, pp. 161–165. DOI: 10.1109/UWBST.2004.1320956.

[121] Robert A. Scholtz, David M. Pozar, and Won Namgoong. “Ultra-wideband radio”. In: *EURASIP J. Appl. Signal Process.* 2005 (2005), pp. 252–272. ISSN: 1110-8657.

[122] M. Schwartz. “Abstract vector spaces applied to problems in detection and estimation theory”. In: *IEEE Trans. Inf. Theory* 12.3 (1966), pp. 327–336.

[123] A. Shlivinski, E. Heyman, and R. Kastner. “Antenna characterization in the time domain”. In: *IEEE Trans. Antennas Propag.* 45 (1997), pp. 1140–1149.

[124] L. H. Sibul, L. G. Weiss, and T. L. Dixon. “Characterization of stochastic propagation and scattering via Gabor and wavelet transforms”. In: *Journal of computational acoustics* 2.3 (1994), pp. 345–369.

[125] M. K. Simon and M. S. Alouini. *Digital Communication over Fading Channels*. 2nd ed. Newark, NJ: Wiley, 2005.

[126] G. Sinclair. “The Transmission and Reception of Elliptically Polarized Waves”. In: *Proceedings of the IRE* 38.2 (1950), pp. 148–151.

[127] G.S. Smith. “A direct derivation of a single-antenna reciprocity relation for the time domain”. In: *IEEE Trans. Antennas Propag.* 52.6 (2004), pp. 1568–1577. ISSN: 0018-926X. DOI: 10.1109/TAP.2004.830257.

[128] A. Spalvieri et al. “Stabilizing the fractionally spaced equalizer by prewhitening”. In: *Proc. GLOBECOM*. Vol. 1. 1995, pp. 93–97. DOI: 10.1109/GLOCOM.1995.500276.

[129] M. Stojanovic and J. Preisig. “Underwater acoustic communication channels: Propagation models and statistical characterization”. In: *IEEE Commun. Mag.* 47.1 (2009), pp. 84–89. ISSN: 0163-6804. DOI: 10.1109/MCOM.2009.4752682.

[130] G. Strang. “The finite element method and approximation theory”. In: *Proc. Sympos. Numerical Solution of Partial Differential Equations*. New York: Academic Press, 1971, pp. 547–583.

[131] J.A. Stratton. *Electromagnetic theory*. McGraw-Hill, 1941.

[132] Gordon L. Stüber. *Principles of Mobile Communication*. 3rd. New York: Springer-Verlag, 2012.

[133] *Study on channel model for frequencies from 0.5 to 100 GHz*. URL: www.etsi.org/deliver/etsi_tr/138900_138999/138901/14.../tr_138901v140000p.pdf (visited on 2017).

[134] S. Sun, G. R. MacCartney, and T. S. Rappaport. “A novel millimeter-wave channel simulator and applications for 5G wireless communications”. In: *Proc. ICC*. 2017, pp. 1–7.

[135] S. Sun et al. “Investigation of Prediction Accuracy, Sensitivity, and Parameter Stability of Large-Scale Propagation Path Loss Models for 5G Wireless Communications”. In: *IEEE Transactions on Vehicular Technology* 65.5 (2016), pp. 2843–2860. ISSN: 0018-9545. DOI: 10.1109/TVT.2016.2543139.

[136] J. Sykora. “Tapped delay line model of linear randomly time-variant WSSUS channel”. In: *Electronics Letters* 36.19 (2000), pp. 1656–1657. ISSN: 0013-5194. DOI: 10.1049/el:20001168.

[137] J. D. Taylor. *Introduction to Ultra-Wideband Radar Systems*. Taylor & Francis, 1994.

[138] P. Tewari, S. Soni, and B. Bansal. "Time-Domain Solution for Transmitted Field Through Low-loss Dielectric Obstacles in a Microcellular and Indoor Scenario for UWB Signals". In: *IEEE Trans. Veh. Technol.* 64.2 (2015), pp. 541–552.

[139] J. B. Thomas. *An introduction to statistical communication theory*. Wiley, 1969.

[140] A. N. Tikhonov et al. *Numerical methods for the solution of ill-posed problems*. Dordrecht, Boston: Kluwer Academic Publishers, 1995.

[141] J. Timmermann et al. "Investigating the influence of the antennas on UWB system impulse response in indoor environments". In: *Radar Conference, 2007. EuRAD 2007. European*. 2007, pp. 283–286.

[142] J.R. Treichler, I. Fijalkow, and C.R. Johnson. "Fractionally spaced equalizers: How long should they really be?" In: *IEEE Signal Process. Mag.* 13.3 (1996), pp. 65–81.

[143] Steven A. Tretter. *Communication System Design Using DSP Algorithms: With Laboratory Experiments for the TMS320C6713 DSK*. Springer, 2008.

[144] M.K. Tsatsanis and G.B. Giannakis. "Time-varying system identification and model validation using wavelets". In: *IEEE Trans. Signal Process.* 41.12 (1993), pp. 3512–3523. ISSN: 1053-587X. DOI: 10.1109/78.258089.

[145] D. Tse and P. Viswanath. *Fundamentals of Wireless Communications*. Cambridge: Cambridge University Press, 2005.

[146] G. L. Turin. *Communication Through Noisy, Random-multipath Channels*. Tech. rep. MIT, 1956.

[147] G. Ungerboeck. "Fractional Tap-Spacing Equalizer and Consequences for Clock Recovery in Data Modems". In: *IEEE Trans. Commun.* 24.8 (1976), pp. 856–864. ISSN: 0090-6778. DOI: 10.1109/TCOM.1976.1093381.

[148] T. Uyematsu, T. Iida, and K. Sakaniwa. "An optimization of the stable tap-adjustment algorithm for the fractionally spaced equalizer". In: *Proc. GLOBECOM*. Vol. 1. 1988, pp. 366–370. DOI: 10.1109/ICC.1988.13592.

[149] P. P. Vaidyanathan, See-May Phoong, and Yuan-Pei Lin. *Signal Processing and Optimization for Transceiver Systems*. Cambridge University Press, 2010.

[150] Harry L. Van Trees. *Detection, Estimation, and Modulation Theory*. New York: John Wiley & Sons, 1971.

[151] H.L. Van Trees. *Optimum Array Processing: Part IV of Detection, Estimation, and Modulation Theory*. Wiley, 2004.

[152] R. Vaughan and J.B. Andersen. *Channels, Propagation and Antennas for Mobile Communications*. IET, 2003.

[153] G. Vitetta et al. *Wireless Communications: Algorithmic Techniques*. Wiley, 2013.

[154] L. A. Wainstein and V. D. Zubakov. *Extraction of Signals from Noise*. Dordrecht, Boston: (translated from Russian by R. A. Silverman), Prentice-Hall I Englewood Cliffs, New Jersey., 1995.

[155] R. H. Walden. "Analog-to-digital converter survey and analysis". In: *IEEE J. Sel. Areas Commun.* 17.4 (1999), pp. 539–550. ISSN: 0733-8716. DOI: 10.1109/49.761034.

[156] G.G. Walter and X. Shen. *Wavelets and Other Orthogonal Systems, Second Edition*. Studies in Advanced Mathematics. Taylor & Francis, 2000.

[157] L.G. Weiss. "Wavelets and wideband correlation processing". In: *IEEE Signal Process. Mag.* 11.1 (1994), pp. 13–32. ISSN: 1053-5888. DOI: 10.1109/79.252866.

[158] B. Widrow et al. "Stationary and nonstationary learning characteristics of the LMS adaptive filter". In: *Proc. IEEE* 64.8 (1976), pp. 1151–1162. ISSN: 0018-9219. DOI: 10.1109/PROC.1976.10286.

[159] W. Wiesbeck, G. Adamiuk, and C. Sturm. "Basic Properties and Design Principles of UWB Antennas". In: *Proc. IEEE* 97.2 (2009), pp. 372–385. ISSN: 0018-9219. DOI: 10.1109/JPROC.2008.2008838.

[160] M. Z. Win, R. A. Scholtz, and M. A. Barnes. "Ultra-wide bandwidth signal propagation for indoor wireless communications". In: *Proc. ICC*. Vol. 1. 1997, pp. 56–60.

[161] M.Z. Win and R.A. Scholtz. "Impulse radio: how it works". In: *IEEE Commun. Lett.* 2.2 (1998), pp. 36–38. ISSN: 1089-7798. DOI: 10.1109/4234.660796.

[162] M.Z. Win and R.A. Scholtz. “On the robustness of ultra-wide bandwidth signals in dense multipath environments”. In: *IEEE Commun. Lett.* 2.2 (1998), pp. 51–53.

[163] Gregory W. Wornell. “Emerging applications of multirate signal processing and wavelets in digital communications”. In: *IEEE Commun. Lett.* 8.3 (2004), pp. 135–137.

[164] J.M. Wozencraft and I.M. Jacobs. *Principles of communication engineering*. Wiley, 1965.

[165] Tao Xu et al. “Multi-Rate Block Transmission Over Wideband Multi-Scale Multi-Lag Channels”. In: *IEEE Trans. Signal Process.* 61.4 (2013), pp. 964–979. ISSN: 1053-587X. DOI: 10.1109/TSP.2012.2230169.

[166] K.Y. Yazdandoost and R. Kohno. “Ultra wideband antenna”. In: *IEEE Commun. Mag.* 42.6 (2004), S29–S32.

[167] K.Y. Yazdandoost and R. Kohno. “Ultra wideband antenna”. In: *IEEE Commun. Mag.* 42.6 (2004), S29–S32.

[168] L. Yu and L. B. White. “Optimum Receiver Design for Broadband Doppler Compensation in Multipath/Doppler Channels With Rational Orthogonal Wavelet Signaling”. In: *IEEE Trans. Signal Process.* 55 (8 2007), pp. 4091–4103.

[169] Hongbing Zhang and H. Howard Fan. “An indoor wireless channel model based on wavelet packets”. In: *Signals, Systems and Computers, 2000. Conference Record of the Thirty-Fourth Asilomar Conference on*. Vol. 1. 2000, 455–459 vol.1. DOI: 10.1109/ACSSC.2000.910996.

[170] Hongbing Zhang, H.H. Fan, and Alan Lindsey. “A wavelet packet based model for time-varying wireless communication channels”. In: *Wireless Communications, 2001. (SPAWC ’01). 2001 IEEE Third Workshop on Signal Processing Advances in*. 2001, pp. 50–53. DOI: 10.1109/SPAWC.2001.923841.